Concentration Preserving Deicing Solutions for Higher Ice

IOWA | DOT

IHRB celebrating 75 years

Disclaimer

The contents of this report reflect the views of the authors, who are responsible for the facts and the accuracy of the information presented herein. The opinions, findings, and conclusions expressed in this publication are those of the author and not necessarily those of the project sponsor(s).

The sponsors assume no liability for the contents or use of the information contained in this document. This report does not constitute a standard, specification, or regulation.

The sponsors do not endorse products or manufacturers. Trademarks or manufacturers' names appear in this report only because they are considered essential to the objectives of the document.

Statement of Non-Discrimination

Iowa DOT ensures non-discrimination in all programs and activities in accordance with Title VI of the Civil Rights Act of 1964. Any person who believes that they are being denied participation in a project, being denied benefits of a program, or otherwise being discriminated against because of race, color, national origin, gender, age, or disability, low income, and limited English proficiency, or needs more information or special assistance for persons with disabilities or limited English proficiency, please contact Iowa DOT Civil Rights at 515-239-7970 or by email at civil.rights@iowadot.us.

TECHNICAL REPORT DOCUMENTATION PAGE

1. Report No.	2. Government Accession No.	3. Recipient's Catalog No.
IHRB Project TR-814		

4. Title and Subtitle	5. Report Date
Concentration Preserving Deicing Solutions for Higher Ice Melting	Dec 2025
	6. Performing Organization Code

7. Author(s)	8. Performing Organization Report No.
Ravi Kiran Yellavajjala, Ph.D., P.E. https://orcid.org/0000-0001-8300-0767 Sher Afgan https://orcid.org/0000-0001-6326-2452 Maedeh Hesami https://orcid.org/0009-0006-2028-2991 Muhammad Rafiul Mahdi https://orcid.org/0000-0001-9552-7865	

9. Performing Organization Name and Address	10. Work Unit No.
Arizona State University, Room #174, ISTB5, 600 E Tyler Mall, Tempe, AZ 85281	11. Contract or Grant No.

12. Sponsoring Agency Name and Address	13. Type of Report and Period Covered
Iowa Highway Research Board Iowa Department of Transportation 800 Lincoln Way, Ames, IA 50010.	7/1/2023-12/30/2025
	14. Sponsoring Agency Code

15. Supplementary Notes

16. Abstract

Chloride-based brine deicers are widely used to maintain winter roadway safety, but their performance drops in extreme cold as meltwater dilutes the brine, and their runoff accelerates concrete deterioration, rebar corrosion, and ecological harm. This report investigates sustainable, high-performance deicing formulations that enhance low-temperature ice melting while limiting infrastructure damage and preserving pavement friction. Both concentration-preserving and oversaturated deicing formulations have been considered. Superabsorbent polymers (SAPs) and corn-derived polyols were used to prepare concentration-preserving and oversaturated deicing formulations, respectively. Superabsorbent polymers (SAPs) are introduced to brines to retain meltwater and sustain salt concentration at the ice–solution interface. Their swelling behavior is quantified using both bulk absorption tests and optical microscopy with 3D reconstruction of individual particles in distilled water and saline solution, revealing strong particle-size dependence and rapid uptake primarily within the first five minutes. Deicer performance is evaluated through freezing-point depression and ice-melting capacity tests at 0, −10, −20, and −30 °C using controlled laboratory setups. The results showed that adding 5% large-particle-sized SAPs increased ice-melting capacity by up to 80% compared to the brine solution at − 30°C. This improvement in ice-melting capacity occurred by preserving the salt concentration in the SAP-adsorbed water. Corn-derived polyol additives (erythritol and xylitol) are assessed in salt brines for freezing-point reduction and enhanced melting, achieving freezing points near −37.5 °C and improved ice-melting capacity at subzero temperatures relative to conventional brines. Skid resistance is evaluated using British Pendulum testing on asphalt and Portland cement concrete, showing negligible friction loss with optimized SAP brine formulations and comparable or slightly improved skid resistance with select polyol brine mixtures. Corrosion mitigation is evaluated for low-carbon, high-strength steel exposed to aggressive chloride environments using visual inspection and potentiodynamic polarization tests. Polyols act as mixed-type inhibitors that adsorb onto steel surfaces, markedly reducing corrosion rates. Overall, the results demonstrate that tailoring the additive type, concentration, and SAP particle size can simultaneously improve extreme-cold deicing effectiveness, maintain skid resistance, and reduce chloride-driven corrosion.

17. Key Words	18. Distribution Statement
Deicing solution; Biobased polyols; Superabsorbent polymers; Chloride; and Ice melting	No restrictions.

19. Security Classif. (of this report)	20. Security Classif. (of this page)	21. No. of Pages	22. Price
Unclassified	Unclassified	102	$109,697

Form DOT F 1700.7 (8-72) Reproduction of completed page authorized

Concentration Preserving Deicing Solutions for Higher Ice Melting

Final Report

Dec 2025

Principal Investigator

Ravi Kiran Yellavajjala, Ph.D., P.E.

Associate Professor

School of Sustainable Engineering and the Built Environment

Ira A. Fulton Schools of Engineering

Arizona State University

Co-authors

Sher Afgan[1], Maedeh Hesami[2], and Muhammad Rafiul Mahdi[2]

[1] Graduate student at North Dakota State University

[2] Graduate student at Arizona State University

Sponsored by

The Iowa Highway Research Board

(IHRB Project TR-814)

A Report from

Damage in Materials and Structures Laboratory

School of Sustainable Engineering and the Built Environment

Room #174, ISTB5, 600 E Tyler Mall, Tempe, AZ 85281

Phone: 480-965-2790

Fax: 480-965-0557

1. Acknowledgments

The Principal Investigator (PI) extends heartfelt gratitude to the Iowa Highway Research Board (IHRB) for their generous sponsorship of this research endeavor. The PI would also like to express sincere appreciation to the Technical Advisory Committee (TAC) members, namely Tina Greenfield Huitt and Craig Bargfrede, for their valuable comments and suggestions throughout the project. Their enthusiasm for this project and suggestions provided during the TAC meetings have contributed to its successful completion.

The PI is immensely grateful to Ms. Vanessa Goetz for her unwavering support during the launch and execution of this project. The authors wish to acknowledge the invaluable assistance provided by Jeff Long at Arizona State University in conducting experimental studies.

2. Metric Conversion Chart

[The conversion factors table below is taken from Modern Metric Conversion Factors, provided by Federal Highway Administration and last updated in 2019. **Insert this table only if the report includes metric references.**]

SI* (MODERN METRIC) CONVERSION FACTORS				
APPROXIMATE CONVERSIONS TO SI UNITS				
Symbol	**When You Know**	**Multiply By**	**To Find**	**Symbol**
		LENGTH		
in	inches	25.4	millimeters	mm
ft	feet	0.305	meters	m
yd	yards	0.914	meters	m
mi	miles	1.61	kilometers	km
		AREA		
in^2	square inches	645.2	square millimeters	mm^2
ft^2	square feet	0.093	square meters	m^2
yd^2	square yard	0.836	square meters	m^2
ac	acres	0.405	hectares	ha
mi^2	square miles	2.59	square kilometers	km^2
		VOLUME		
fl oz	fluid ounces	29.57	milliliters	mL
gal	gallons	3.785	liters	L
ft^3	cubic feet	0.028	cubic meters	m^3
yd^3	cubic yards	0.765	cubic meters	m^3
		NOTE: volumes greater than 1000 L shall be shown in m^3		
		MASS		
oz	ounces	28.35	grams	g
lb	pounds	0.454	kilograms	kg
T	short tons (2000 lb)	0.907	megagrams (or "metric ton")	Mg (or "t")
		TEMPERATURE (exact degrees)		
°F	Fahrenheit	5 (F-32)/9 or (F-32)/1.8	Celsius	°C
		ILLUMINATION		
fc	foot-candles	10.76	lux	lx
fl	foot-Lamberts	3.426	$candela/m^2$	cd/m^2
		FORCE and PRESSURE or STRESS		
lbf	poundforce	4.45	newtons	N
lbf/in^2	poundforce per square inch	6.89	kilopascals	kPa
APPROXIMATE CONVERSIONS FROM SI UNITS				
Symbol	**When You Know**	**Multiply By**	**To Find**	**Symbol**
		LENGTH		
mm	millimeters	0.039	inches	in
m	meters	3.28	feet	ft
m	meters	1.09	yards	yd
km	kilometers	0.621	miles	mi
		AREA		
mm^2	square millimeters	0.0016	square inches	in^2
m^2	square meters	10.764	square feet	ft^2
m^2	square meters	1.195	square yards	yd^2
ha	hectares	2.47	acres	ac
km^2	square kilometers	0.386	square miles	mi^2
		VOLUME		
mL	milliliters	0.034	fluid ounces	fl oz
L	liters	0.264	gallons	gal
m^3	cubic meters	35.314	cubic feet	ft^3
m^3	cubic meters	1.307	cubic yards	yd^3
		MASS		
g	grams	0.035	ounces	oz
kg	kilograms	2.202	pounds	lb
Mg (or "t")	megagrams (or "metric ton")	1.103	short tons (2000 lb)	T
		TEMPERATURE (exact degrees)		
°C	Celsius	1.8C+32	Fahrenheit	°F
		ILLUMINATION		
lx	lux	0.0929	foot-candles	fc
cd/m^2	$candela/m^2$	0.2919	foot-Lamberts	fl
		FORCE and PRESSURE or STRESS		
N	newtons	0.225	poundforce	lbf
kPa	kilopascals	0.145	poundforce per square inch	lbf/in^2

Table of Contents

3. List of Figures

4. List of Tables

1. Application Deicers for Improved Mobility in Winters

1.1 Introduction

The accumulation of snow and ice on roads has consistently posed a longstanding safety issue in cold climate regions. Various chemical deicers are employed for deicing operations, including sodium chloride (NaCl), magnesium chloride ($MgCl_2$), calcium chloride ($CaCl_2$), calcium magnesium acetate ($Ca_xMg_y(C_2H_3O_2)_{2(x+y)}$), potassium acetate (KAc), and some agri-based deicers [1]–[4]. Among all, sodium chloride (also referred to as bulk rock salt) is the most frequently used deicer owing to its low cost, high efficiency, and relatively lower toxicity. However, the extensive application of salt brine deicer can lead to several drawbacks, including reduced efficiency at very low temperatures (below -12°C), corrosion damage in the transportation infrastructure, contamination of freshwater sources, and harm to aquatic wildlife. Therefore, there is a growing interest among researchers to reduce the amount of brine deicer or increase its efficiency through the incorporation of various chemical additives. Iowa DoT used more than 7 million gallons of salt brine to conduct snow and ice control in 2018 utilizing a full fleet of 879 snowplows that have the potential to deice more than 10,000 lane-miles (source: Iowa DoT winter operations). Although salt brine is economical and efficient, it has two negative consequences on transportation infrastructure: 1) chloride-ion induced corrosion, and 2) corrosion of vehicles and snowplows [5], [6]. While attaining a high ice-melting capacity is the key feature of a desired deicer, analyzing the frictional properties of the pavement surface after the application of the deicer is also critical for ensuring safe vehicle operation in snowy regions. Skid resistance is commonly employed to quantify the degree of slipperiness of the pavement surface. Low skid resistance of the pavement surface is one of the major contributors to unsafe road condition in extreme cold climates [7].

As noted by previous studies, the application of traditional brine deicer on icy pavement can significantly enhance the skid resistance of surface in the absence of any additives. However, the addition of organic additives to salt brine solution can significantly impair the skid resistance of the road pavement due to its high viscosity and nonuniform distribution on the surface. Cao et al., employed three distinct types of agro-based deicers combined with $MgCl_2$ and $CaCl_2$ to evaluate the friction properties of the iced and deiced concrete surface. Their results showed that addition of agro-based deicers led to the lower skid resistance on both the ice and deiced concrete surface when compared with two traditional deicing salts of sodium chloride (NaCl) and calcium chloride ($CaCl_2$). In another study conducted by Sajid et al., three bio-based non-toxic corn-derived polyols were added to the brine solutions at various weight concentrations. Their results showed that the addition of 27.7% polyol to the traditional brine solution increased its ice melting by 100% when compared to the typical salt brine deicer. However, the skid resistance of the Portland cement concrete (PCC) surface was reduced up to 33% when compared to the skid resistance of dry pavement surface.

Some organic or inorganic additives can improve the performance of brine deicer by lowering the freezing point and enhancing the ice melting capacity of deicer, particularly at extremely low temperatures. Taylor et al. employed a combination of chloride-based deicers (NaCl and $MgCl_2$), glycerol, and commercial agricultural-based (agro-based) deicers to evaluate their ice melting efficiency. According to their results, a combination of 80% glycerol with 20% NaCl has shown the greatest promise with a freezing point of -43°C and ice melting capacity equivalent to that of 100% NaCl. However, chemical additives with lower eutectic point than NaCl cannot guarantee the superior ice melting capacity at extreme cold temperatures. Nilssen et al. investigated the effect of different additives including magnesium chloride ($MgCl_2$), calcium magnesium acetate (CMA), potassium formate (KFo), calcium chloride ($CaCl_2$), and sugar (sucrose) to NaCl (80% NaCl with 20% additive) at −18°C. Their results

revealed that NaCl had the highest ice-melting capacity in the solid state, surpassing the second-best solid deicer, $CaCl_2$-$2H_2O$, by 31%. All the other additives to solid NaCl resulted in a negligible ice-melting capacity.

1.1.1 Reducing the Corrosivity of Traditional Deicers

Deicers play a crucial role in winter road maintenance and are a primary component of snow removal operations. Treating roadways with deicers helps melt the ice and ensure sufficient skid resistance for vehicular traffic in wet conditions. Commonly used salt brine deicers are known to lower the freezing point of water to -21.1°C. Traditionally, chloride-based salts such as sodium chloride (NaCl) and calcium chloride (CaCl2) are commonly used deicers due to their low cost and abundant availability. In addition to chlorides, acetate-based deicers (potassium acetate, sodium acetate, and calcium magnesium acetate), and formate-based deicers (potassium formate) have also been used. While chloride-based deicers are effective in deicing operations, their usage causes significant durability issues in pavements and are among the primary cause of corrosion in bridge infrastructure. Apart from chloride and acetated-based deicers, several alternative deicers, which are mostly agriculturally derived, have been investigated in recent years for their snow-melting efficacy and corrosion mitigation. These alternative deicers include glycerol, beet juice, and molasses obtained from agricultural sources. For winter road maintenance, sodium chloride-based deicers are the most often used among currently available deicers. The United States Geological Survey (USGS) estimates that the US uses up to 24 million metric tons of deicing salt each year, mostly made up of sodium chloride and other products with a chloride basis.

While chloride-based deicers perform well in snow removal operations at moderately low temperatures, their ice-melting performance reduces drastically at lower temperatures (below -21.1°C). Furthermore, the harmful impacts of chloride-based salts are far-reaching as they increase the potential of corrosion in structures and pollute the environment by increasing the salt content in stream water after runoff. Chloride-based deicers are the primary contributor to infrastructure and vehicular corrosion, and they are widely documented to accelerate corrosion and corrosion-induced deterioration in steel and RC bridges, RC pavements, and ancillary steel structures along highways. Their usage thus results in hefty maintenance and repairs. Additionally, their runoff into soil and water bodies causes an imbalance in pH level, increases soil salinity, and reduces dissolved oxygen (DO) level in water. These alterations in soil and water properties negatively impact crop production, ecological balance, biodiversity, and the quality of drinking water sources. Therefore, alternative deicers are required to circumvent the infrastructural and environmental concerns associated with chloride-based deicers while maintaining deicers' effectiveness at subzero temperatures. To this end, various additives have been added to salt brine deicer to lower their freezing point and mitigate their adverse effects. Different organic and inorganic additives have been added to brine solutions to decrease the freezing point of water as research suggests that the addition of non-volatile solute greatly depreciates the freezing point. These additives lower the eutectic point of water. However, it is worth noting that a lower eutectic point doesn’t necessarily translate to a higher ice melting capacity. With this aim in view, this study focuses on exploring the effects of the addition of polyols especially, xylitol and erythritol on the ice melting capacity as well as other important properties of salt brine deicer.

1.2 Research gaps

A novel approach for enhancing the ice melting capacity of the traditional brine deicer is to preserve the saltwater concentration in saturated super absorbent polymer (SAP) that will desorb salt water gradually to melt more ice. The introduction of SAP to the deicer solution can not only open several new possibilities for enhancing the efficiency of deicers, but also can maintain the skid resistance of the pavement surface, enhancing road safety. SAPs are three-dimensional cross-linked network polymers that do not dissolve in water. They can absorb and hold water up to several hundred times their own weight by swelling their polymeric networks. Despite their frequent use in industries such as sanitation (e.g., diapers), healthcare (e.g., bandage production), and construction (e.g., as internal curing agents in concrete admixtures), their potential as additives to traditional brine deicers remains unexplored. Additionally, conventional brine deicers can cause severe corrosion in steel structures and reinforcing bars embedded in concrete. The resulting corrosion leads to expansion, cracking, and eventual loss of structural integrity. Current commercial corrosion mitigation options are often costly or toxic, highlighting the need to investigate sustainable, biobased alternatives. This research aims to evaluate and characterize such biobased solutions for potential future application.

1.3 Technical Objectives

The overarching goal of this project is to mitigate rebar corrosion by employing sustainable and renewable materials. This goal is accomplished by fulfilling the following technical objectives:

1) To evaluate the performance of xylitol and erythritol, on the performance of NaCl brine solutions for snow removal operations.
2) To quantify the effects of varying concentrations of xylitol and erythritol on the freezing point depression, ice melting capacity, and pavement skid resistance of traditional brine deicer solution (23.3% wt. NaCl).
3) To investigate the impact of weight fractions of these two polyols on dissolved oxygen (DO) levels in nearby streams.
4) To quantify the correlation between the dry and swollen SAP particle volumes in cementitious, brine, and aqueous solutions.
5) To study the performance of erythritol and xylitol as corrosion inhibitors in traditional brine deicer.

1.4 Organization of the report

A detailed discussion on the use of superabsorbent polymers (SAPs) as additives to a traditional deicer solution (23.3 wt.% NaCl) and their ice-melting capacity at various low temperatures is presented in Chapter 2. This chapter also evaluates five commercial SAPs with distinct material properties. Chapter 3 provides a comprehensive analysis of erythritol and xylitol for lowering the freezing point of deicing solutions. Chapter 4 examines the potential of xylitol and erythritol as biobased corrosion inhibitors for protecting ASTM A572 steel. Chapter 5 discusses the variation and distribution of dry and swollen SAP particle sizes in cement pore solution and traditional deicers. Finally, Chapter 6 summarizes the key findings of this project and offers recommendations for future studies.

1.5 Research products from the project

This project resulted in four journal articles and five conference talks/ posters. Here are the references to the published articles:

1.5.1 Journal articles

1) G. Merke, M. Hesami, and **R. Yellavajjala**, "Super Absorbent Polymers (SAPs) as concentration preservers in brine deicers for enhanced ice melting capacity," *J. Infrastruct. Preserv. Resil.*, vol. 6, no. 1, pp. 1–15, 2025, doi: 10.1186/s43065-024-00105-z.
2) S. Afgan, **R. Yellavajjala**, and X. Qi, "Mitigating corrosion damage in steel employing biobased erythritol and xylitol as corrosion inhibitions," vol. 37, no. August, pp. 1–14, 2024, doi: 10.1061/JMCEE7.MTENG-18945.
3) M. Rafiul, S. Afgan, H. Sajid, and **R. Yellavajjala**, "Lowering Freezing Point and Improving Ice Melting Capacity of Deicers with Xylitol and Erythritol" (Revised Version Submitted**)**
4) M. Hesami, M. Acharya, M. Rafiul, S. Dey, N. Neithalath, and **R. Yellavajjala**, "Correlation between dry and swollen superabsorbent polymer particle sizes in cement pore solution and salt brine," (Submitted**)**

2 Super Absorbent Polymers (SAPs) as Concentration Preservers in Brine Deicers for Enhanced Ice Melting Capacity

This study aimed to investigate the effect of introducing various SAPs into a traditional brine deicer solution (23.3% wt. NaCl) on its ice melting capacity at various low temperatures. Five commercial SAPs with distinct material properties were chosen and added to the brine solution at different weight concentrations. A comprehensive set of tests was conducted to evaluate the efficiency of these materials, including: 1) swelling test to evaluate the absorption capacity of SAPs in salt brine solution; 2) ice melting capacity test to assess the ice melting capacity of SAP-brine deicers at low temperatures; and 3) skid resistance test to evaluate the slipperiness of the pavement in the presence of SAP-brine solution. Characterization of SAPs, along with the conducted tests, and the results obtained from each test were discussed in detail.

2.1 Super Absorbent Polymers (SAPs) and Quantification of their Deicing Potential

2.1.1 Properties of SAPs

Five commercially available SAPs are obtained from Emerging Technologies[4], including Liquiblock WHS1 (SA), Liquiblock WHS2 (SB), Liquiblock 40F (SC), Liquiblock HS Fines (SD), and Liquiblock 2g-110 (SE) in this study. The properties of these SAPs including chemical composition, particle size distribution (PSD) in µm, pH value, apparent bulk density in grams/liter (g/l), moisture content in %, and deionized water absorption capacity in grams/gram (g/g) are summarized in Table 2-1.

Among the considered SAPs, SA, and SB, have large particle sizes, SC has medium particle sizes and SAPs SD and SE have small particle sizes. Furthermore, SAP SE is a potassium salt of crosslinked polyacrylic acid /polyacrylamide, whereas the other SAPs are sodium salts of crosslinked polyacrylic acid. It is also important to note that all the SAPs are slightly acidic, with the SAP SA being the most acidic of all. Moreover, all the SAPs are less dense than salt whose relative density is 1200 grams per liter, and hence occupy more volume. Despite their hydrophilic nature, all the SAPs have less than 7% moisture content at the time of delivery. Large particle-sized SAPs usually have larger water absorption capacity despite lower surface area owing to their porosity and accessibility of higher polymer chains in each particle [7], [18].

It is important to note that the water absorption values in Table 2-1 may not be directly applicable in the current pursuit, as the SAPs will be added to the salt brine solution and not deionized water. This information, however, is still valuable to understanding the reduction in absorption capacity. The swelling in the SAPs occurs in three distinct stages. In the first stage, also referred to as the wetting stage, the surface of the SAP crystals will contact the water molecules. In the second stage, the water molecules travel through the micropores of the SAP crystals leading to their volumetric swelling. In the third and final stage, the maximum water swelling capacity is reached when either the maximum water binding capacity of the SAP is reached, or the osmotic pressure gradient is diminished [1]. However, in a salt solution, the SAPs bind the free ions in the salt brine solution causing a screening effect which blocks the entry of water molecules in the first two stages of swelling and preventing the initiation of the third stage of swelling. This screening effect was previously reported in the literature for sodium chloride, potassium chloride, and calcium chloride solutions [19]. In a recent study, it was noted that the swelling

capacity was reduced from about 150 to 17 grams/gram for a sodium acrylate-co-acrylamide-based gel in brine solution [20]. For this reason, further testing is necessary to evaluate the swelling properties of each SAP in the salt brine solution. The weight concentration and the type of salt in reference brine deicer is taken as 23.3% wt. NaCl is popularly used for deicing roads throughout the US. This composition is also referred to as the eutectic composition of the sodium chloride water system which lowers the freezing point of water from 0℃ to -21℃ [21]. The water absorption capacity is one of the most important characteristics of SAPs. SAP particles do not dissolve in water due to their composition as crosslinked homopolymers or copolymers. However, the water molecules diffuse into their polymeric chain, resulting in swelling. If the absorption capacity of SAP in a salt brine solution is too high, the viscosity of the solution would increase excessively, reducing the spreading power of the salt brine deicer and decreasing the skid resistance. Hence, it is necessary to quantify the absorption capacity of SAP additives in traditional road deicing brine solution as an initial step.

Table 2-1: Material properties of SAPs.

SAP ID	**SA**	**SB**	**SC**	**SD**	**SE**
Commercial Name	Liquiblock™ WHS1	Liquiblock™ WHS2	Liquiblock™ 2g-110	Liquiblock™ HS Fines	Liquiblock™ 40F
Chemical composition	Sodium salt of crosslinked polyacrylic acid	Sodium salt of crosslinked polyacrylic acid	Sodium salt of crosslinked polyacrylic acid	Sodium salt of crosslinked polyacrylic acid	Potassium salt of crosslinked polyacrylic acid /polyacrylamide copolymer
Particle Size Distribution (μm)	0-850	150-850	<600	1-140	1-200
pH	4	5.6-6.6	6	5.4	5.5-6.0
Apparent Bulk Density (g/l)	600	600-700	400	500	540
Moisture Content (%)	<7	0-5	<5	<7	5
Absorption (g/g) in Deionized H_2O	>400	>450	>490	>180	>200

2.2 Characterization Methods

2.2.1 Swelling test

Several traditional methods have been utilized in the past to measure the water absorbency capacity of SAPs, including the sieve method, filtration method, and tea-bag method [6]. While the sieve and filtration method generally require larger sample quantity, the tea bag method is suitable even with smaller sample quantities. This is particularly relevant when the SAPs have very high water absorption capacity [22].

In this study, the tea-bag method is employed to evaluate the absorption capacity of SAPs as it is fast and accurate even for small sample sizes. To experiment, one gram of dry SAP was placed inside a tea bag made of wood pulp paper with overall bag dimensions of 2.36 inches × 3.15 inches [23]. The tea

bag was then sealed with a tie-off string at the top. The 23.3% wt. NaCl solution was prepared at room temperature and each tea bag was submerged in the solution over a 24-hour period, with measurements taken after 1, 5, 10, 30, 60, and 1440 minutes. To ensure complete immersion of the tea bags and to eliminate carbonation, a small weight was placed on top of the tea bags.

At specific time periods of 1, 5, 30, 60, 120, and 1440 minutes, each tea bag was taken out from the brine solution, gently wiped with a paper towel to remove excess liquid, and then weighed as shown in Figure 2-1. The absorption capacity of each SAP at a given time, denoted as W_t, can be calculated using the following equation:

$$W_t = \frac{W_f - W_{tb} - W_{SAP}}{W_{SAP}} \quad (1)$$

where, W_f is the final mass of the tea bag in grams (g) containing the swelled SAP at time t, W_{tb} is the initial mass of the empty tea bag (g), and W_{SAP} is the initial mass of the SAP sample (g). The results of the swelling test in 23.3% wt. NaCl brine solution are discussed in detail in Section 2.3.1.

Figure 2-1: Swollen tea bags of SAPs after removal from NaCl brine solution.

2.2.2 Ice Melting Capacity Test

The ice melting capacity (IMC) of brine solution depends on its salt concentration and the ambient temperature. At 0°C, the ice and water have the same chemical potential and can co-exist without the ice melting. However, the salt brine is always warmer than ice in practice and has lower chemical potential than ice leading to snow/ ice melting. In addition, the salt brine comprises of disassociated sodium and chloride ions along with some undissolved salt particles. The ions function as contaminants to disrupt the arrangement of water molecules, preventing the formation of crystal lattice structures necessary for the re-formation of ice from the melted snow/ ice. As the concentration of salt increases up to the eutectic composition, the chemical potential decreases and the disruption of water molecules is intensified leading to lower freezing point of brine solution and consequently higher ice melting capacity. At extremely cold temperatures (less than -10°C), however, the ice melting efficiency of brine solution is drastically impaired [24]. To counteract this reduction, various additives such as polyols, beet juice, corn juice, etc. have been used to improve the low-temperature performance of deicers [25], [26]. Similar to the brine solution, the ice melting capacity of these additives is also strongly associated with the solute concentration. On the other hand, the SAPs that are already saturated

with salt water tend to desorb this salt water to melt more ice. Thus far, the ice melting capacity SAPs saturated with salt water has not been investigated yet and will be attempted in this study.

To date, several test methods have been developed to measure the ice melting capacity of deicers including SHRP H-205.1 and SHRP H-205.2 (Strategic Highway Resource Program) tests, the ice cube titration test, the shaker test, and the mechanical rocker test [27]. While the first two methods use controlled settings to monitor changes in the solution concentration or the weight of melting ice cubes, the latter two methods employ mechanical agitation to replicate the effects of mechanical forces on road surfaces.

Among various standards, SHRP is the most common industrial standard that applies a limited amount of deicer (about 5 ml for liquid deicers) on a fabricated sheet of ice. The resulting melted ice is then measured by collecting the melt water with a syringe [28]. While this method provides a straightforward and direct assessment of ice melting efficiency, it is prone to significant variations including underestimations of ice melting capacity at lower deicer application rates and overestimations at higher rates and extended measurement times. The main source of these variations is the difficulty of accurately recovering a small amount of meltwater from a relatively large ice sample [27].

To improve this standard method, an alternative approach can be adopted, wherein a small amount of ice cubes is introduced into a larger quantity of deicer. To this end, the current study uses a custom-built apparatus to measure the ice melting capacity of SAP-brine deicers, as shown in Figure 2-2. This apparatus consists of three major components: (a) K-type thermocouples employed to monitor the solution temperature, (b) cooling bath of dry ice pellets used to achieve and maintain required temperatures, and (c) SAP-brine solution maintained at 10°C to simulate the temperature conditions preceding its application on roads. This method was previously co-implemented by one of the authors in a previous study [29].

The ice melting capacity of the SAP added brine solutions is evaluated at four different temperatures of 0°C, −10°C, −20°C, and −30°C. Temperatures below −30°C are not investigated as rock salt deicer solutions are not effective at such temperatures. Special attention was paid to the ice melting capacity around −30°C to investigate how the SAPs enhance the ice melting at temperatures where salt brine becomes increasingly ineffective. This is particularly relevant to northern states in the United States where temperatures dip below -20°C for more than 30 days annually.

To evaluate the ice melting behavior of the deicers, the acetone bath cooled with dry ice was set to four different temperatures of 0°C, −10°C, −20°C, and −30°C using dry ice. Ice cubes, with an approximate cube size of 22.5mm × 22.5mm × 40mm, were formed in a commercial freezer that is set at -5 °C. Each ice cube was immersed in an acetone bath for 2 minutes to attain one of the preset target temperatures (0°C, −10°C, −20°C, and −30°C) and its weight is recorded after being removed and dried off. Then, the weighted ice cube was immersed into the SAP-brine deicer solutions with different weight percentages (as outlined in Table 2-2) of the five SAPs for an additional 2 minutes and weighed again.

The solution designs of 5% addition, 10% addition, and 5% replacement (see Table 2-2) have been chosen due to a multitude of factors including viscosity considerations, economic considerations, and an awareness towards minimal augmentation of brine solutions within experimental parameters. According to our preliminary studies, adding less than 5% SAPs is insufficient to desorb the required salt water to melt ice. Conversely, incorporating SAPs at concentrations exceeding 10% increases the viscosity of the solution, leading to enhanced slipperiness on pavement surfaces. Additionally, higher concentrations are not economically viable as they require more additives without proportionate benefits in ice melting capacity.

Further, this choice in solution design allowed for a quantification of an increasing weight fraction of SAP in brine solution, and further to understand the potential increase in ice melting capacity with a considerable reduction in NaCl concentration. The temperatures of ice cubes for each step were also monitored to ensure the accuracy of the test.

The ice melting capacity of each deicer can be determined by calculating the weight difference of ice cubes before and after its immersion in the deicer solution. To better compare the role of SAP additives in the ice melting capacity of deicing solution, the reduction percentage in weight of the ice cube was derived for SAP-brine solution with respect to the control brine solution according to the following equation:

$$\text{Relative Weight Change} = \frac{WR_S - WR_C}{WR_C} \times 100 \quad (2$$

where, WR_C is the mass loss of the ice cube after submersion in the control (23.3% wt. NaCl) brine solution and WR_S is the mass loss of the ice cube after submersion in SAP-brine solution. A total of 72 different combinations of SAPs-brine solutions with various weight percentages and temperatures (see Table 2-5) were evaluated and each test was repeated 3 times. The results of ice melting capacity tests are discussed in Section 2.3.2.

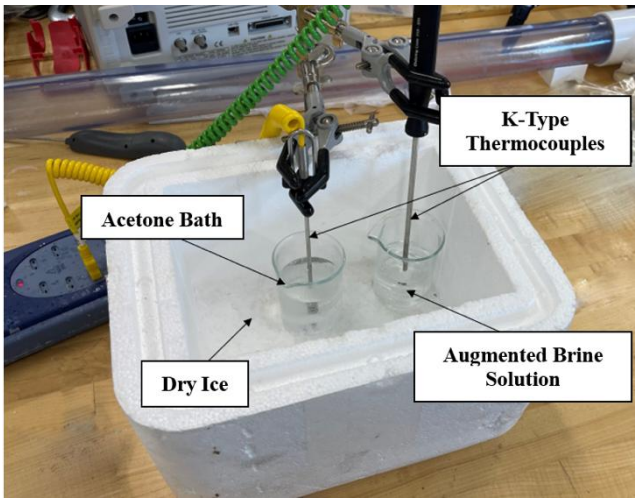

Figure 2-2: In-house test Setup for measuring ice melting capacity.

2.2.3 Skid resistance tests

Skid resistance is defined as the measure of pavement surface resistance to sliding or skidding for a vehicle. It provides a correlation between horizontal and vertical force generated when the tire slides along the surface, and is a measurement used to define and understand road conditions during precipitous and winter storm events. As water/ice film on road and pavement surfaces increases during wet weather, it significantly reduces the skid resistance when compared to dry roadways. This decrease in the skid resistance of the roadway has been shown to result in higher rates of roadway accidents, and increasingly unsafe conditions for drivers [30]. To address this issue, it seems necessary to quantify the skid resistance of a road surface under wet conditions.

So far, numerous measurement methods have been developed to quantify skid resistance of road surface that can be divided into two categories: field measurements and laboratory test methods. Field measurements include methods such as the Side Force Test, Locked Wheel Test, Fixed Slip Test,

and Variable Slip Test which are conducted directly on the road surface [31]–[35]. While each of these field tests can provide friction characteristics of a surface under a specific condition, the variable slip test is usually preferred due to data collected in the form of a full friction curve that can be applied to varying conditions between tires and road surfaces. Laboratory testers, on the other hand, are portable devices designed for skid resistance evaluation in controlled laboratory conditions. Examples of laboratory testers include the British Pendulum Tester (BPT), Dynamic Friction Test (DFT), Sand Pitch Test, and Outflow Test [31], [32], [32]–[37], [37]–[39].

While BPT and DFT are primarily focused on the friction coefficient of road surface, the sand patch test and outflow test consider the texture properties of the runway like surface particulate, roughness, and material composition. This study employs the British Pendulum Tester (BPT) as it is the most common portable laboratory tester to determine the friction characteristics of deiced surface and is governed by ASTM E303 [40]–[43]. The BPT is known for its portability and ease of use in both laboratory and field settings. As a low-speed testing equipment, BPT provides a measure of the kinetic energy lost when a rubber slider is pushed over a test pavement surface. Figure 2-3 (a & b), shows the use of BPT method on both asphalt and Portland Cement Concrete (PCC) pavement surface within the premises of the North Dakota State University, Fargo, USA. The asphalt pavement surface falls in accordance with asphalt specifications in Fargo, USA. The PCC pavement used in the skid resistance tests meets the concrete pavement specifications of the city of Fargo, North Dakota. These specifications require the PCC pavement to be constructed using Portland Cement Type I or II (meeting the requirements of ASTM C-150), clean water (free from oil, acid, alkali, and vegetable substances), well-graded coarse and fine aggregates (conform to the requirements of ASTM C33), and an air-entrainment of 5% to 8% (conforms to ASTM C226 [30]).

The skid resistances of both asphalt and PCC surfaces are determined in three groups of SAP-brine deicing solutions on separate days with weather conditions as outlined in Table 2-2. Each of these deicing solutions is applied to the cleaned surfaces and remains on the surface for 30 minutes. This time interval was chosen to ensure the occurrence of a significant swelling (approximately 85% of SAP's final absorbent capacity), as determined by the results of the tea-bag method (see section 2.3.1) to ensure maximum depreciation in the skid resistance. The British pendulum tester is then used to measure the skid resistance in terms of the British Pendulum Number (BPN) as a measure of friction characteristics of the surface. The higher BPN values imply greater skid resistance of a road pavement surface leading to higher loss in kinetic energy of a moving vehicle. Different locations of PCC and asphalt pavement surface are chosen for each SAP-Brine deicing solution, and each test is repeated 5 times. The results of skid resistance test are further discussed in section 2.3.4.

Table 2-2: The composition of SAP-salt brine deicer solutions with the temperature and relative humidity values recorded on the test day.

Solution	Composition	Temperature(°C)	Relative Humidity (%)
5 % Addition	23.3% wt. NaCl + 5% wt. SAP	-1.1	72
10 % Addition	23.3% wt. NaCl + 10% wt. SAP	-4.4	63
5 % Replacement	18.3% wt. NaCl + 5% wt. SAP	-2.2	80

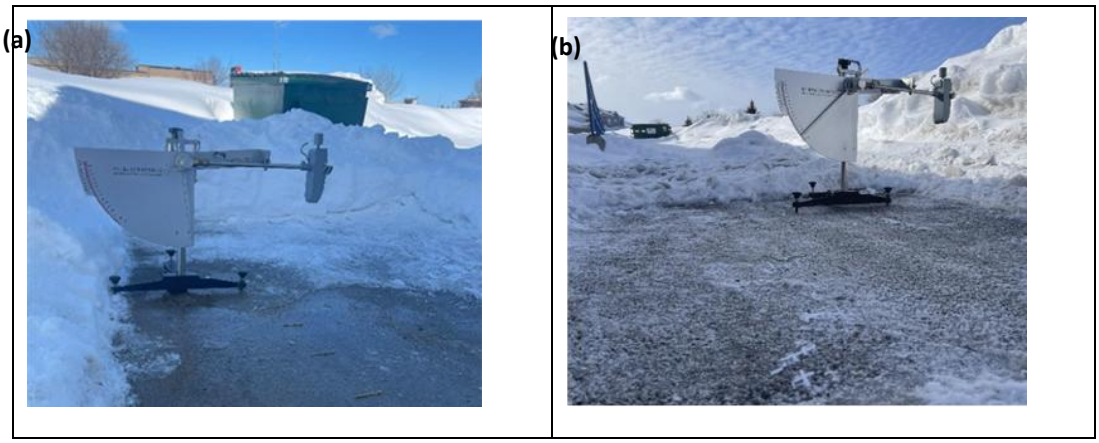

Figure 2-3: British Pendulum Tester for measuring skid resistance of pavement surface on (a) PCC pavement, and (b) asphalt pavement.

2.3 Performance of SAPs in enhancing the ice melting capacity

2.3.1 Swelling behavior of SAPs

The water absorption capacity of each SAP in the 23.3% wt. salt brine solution was measured employing the tea bag method described in Section 2.2.1. The weight of water in grams absorbed by a gram dry weight of SAP is plotted as a function of time in Figure 2-4a. All the SAPs except SE had a similar water absorption as a function of time in the salt brine solution as seen in Figure 2-4a. Notably, SAP-SE exhibited the highest water absorption capacity at all time instances, with a maximum value of 24 grams/gram (g/g). This increased water absorption capacity can be attributed to the higher osmatic pressure caused by the presence of potassium ions in the SAP-SE mixed with a solution containing sodium and chloride ions. The osmatic pressure facilitates the inward flow of water from the salt brine into the SAP-SE crystals. Unlike SAP-SE that is a potassium salt of crosslinked polyacrylic acid/polyacrylamide copolymer, other SAPs are sodium salts of crosslinked polyacrylic acid. The presence of the non-potassium ions in the salt brine will lead to the shielding effect, preventing further absorption of water before osmatic equilibrium is reached [44]. Moreover, the osmatic pressure is low from the beginning as the SAP crystal and salt brine have the same ions. This, compounded with the shielding effect, significantly lowers the water absorption capacity of these SAPs. It is worth mentioning that all SAPs reached approximately 85% of their maximum absorption capacity within 30 minutes of immersion in the 23.3% salt brine as depicted in Figure 2-4a.

The swelling rates of all the SAPs have been plotted in Figure 2-4b. The swelling rate is determined by calculating the weight difference of swollen SAPs between two consecutive periods. The swelling rate is the slope of the water absorption capacity curve in each time interval. Once again, all the SAPs except SE exhibited maximum swell rates at 5 minutes whereas SE reached maximum swell rate after 10 minutes of soaking. The peak swelling rate is reached when the shielding effect dominates the osmatic pressure. As the rates slow and approach zero, the maximum shielding effect has occurred. The maximum swell rate of each of the five SAPs in grams/minute is summarized in Table 2-3. These values are extracted from the point at which peak swelling occurs during the 1440-minute interval (see Figure 2-4b). As previously stated, SAP-SE exhibited the highest swell rate of 2.44 grams/minute, whereas the swelling rates for the other SAPs ranged between 1.01 and 1.69 grams/minute.

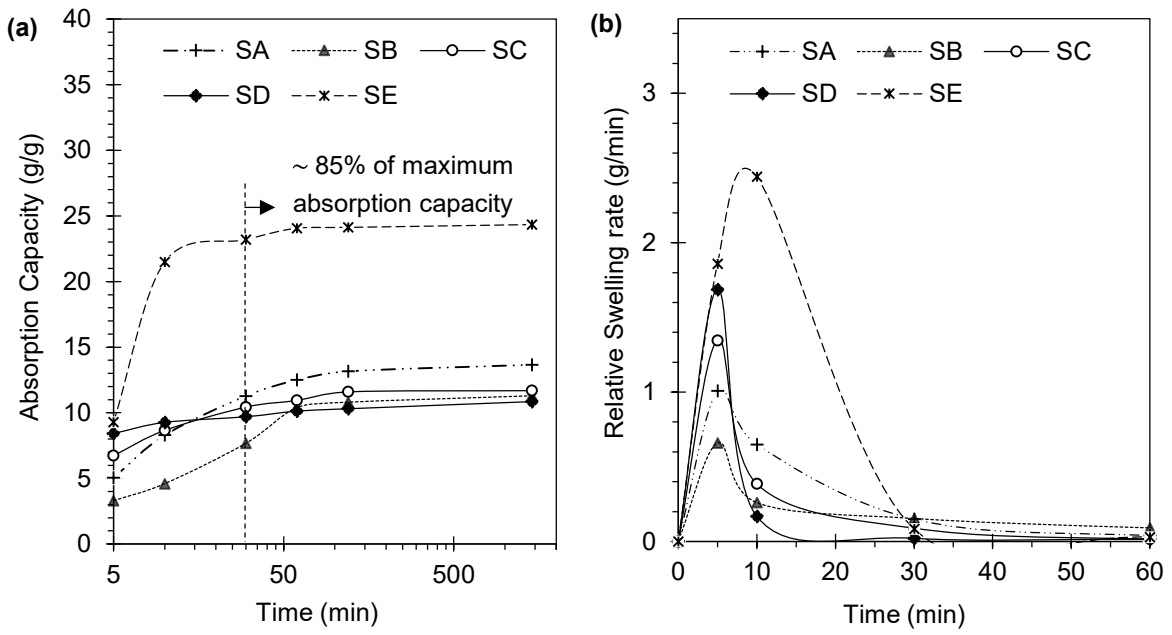

Figure 2-4: (a) the water absorption capacity of SAPs in the 23.3% wt. NaCl brine solution as a function of time, and (b) the relative swelling rate of SAPs as a function of time.

Table 2-3: Maximum swell rate of each SAP.

SAP	SA	SB	SC	SD	SE
Maximum swelling rate (grams/min)	1.01	0.65	1.36	1.69	2.44

The SAPs exhibited significantly lower water absorption capacity in the salt brine solution due to the shielding effect from the sodium and chloride ions. Table 2-4 summarizes the reduction in the swelling capacity of SAPs in a salt brine solution at the end of 1440 minutes of soaking when compared to their water absorption capacity in deionized water (see Table 2-1), as supplied by the SAP manufacturer [42]. The absorption capacity of SAPs in brine solution is decreased by about 97%, 97%, 98%, 94%, and 88% for SAP-SA, SB, SC, SD, and SE, respectively. These sharp drops in swelling rate can be attributed to the poor osmatic pressure in SA, SB, SC, and SD in the salt brine followed by the screening effect. On the other hand, in the case of SE the shielding effect is more dominant in reducing the water absorption capacity.

However, it is worth noting that SE had the least water absorption in the deionized water. This is in part due to potassium salt-based SE particles in deionized water causing a smaller osmotic pressure gradient, which leads to lower water absorption when compared to the sodium salt-based SAPs [45].

Table 2-4: Percent reduction in water absorption capacity in the traditional salt brine deicer

SAP	SA	SB	SC	SD	SE
Reduction in Absorption Capacity (%)	96.58	97.49	97.61	93.97	87.83

2.3.2 Ice melting capacity

The ice melting test is conducted employing the procedure described in Section 2.2.2. The percentage change in the weight of ice cube immersed in the SAP-brine deicing solution with respect to the reference salt brine solution (23.3% wt. NaCl) is calculated according to Eq. **Error! Reference source not found.** of Section 2.2.2 and is taken as a measure of ice melting capacity of a deicing solution in this study. The ice melting studies are conducted for all five SAPs at 5% replacement, 5% addition, and 10% addition at temperatures 0℃, -10℃, -20℃, and -30℃. This resulted in 72 combinations and three tests were performed for each combination. The average weight of ice melt for the reference 23.3% wt. salt brine solution along with all the SAP-deicing solutions is summarized in Table 2-5. These ice melting test results are plotted in Figure 2-5, Figure 2-6, and Figure 2-7 with respect to the reference brine solution for all the SAPs at a given deicing temperature. The positive percentage values shown in these figures represent better performance than the reference salt brine solution.

Table 2-5: Average percentage weight loss of ice cube during ice melting test.

Temp (°C)	**Weight Concentration**	**SA (%)**	**SB (%)**	**SC (%)**	**SD (%)**	**SE (%)**	**23.3% Brine**
0	10% wt. SAP +23.3% NaCl	28.33	29.64	20.85	23.74	14.37	27.73
-10	10% wt. SAP +23.3% NaCl	25.86	26.01	20.46	21.09	14.46	24.47
-20	10% wt. SAP +23.3% NaCl	22.22	25.30	18.76	20.76	15.62	18.47
-30	10% wt. SAP +23.3% NaCl	21.63	21.53	10.53	15.36	15.42	16.05
0	5% wt. SAP +23.3% NaCl	40.21	34.41	26.19	35.26	18.85	27.73
-10	5% wt. SAP +23.3% NaCl	33.73	39.73	28.16	29.98	17.82	24.47
-20	5% wt. SAP +23.3% NaCl	30.82	25.09	18.35	21.34	13.61	18.47
-30	5% wt. SAP +23.3% NaCl	29.58	20.57	18.35	17.69	13.61	16.05
0	5% wt. SAP +18.3% NaCl	34.02	39.92	20.84	20.38	21.45	27.73
-10	5% wt. SAP +23.3% NaCl	37.78	32.25	20.00	17.99	17.32	24.47
-20	5% wt. SAP +18.3% NaCl	26.68	23.99	19.63	19.93	14.17	18.47
-30	5% wt. SAP +18.3% NaCl	22.76	23.04	20.07	14.99	17.28	16.05

From Figure 2-5, the SAPs SA and SB were found to outperform the reference salt brine at all the considered deicing temperatures for 5% replacement, 5% addition and 10% addition. On the other hand, the ice melting capacity of SE at all the deicing temperatures and weight fractions is inferior to the reference salt brine.

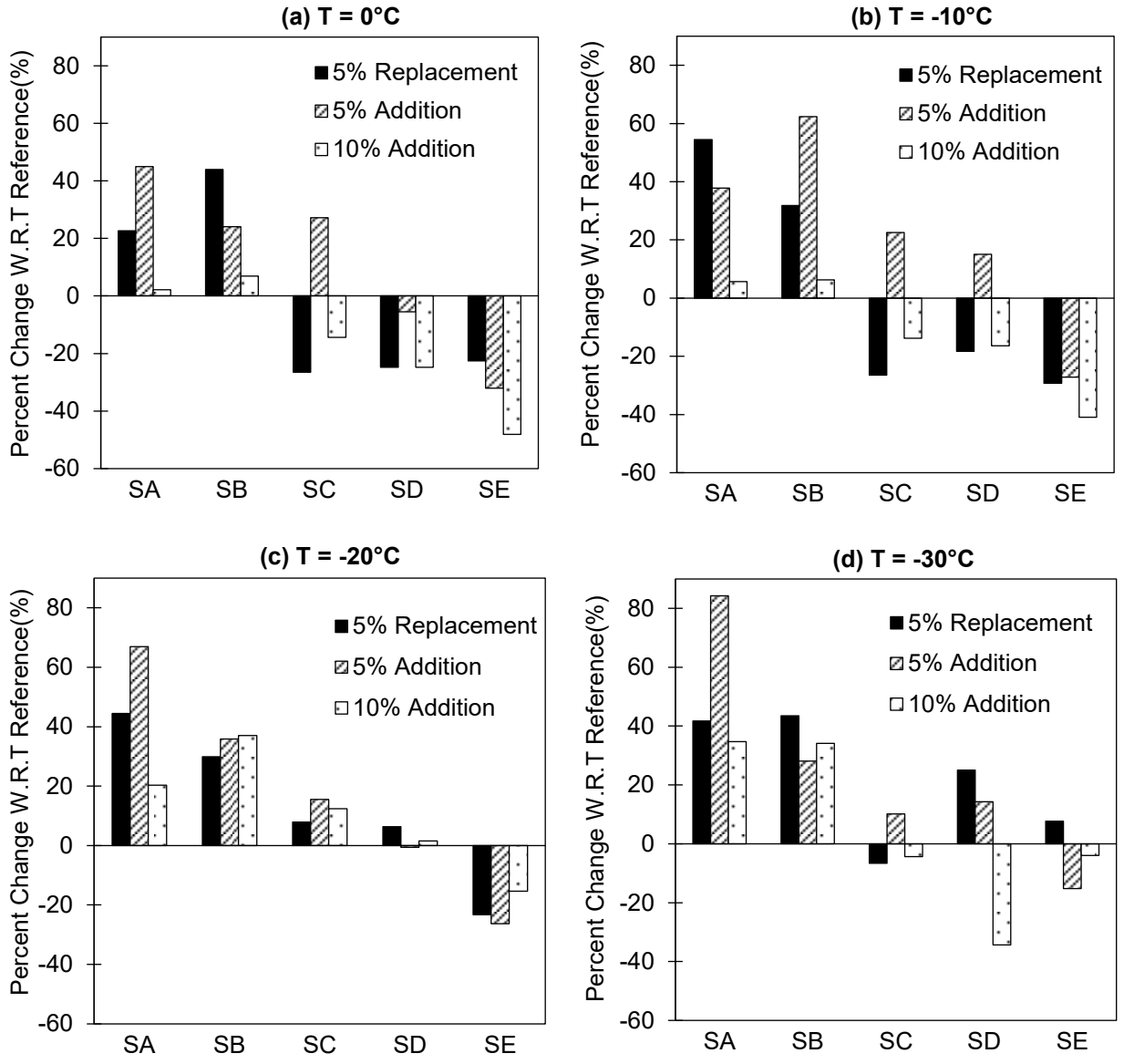

Figure 2-5: Relative weight loss of ice cube at various weight fractions of SAP in salt brine solution at (a) 0°C, (b) -10°C, (c) -20°C, and (d) -30°C.

The influence of the weight percentage of SAPs is demonstrated in Figure 2-6. The discussion on SAPs SE, SC, and SD will be ignored considering their inconsistent and inferior performance. From Figure 2-6, the 10% addition of SAPs SA and SB are not as effective or barely on par with the 5% replacement and 5% addition at all the considered deicing temperatures. It is important to note that, although the ice melting capacity of SA and SB in 10% addition group is still about 40% higher than the ice melting capacity of brine solution at T=-30°C, addition or replacement of a fewer amount (5%) of the same SAP can exhibit equal or higher efficiency (note the 80% outperformance of 5% addition group for SA) at this

temperature. Given the weaker performance of 10% addition of SAP to brine solution coupled with the economic inefficiency of using higher amounts of SAPs, especially at large-scale deicing operations, it is reasonable to proceed with a more detailed analysis of ice melting test focused on the 5% addition and 5% replacement groups.

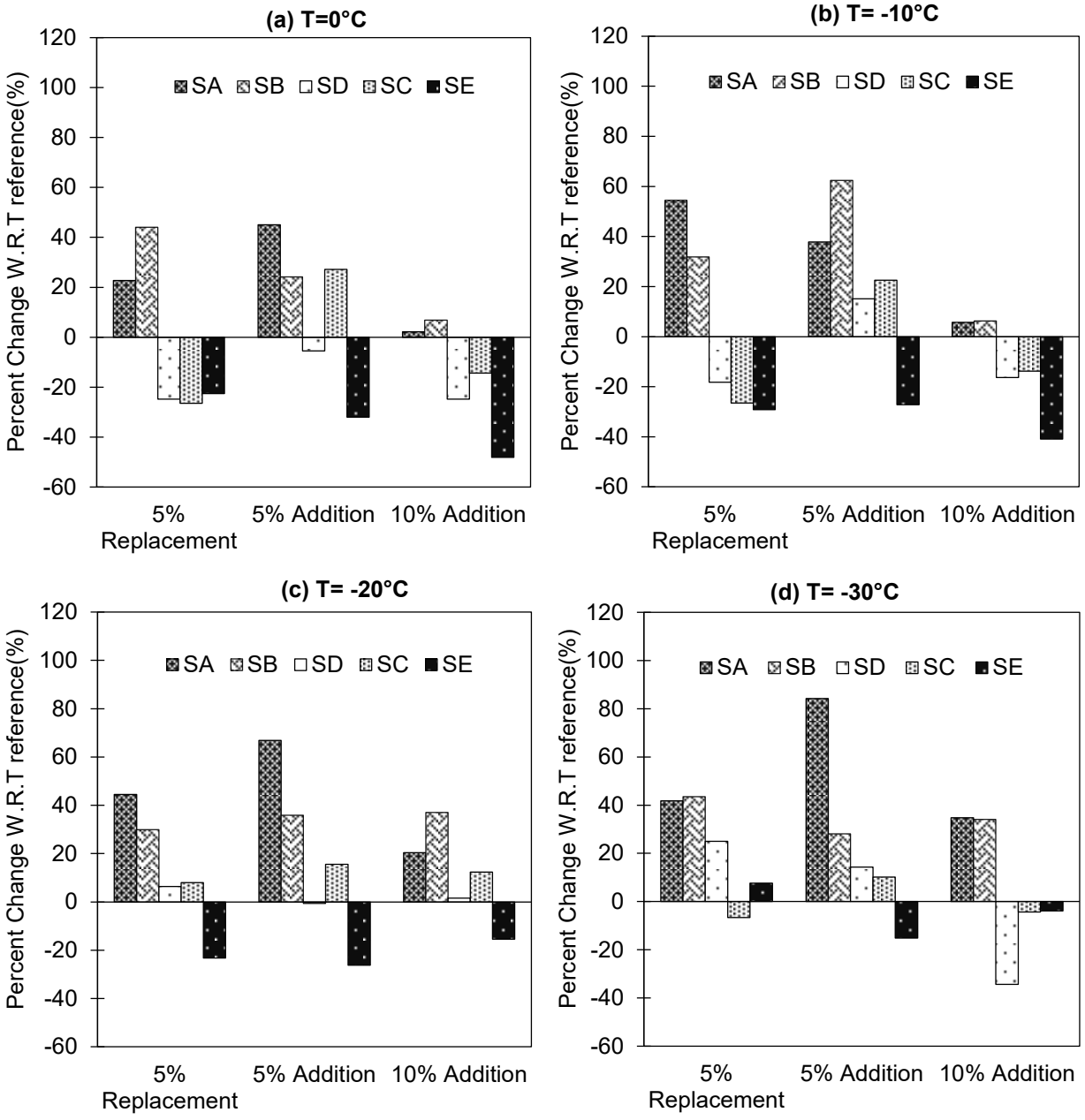

Figure 2-6: Comparison of relative ice melting capacity for 5% replacement, 5% addition and 10% addition at (a) 0°C, (b) -10°C, (c) -20°C, and (d) -30°C.

According to the reported inefficiency of brine solution under extreme low temperatures [26], [46], it is imperative to investigate the efficacy of the alternative SAP-brine groups (5% addition and 5% replacement) under severe cold conditions. The effect of 5% replacement and 5% addition for all the SAPs across all the deicing temperatures is plotted in **Figure 2-7**. The SAP-SA outperformed SB for the

5% addition case and performed better or on par with SB at very low temperatures (less than -10℃) for the 5% replacement case. These changes may be due to the difference in the particle size gradation and the pH value which should be explored in future studies. According to **Figure 2-7**a, substituting NaCl with the 5% SA in brine solution could increase ice melting capacity by up to 60% at T=-10°C and 40% at lower temperatures (T=-20°C and T=-30°C). Consistent with the superior performance of SA, substituting 5% of NaCl with SB results in increased ice melting efficacy (>30%) under extreme low temperatures when compared to the reference brine solution. Even fine particle-sized SAPs (SD and SE), which are normally less effective than large-sized SAPs (as stated previously in Section 2.3.2), show impressive outcomes at extremely low temperatures. For example, substituting 5% NaCl with SD at T=-30°C would increase the solution's ice melting capacity by more than 20% when compared to the brine deicer. **Figure 2-7**b presents the relative mass loss of SAP-brine solution upon the addition of 5% SAPs at different temperatures into the brine solution. The addition of only 5% large-sized SA to the 23.3% wt. NaCl brine solution increased the ice melting capacity by up to 65% at T=-20°C and 80% at T=-30°C. The trend is similar for other large-sized SAP (SB), which could enhance ice melting capacity by 60% at T=-10°C and 40% at T=-20°C. The superior ice melting capacity of SAP-SA and SB is explained next.

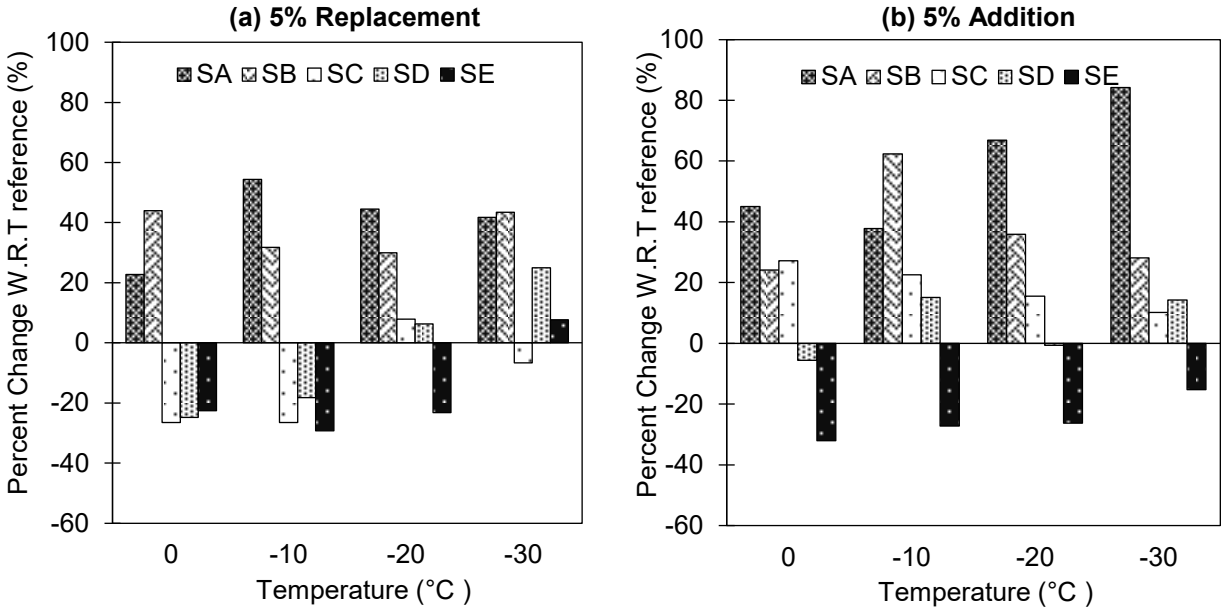

Figure 2-7: The Relative weight loss of ice cube at different temperatures for (a) 5% replacement, and (b) 5% addition.

2.3.3 Explanation for the superior performance of SAPs SA and SB

To test the hypothesis that the SAPs preserve the salinity of water that was bound in their microstructure and release later to melt more ice, salinity tests have been performed. To this end, 46 grams of salt is dissolved in 154 grams of deionized water to produce a 23% salt brine solution. One gram of SAPs SA and SB have been loaded to a porous bag and was dipped in the salt brine solution for 30 minutes. After this, an additional 100 grams of deionized water has been added to the initial 200 grams of solution without removing the SAP bag. This deliberate dilution brings down the concentration of salt to 15.33% from 23%. Ten minutes after the dilution, the SAP bag was removed, and the residual solution was weighed, and water evaporated by slow heating until the salt was left behind. This experiment was repeated thrice for SAPs SA and SB and the weights and salinity of the residual solution,

and the salinity of the water bound in the SAP are summarized in the Table 3. The salinity of the unabsorbed water in the case of SAPs SA and SB are 14.33% and 14.67%, respectively which are both below the 15.33% salinity and suboptimal for ice melting. However, the salinity of the water absorbed in the SAPs SA and SB are 16.2% and 15.93%, respectively which is greater than the salinity of the unabsorbed water by 13% and 8.57%, respectively. Although this difference is minor, based on the past literature, ice melting and freezing points are very sensitive to salt concentration [3, 34] and this preservation of the salt brine salinity in the SAP could have led to the better performance of the SAP blends.

These experiments have been repeated for the SAP SE and the salinity of the unabsorbed water was found to be 11.12% which is significantly below the salt concentrations noted in the SAP SA and SB unabsorbed solutions. However, the salinity of water in the absorbed water in the case of SAP SE is 15.77% which is slightly higher than the nominal 15.33% salinity assuming that there is no SAP bag soaking in the salt brine solution. Despite this higher salinity within the SAP SE, it must be noted that this SAP has a very high-water absorption capacity in the salt brine leaving behind only 28.27 grams of unabsorbed salt brine and the water bound in the SAP did not desorb even after 10 minutes. On the other hand, in the case of SAPs SA and SB, about 139.78 and 142.65 grams of solution was left unabsorbed which can get engaged with the ice melting process and the SAP can desorb more readily when there is a salinity gradient which may be leading to better ice melting capacity. More studies are required to investigate the particle size effect, and desorption of SAPs at low temperatures to comprehensively explain the noted phenomenon which the authors are pursuing in their ongoing studies.

Table 2-6: Salinity tests to validate the hypothesis

	Unabsorbed solution	**Unabsorbed solution**	**Unabsorbed solution**	**SAP absorbed water**	**SAP absorbed water**	**SAP absorbed water**
SAP type	**Soln. wt. (g)**	**Salt wt. (g)**	**Salinity (%)**	**Soln. wt. (g)**	**Salt wt. (g)**	**Salinity (%)**
SA	139.55	20.15	14.44	160.45	25.85	16.11
SA	139.22	20.02	14.48	160.78	25.98	16.16
SA	140.58	19.95	14.19	159.42	26.05	16.34
SB	141.88	21.02	14.82	158.12	24.98	15.79
SB	142.05	20.56	14.47	157.95	25.44	16.10
SB	144.03	21.22	14.73	155.97	24.78	15.89
SE	29.45	3.21	10.89	270.55	42.79	15.81
SE	27.50	3.12	11.35	272.50	42.88	15.73
SE	27.86	3.14	11.27	272.14	42.86	15.74

2.3.4 Skid resistance

The skid resistance of both asphalt and Portland Cement Concrete (PCC) pavements is evaluated after the application of SAP-brine deicer employing a British pendulum tester as described in Section 2.2.3. The percentage reduction in the average BPN for different weight concentrations of SAP-brine

solutions on a dry surface is shown in **Figure 2-8**. Remarkably, SA and SB exhibited the lowest BPN reduction (1% for SA and 2% for SB) compared to dry surface in both Asphalt and PCC pavements across all examined weight concentrations of SAP-brine solutions. This is attributed to a smaller number of large-sized SAP particles for a given weight fraction, leading to less road surface coverage. Furthermore, some of these particles can penetrate the porous surface of the pavements, resulting in a lower reduction of the skid resistance. When compared to standard brine deicers, replacing, or adding 5% of large-sized SAPs to the brine solution not only improves ice melting capability but also preserves surface friction, resulting in increased road safety. In contrast, fine-sized SE demonstrates the highest reduction of about 25-30% in average BPN values for various weight concentrations when compared to dry surfaces. In contrast to the SA and SB, the large number of finer particles in SE for a given weight fraction results in a larger coverage of pavement surface, leading to increased surface skid. Moreover, the higher absorption capacity of SAP SE (as discussed in section 2.3.1) would create a layer between the road surface and the tires, reducing the effective contact area. This diminished contact can lower the friction between the tire and the road surface, leading to decreased skid resistance.

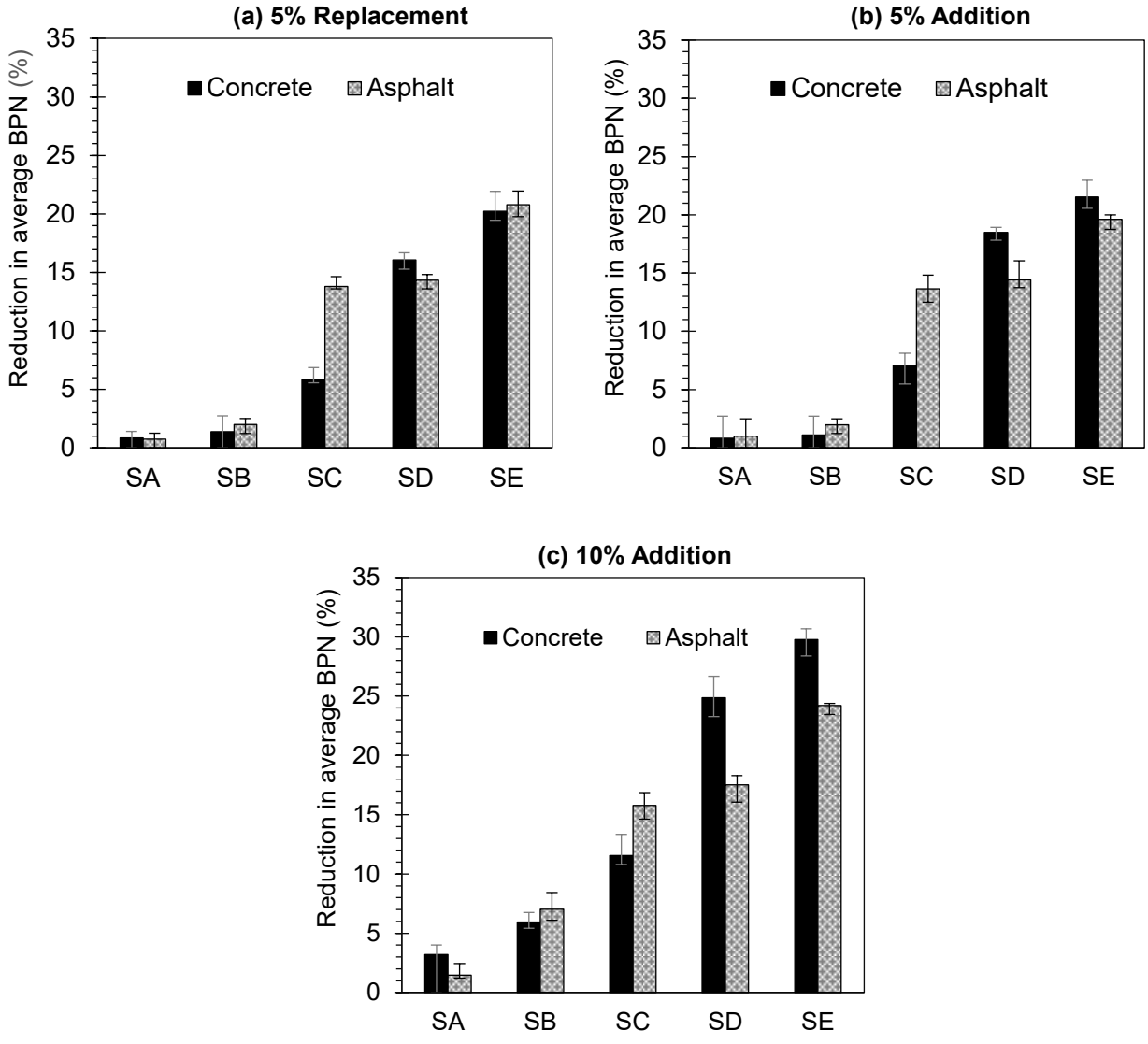

Figure 2-8: Average percentage reduction in BPN for (a) 5% addition, (b) 10% addition, and (c) 5% replacement.

To better illustrate the influence of SAP type and weight concentration on skid resistance reduction, the percentage of BPN reduction is compared for various SAP weight percentages in PCC and asphalt pavement as shown in **Figure 2-9**. While there is no significant difference in BPN reduction between the 5% addition and 5% replacement of SAPs, a substantial reduction in skid resistance is observed when 10% of SAPs are added to the brine solution. These findings align with the results of prior study [25], [47]–[49], indicating that higher weight concentrations of additives in the brine solution contribute to increased slipperiness on the pavement surface.

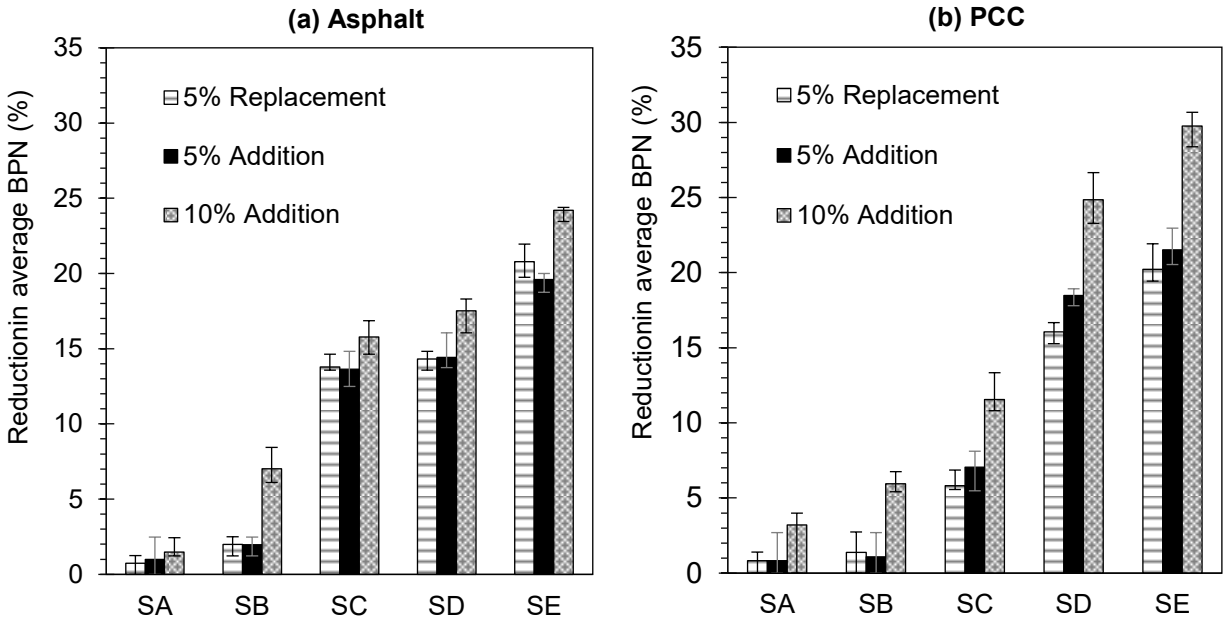

Figure 2-9: Comparison of reduction in the skid resistance between (a) asphalt and (b) PCC pavement.

3 Lowering Freezing Point and Improving Ice Melting Capacity of Deicers with Xylitol and Erythritol

3.1 Introduction

Polyol-based salt brine solution offers a sustainable alternative to traditional deicers with considerably lower environmental impact. Polyols have been used in the food industry for their ability to lower freezing and melting points [50]. Polyols are characterized by multiple hydroxyl groups and are known to decrease the freezing point of water due to the colligative property of the solution. The increase in the total number of dissolved molecules (solute particles) and the enhanced ability to form hydrogen bonds due to the presence of multiple hydroxyl groups result in lower freezing point depression [29], [50]. Polyols, such as sorbitol, maltitol, and mannitol, have been demonstrated to reduce the water freezing point and increase the ice melting capacity of salt brine solutions. Recent studies have shown that sorbitol and maltitol-mixed salt brine solution can reduce the freezing point of water to as low as -38.1°C which is well below the freezing point depression of NaCl brine solution (-21.1°C) [29], [50]. This freezing point depression ability of polyols, combined with increased ice-melting rates, reduces the overall quantity of deicer needed in snow removal operations, which can result in a reduction in corrosion vehicular and infrastructure corrosion, lower surface runoff, and reduction in related adverse effects on soil and aquatic ecosystems [29], [50], [51].

Though polyols have great potential in terms of freezing point depression and ice melting capacity, certain concerns need to be addressed. One of the key concerns associated with polyol-based brine solutions, as with the usage of other organic materials, is their impact on pavement skid resistance. As organic materials tend to be more viscous, polyols having high viscosity may potentially decrease the pavement surface friction and vehicles may thus become vulnerable to slipping in wet conditions. However, a recent study has shown that the addition of polyols such as sorbitol, mannitol, and maltitol increases the overall viscosity of the deicing solution only by a small amount and thus has a minimal impact on the pavement skid resistance [52]. Hence, it is important to ensure that an optimal concentration of polyol is added to the deicing solution to maintain the balance between effective deicing and sufficient pavement skid resistance.

Existing literature has demonstrated the freezing point depression and ice melting capacity of sorbitol, maltitol, and mannitol [52]. However, there is a scarcity of data on the performance of other commonly used polyols, such as xylitol and erythritol, both of which are widely used as alternatives to sugar and to prevent ice crystallization [51]. Their high solubility, which imparts strong freezing point depression capability, makes them potential candidates for addition in brine solution, thus acting as a freezing point depressant and improving the ice melting capacity of salt brine. This study aims to evaluate the effects of two distinct polyols, xylitol and erythritol, on the performance of NaCl brine solutions for snow removal operations. The specific objectives of this experimental study are to quantify the effects of varying concentrations of xylitol and erythritol on the freezing point depression, ice melting capacity, and pavement skid resistance of NaCl brine deicing solutions. It further aims to investigate how different weight fractions of the polyols affect the dissolved oxygen (DO) levels in nearby streams. The findings of this study are aimed at enhancing the effectiveness of traditional chloride-based deicers and reducing the infrastructural costs associated with their usage, thus promoting safer and sustainable approaches to snow removal operations during winter road maintenance.

3.2 Experimental Procedure

This section describes the materials and experimental procedures used in this study to quantify the freezing point depression, ice melting capacity, pavement skid resistance, and DO levels of NaCl brine solutions with various concentrations of xylitol and erythritol. The procedures of these tests are discussed subsequently.

3.2.1 Materials

Erythritol and xylitol utilized in this study were sourced from a commercial supplier in the United States. The molecular structures and physicochemical properties of these polyols are provided in Figure 3-1 and Table 3-1, respectively. Although erythritol (122.12 g/mol) and xylitol (152.15 g/mol) have slightly different molecular weights, the solubility of erythritol is 227.87% lower than that of xylitol at room temperature.

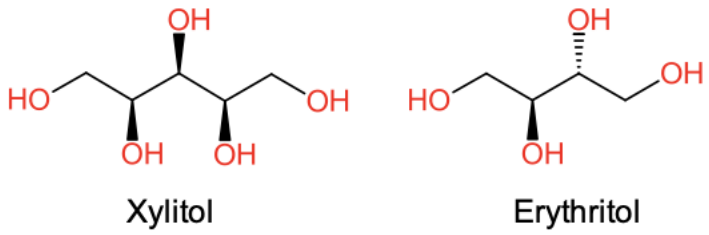

Figure 3-1: Molecular structures of xylitol and erythritol [25].

Table 3-1: Physiochemical properties of polyols used

Properties	Xylitol	Erythritol
Molecular formula	$C_5H_{12}O_5$	$C_4H_{10}O_4$
Molecular weight (g/mol)	152.15	122.12
Water solubility (g/100 g of water at 25°C)	200	61

3.2.2 Preparation of Polyol-based NaCl Brine Deicers

The reference salt brine deicing solution in this study consisted of 23.3 wt% NaCl, which has a freezing point of −21.1°C and is commonly used in deicing operations. The reference deicing solution was modified by adding various weight fractions of xylitol or erythritol as a weight fraction of the resulting solution. Each solution was stirred for 5 minutes to achieve complete solubility of polyol in the 23.3% brine deicing solution. The weight fractions of xylitol and erythritol investigated for freezing point depression tests were: 5%, 10%, and 12.50%. The higher concentrations were excluded due to the relatively low solubility of erythritol and xylitol in the brine solution. For the ice melting capacity test, the following weight fractions were examined for each polyol- 0%, 5%, 10%, and 12.50%. From here on, every percentage that is mentioned will be a weight percentage unless and until exclusively mentioned.

3.2.3 Freezing Point Depression Test

The freezing point depression of the reference and polyol-added NaCl deicing solutions was determined by using a custom experimental setup that consisted of four components (see **Figure 3-2**): (a) a test tube to hold the solution sample, (b) a cooling bath to lower the temperature of the test tube

solution below 0°C, (c) two K-type thermocouples to measure the temperature of the solution and the cooling bath, and (d) a magnetic stirrer to continuously mix the solution. Significantly lower temperatures were achieved in the cooling bath by adding dry ice with acetone (freezing point: −77°C, [28]). To carry out the freezing point depression test, ten milliliters of a specific deicing solution was added to the test tube, which is secured on a vertical stand (refer to Figure 2). Next, a K-type thermocouple, which is connected to a data acquisition system (DAQ) procured from Gain Express Holdings Ltd., was placed at the center of the test tube to monitor the solution's temperature. The test tube was then gradually lowered into the cooling bath (beaker containing acetone). Dry ice was then added to the acetone until the temperature was lowered to around -50 °C, and that temperature was maintained throughout. The temperature of the deicing solution in the test tube was recorded every second up until the end of the test. The solution was stirred continuously using the magnetic stirrer to maintain a homogeneous temperature. Before starting the freezing point tests with polyol-modified brine solutions, a series of validation experiments was performed for solutions with various weight fractions of NaCl.

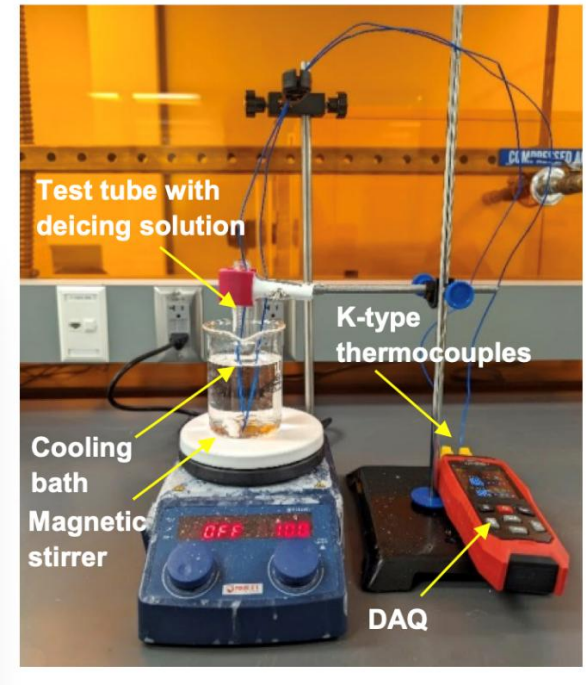

Figure 3-2: Freezing point depression test setup.

3.2.4 Ice Melting Capacity Test

The ice melting capacity (IMC) of the reference and polyol-based NaCl deicing solutions was determined using a custom-built setup shown in **Figure 3-3**. The deicing solutions were prepared by adding erythritol and xylitol to the reference NaCl brine deicer in the following weight percentages: 0%, 5%, 10%, and 12.50%. The IMC of these deicing solutions was then determined at 0°C, -10°C, -20°C, and -30°C. Various test methods are used to evaluate the deicer's IMC, such as the SHRP H205.2 test, the shaker test, the mechanical rocker test, and the ice cube titration test. The SHRP H205.2 and the ice cube titration test provide poor simulation of actual pavement contact, whereas the mechanical rocker test and shaker tests are prone to high variability. This study employed the IMC test developed by Sajid et al. as it mimics the real-world scenario. The deicing solution was maintained at precisely 10 °C to

simulate deicer application conditions [24], [28], [53]. Additionally, this test employed a static setup, with no agitation or shaking, while the ice cube was immersed in the deicing solution for two minutes, unlike the method developed by Sajid et al. [54], to better replicate on-site conditions. To determine the IMC of the deicing solutions, 25 mm ice cubes were first immersed in the cooling bath, which was preset to the desired target temperature using dry ice, and kept in there for 2 minutes. K-type calibrated thermocouple thermometers from Fluke Corporation were used to monitor the temperature of the acetone solution and ice cubes, ensuring the target temperature was maintained. After reaching the desired temperature, the ice cubes were removed from the cooling bath and placed near dry ice to maintain the temperature. An ice cube was then submerged in a 150 ml test solution (NaCl brine with polyol, set at 10°C) for 2 minutes in an insulated container. The weights of the ice cube before and after immersion in the test solution were measured to determine the test solution's IMC. In total, 36 combinations of NaCl brine with varying concentrations of polyols at different temperatures were tested for IMC, with each test being repeated twice.

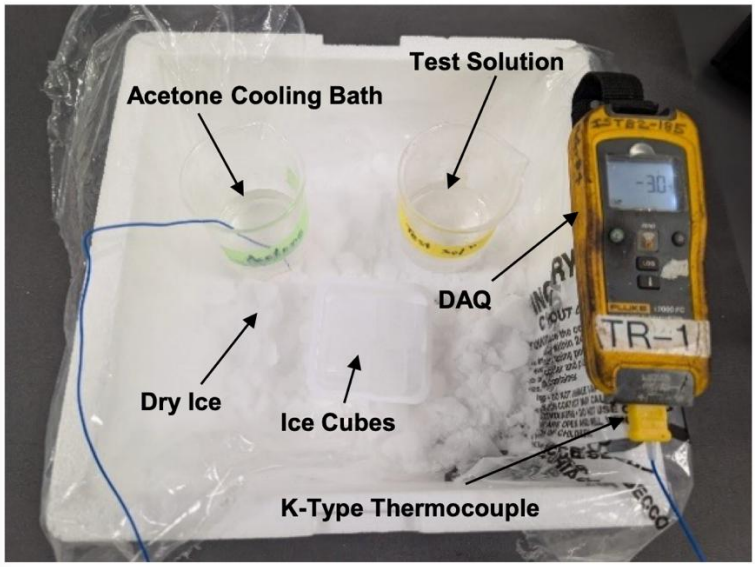

Figure 3-3: Test setup for ice melting capacity tests.

3.2.5 Skid Resistance Test

The metric that evaluates the frictional force generated when a tire slides on a wet pavement surface is termed skid resistance. It measures the slipperiness of a pavement surface and is a key factor contributing to road accidents. High skid resistance helps prevent vehicle tires from skidding on the pavement surface, thereby ensuring safe vehicle control on highways. The skid resistance of pavements can be assessed using various field and laboratory testing methods. Locked Wheel Tester (ASTM E274), Spin Up Tester, Side Force Method (e.g. MuMeter and the Sideway Force Coefficient Routine Investigation Machine (SCRIM)), Fixed Slip Method, Variable Slip Method (ASTM E1859), British Pendulum Tester (ASTM E303), and Dynamic Friction Tester (ASTM E1911) are the commonly used techniques to evaluate skid resistance of pavements [24], [55], [56]. This study assessed the skid resistance of deiced pavement surfaces using the British Pendulum Tester in accordance with ASTM E303 (see **Figure 3-4**). The skid resistance of the pavement surfaces is measured for the reference deicing solution (23.3% NaCl) and the polyol-based deicing solutions (23.3% NaCl combined with different weight fractions of xylitol or erythritol). Skid resistance tests were conducted on a cleaned Portland cement concrete (PCC) pavement surface on the premises of North Dakota State University,

which was built with Portland Cement Type-1 with an approximate air-entrainment of 6%. The relative humidity and temperature during the skid resistance tests were noted to be 18% and 3°C, respectively. The deicing solution was applied to a cleaned pavement surface and was left for 10 minutes. The British Pendulum Tester was then used to measure skid resistance values in terms of British Pendulum Number (BPN). An increase in BPN value indicates greater skid resistance in pavements. For each deicing solution combination, various locations on the PCC pavement surface were tested five times.

Figure 3-4: British Pendulum Tester for Measuring Skid Resistance of Pavement Surface.

3.2.6 Dissolved Oxygen Test

Dissolved oxygen (DO) tests were performed to determine the influence of the reference and polyols-based deicers runoff on the DO levels in a water body, which is an important water characteristic for aquatic life. DO tests were performed using the test method described in Sajid et al [23]. To conduct DO tests, 45 ml of raw lake water, sourced from a nearby lake (Tempe Town Lake), was poured into a 50 ml centrifuge tube, to which 2 µl of deicing solution was added, achieving a concentration of 45 mg/L. The DO level of this mixture is initially measured using a Vernier Optical DO meter, marking the 'Day 0' reading. The mixture is then left undisturbed for 72 hours to obtain a 'Day 3' reading, with the difference in DO levels indicating the oxygen consumed by aquatic microorganisms over this period. The instrument was calibrated using the sodium sulfite solutions at the zero-oxygen point on both occasions. DO tests were conducted for the reference NaCl deicing solution and polyol-mixed deicing solutions. Triplicate tests were conducted for each solution. The DO levels corresponding to the reference and polyol-based deicing solutions are discussed in Section 3.5.

3.3 Results and Discussion

In this section, the experimental results obtained from freezing point depression, DSC, ice melting capacity, skid resistance, and DO tests are presented and discussed for both reference and polyol-based deicing solutions. The performance of different concentrations of xylitol and erythritol in NaCl deicing solution is quantified, and the results are discussed in the following subsections.

3.3.1 Validation of the Freezing Point Depression Experimental Setup

Before conducting tests on the reference and polyol-based deicing solutions, the freezing point depression test setup was validated to confirm the reliability and consistency of the results obtained. For this purpose, freezing point depression tests were conducted for five weight concentrations of NaCl brine solution (5%, 10%, 15%, 20%, and 23.3%) using the procedure described in Section 2.3. This dosage selection was opted to be inline and also to compare the major findings with the available literature [29], [54]. The results obtained from freezing point depression validation tests are based on the literature and provided in **Figure 3-5** [29], [48], [57].

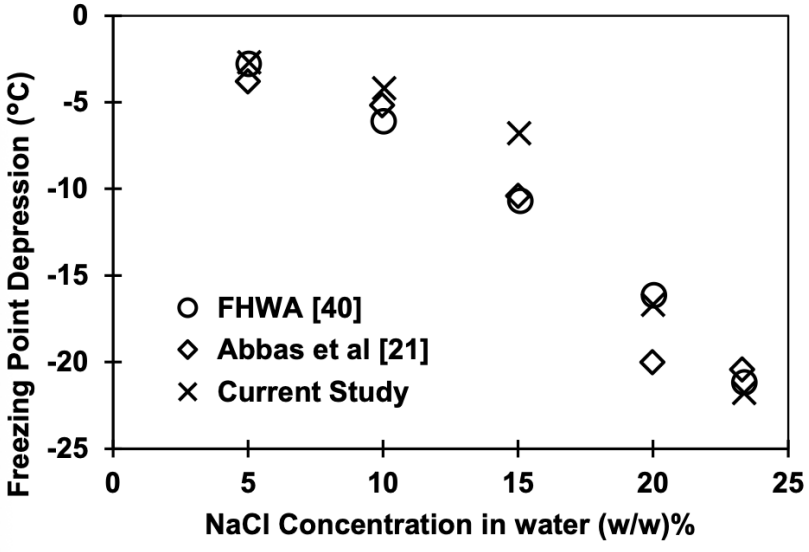

Figure 3-5 shows that the freezing point depression values obtained from the in-house experimental setup aligned closely with the established values, thereby validating the setup's accuracy. Notably, this study did not explore brine solution concentrations exceeding 23.3%, as no further depression of the

freezing point was observed beyond this threshold due to a reduction in ion dissociation of NaCl in water at concentrations greater than 23.3%.

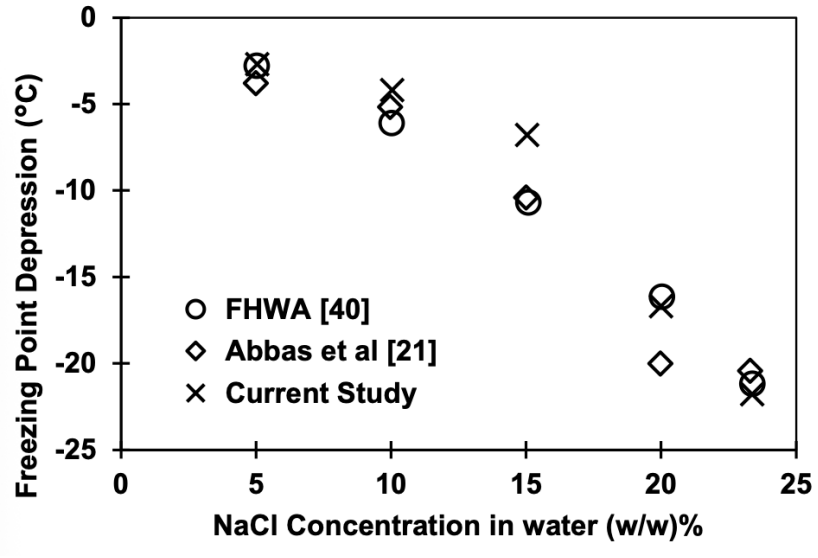

Figure 3-5: Validation of freezing point depression of NaCl brine solution

3.3.2 Freezing Point Depression

Time-temperature cooling curves of the reference and polyol-based NaCl deicing solutions, polyol-brine solutions, were derived from the freezing point depression tests, and the results are discussed in this section. Additionally, the effect of different weight fractions of xylitol and erythritol on the NaCl brine's freezing point is also analyzed in this section.

3.3.3 Xylitol-based NaCl Deicers

In this study, three distinct weight fractions of xylitol ranging from 5% to 12.50% were examined to determine their impact on the freezing point of the reference 23.3% NaCl brine solution. Time-temperature cooling curves for each weight fraction of xylitol obtained from freezing point depression tests are provided in **Figure 3-6**. These curves demonstrated a high degree of consistency across the different weight fractions of xylitol assessed in this study. As observed in Figure 6, most of the xylitol concentrations exhibited a clear horizontal plateau, which signifies the phase transition from liquid to solid, a critical element in identifying freezing point depression.

The freezing points of xylitol-based NaCl deicers, containing varying amounts of xylitol, are provided in **Figure 3-7**. The average freezing point of the different weight concentrations of xylitol: 5%, 10%, and 12.50% based deicers were found to be -27.43°C, -29.77°C, and -35.37°C, respectively. Figure 7 also shows freezing points of the NaCl deicer progressively decrease as the weight fraction of xylitol increases. Initially, as the xylitol's concentration was at 5%, a 25.65% decrease was observed in the average freezing point of the deicer compared to a 23.30% brine solution. The average freezing point of NaCl brine deicer decreased by 36.37% when the xylitol weight fraction increased to 10% in the solution. A more substantial drop of 62% occurred in the average freezing point when the xylitol weight fraction increased from to 12.50%. These results demonstrate that xylitol addition can lead to a substantial

reduction in the freezing point of NaCl deicer and, hence, result in improving the efficiency of snow removal operations in roadways.

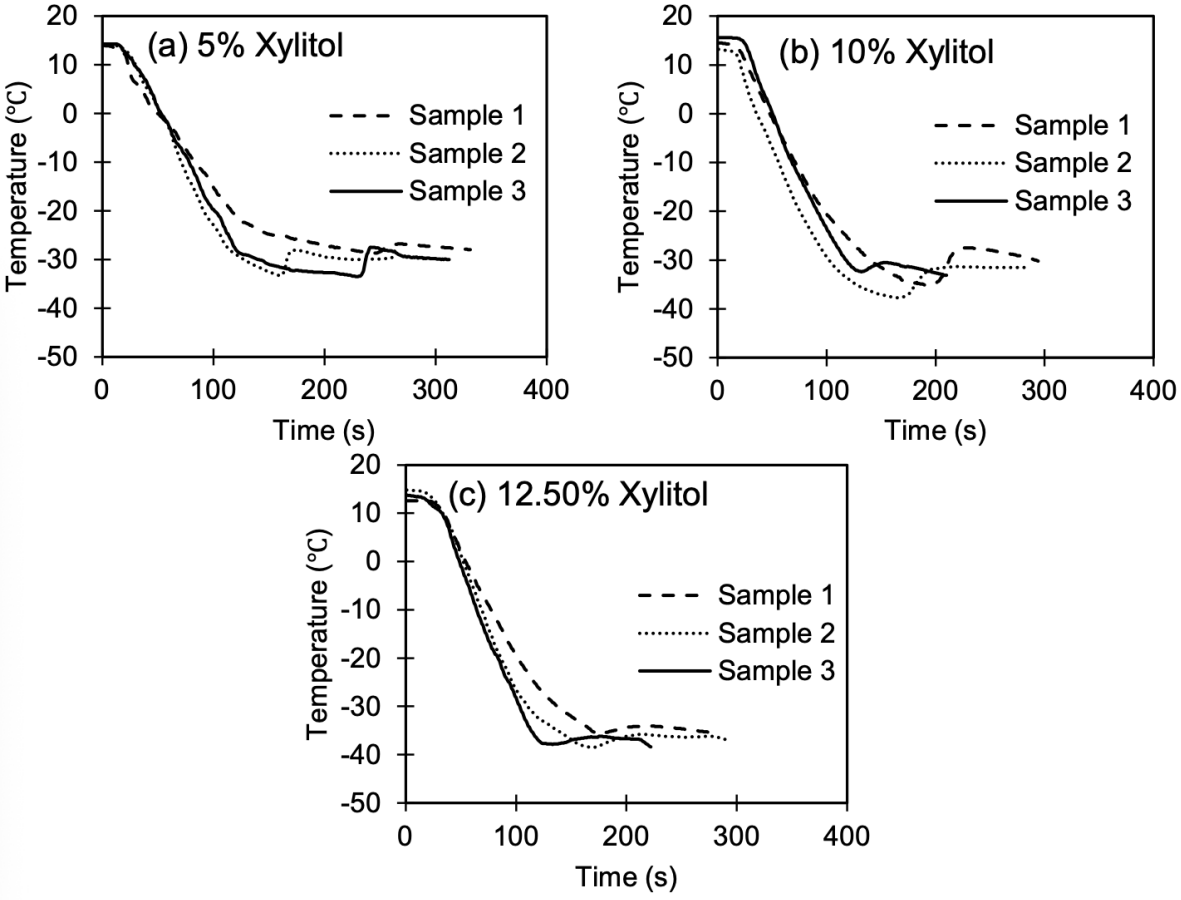

Figure 3-6: Effect of different weight fractions of Xylitol on the freezing point depression of 23.3% NaCl deicing solution (a) 5%, (b) 10 %, and (c) 12.50%.

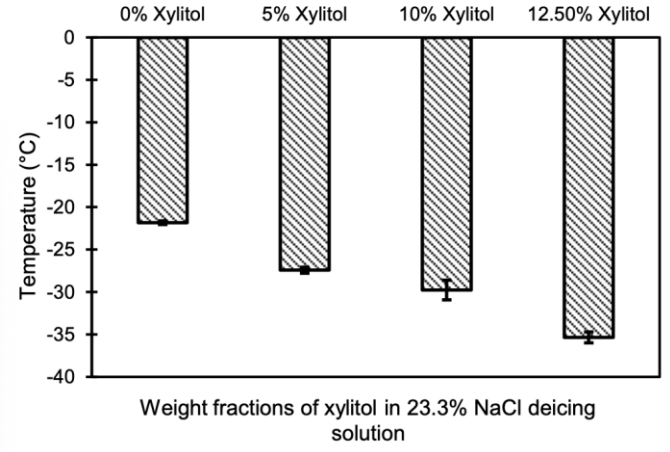

Figure 3-7: Influence of Xylitol on depressing the freezing point of 23.3% NaCl deicing solution

3.3.4 Erythritol-based NaCl Deicers

Freezing point depression tests were conducted for 23.3% NaCl deicer with erythritol concentrations ranging from 5% to 12.50%, and the resulting time-temperature cooling curves obtained from those tests are provided in **Figure 3-8**. The time-temperature curves remained consistent for the whole range of erythritol concentrations studied herein. The average freezing points corresponding to different concentrations of erythritol in NaCl deicing solution are provided in **Figure 3-9**.

As observed in **Figure 3-9**, the freezing point of the NaCl deicing solution decreased almost linearly with an increase in the concentration of erythritol in the deicing solution. The average freezing points of different weight concentrations of erythritol: 5%, 10% and 12.50% based deicers were found to be -27.20°C, -32.20°C, and -37.53°C, respectively. The average freezing point of the erythritol-based NaCl deicer decreased by 47.50% when the erythritol weight fraction in the deicing solution was at 10% compared to a 23.30% brine solution. A further increase in the weight fraction of erythritol to 12.50% resulted in a further 71.92% reduction in the freezing point of the deicing solution. These results exhibit the beneficial role of erythritol in the freezing point depression of the traditional NaCl deicer.

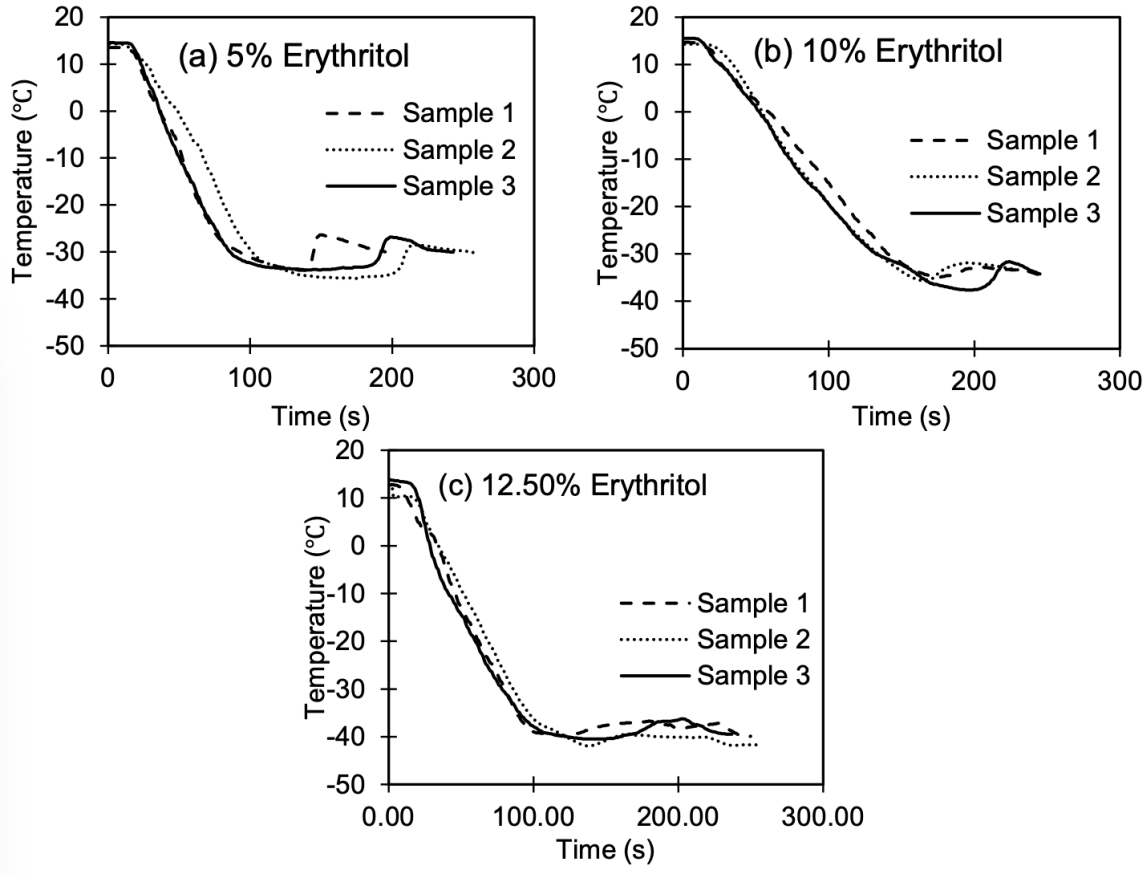

Figure 3-8: Effect of different weight fractions of erythritol on the freezing point depression of 23.3% NaCl deicing solution (a) 5%, (b) 10%, and (c) 12.50%

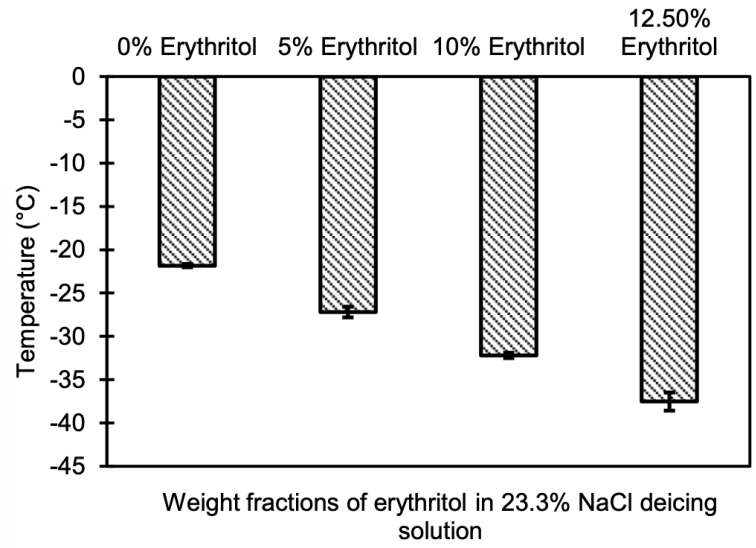

Figure 3-9: Influence of erythritol on depressing the freezing point of 23.3% NaCl deicing solution

The lowest freezing points observed in the case of xylitol-based NaCl deicing and erythritol-based NaCl solution are plotted in Figure 10 alongside the freezing point observed in the absence of either of these polyols in the NaCl deicing solution. **Figure 3-10** further exhibits the marked depression in the average freezing point of the traditional NaCl deicer and highlights the role of polyols in improving the effectiveness of the traditional deicer.

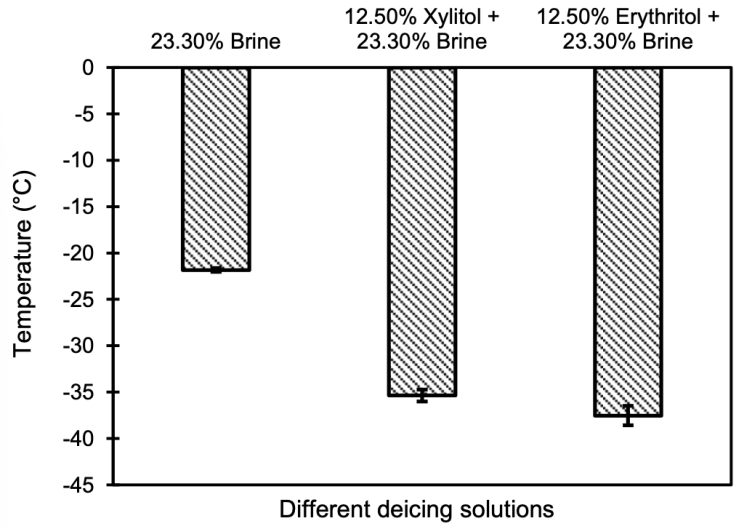

Figure 3-10: Influence of polyols on depressing the freezing point of 23.3% NaCl brine solution

3.3.5 Ice Melting Capacity

The IMC of the reference and polyol-based deicing solutions was determined using the procedure described in Section 2.4. Results obtained from IMC tests are presented in Figure 13 in the form of a percent decrease in the weight of an ice cube submerged in the test deicing solution. Additionally, **Figure 3-11** shows the percent change in the ice cube's weight when immersed in polyol-based deicing solutions compared to the reference NaCl deicer.

The polyol addition resulted in a lower reduction in the ice cube's weight across most target temperatures, except at -20°C and 10% polyol concentration, as per Figure 3-12. The ice melting capacity of salt brine with 12.50% xylitol increased by 12.61% at -10°C, salt brine with 12.50% xylitol exhibited a further increase of 16% at -20°C, and at -30°C demonstrated another increase of 8.34% (see Figure 14(a)). The ice melting capacity of salt brine with 12.50% erythritol increased by 22.24% at -10°C, 23% at -20°C, and 19.46% at -30°C (see Figure 3-12(b)). Compared to all the other concentrations, the 12.50% addition of both erythritol and xylitol performed superiorly when added to the brine solution. The enhanced ice-melting capacity of erythritol-based deicing solutions can be attributed to erythritol's lower solubility in the salt brine compared to xylitol, resulting in undissolved erythritol particles in the salt brine. These undissolved particles can melt ice and form a solution that further aids in melting the ice. The highest ice melting capacity is noted in the case of 12.50% erythritol mixed with 23.3% brine solution at a target temperature of -20°C.

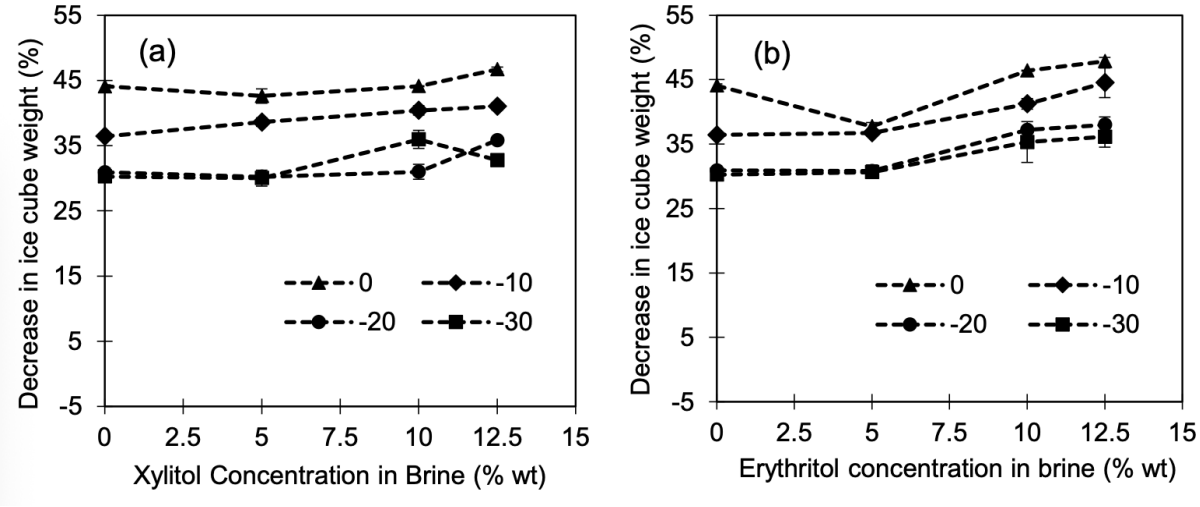

Figure 3-11: Percent decrease in weight of ice cube with an increase in the concentration of (a) xylitol, and (b) erythritol in the 23.3% NaCl deicing solution at different low temperatures.

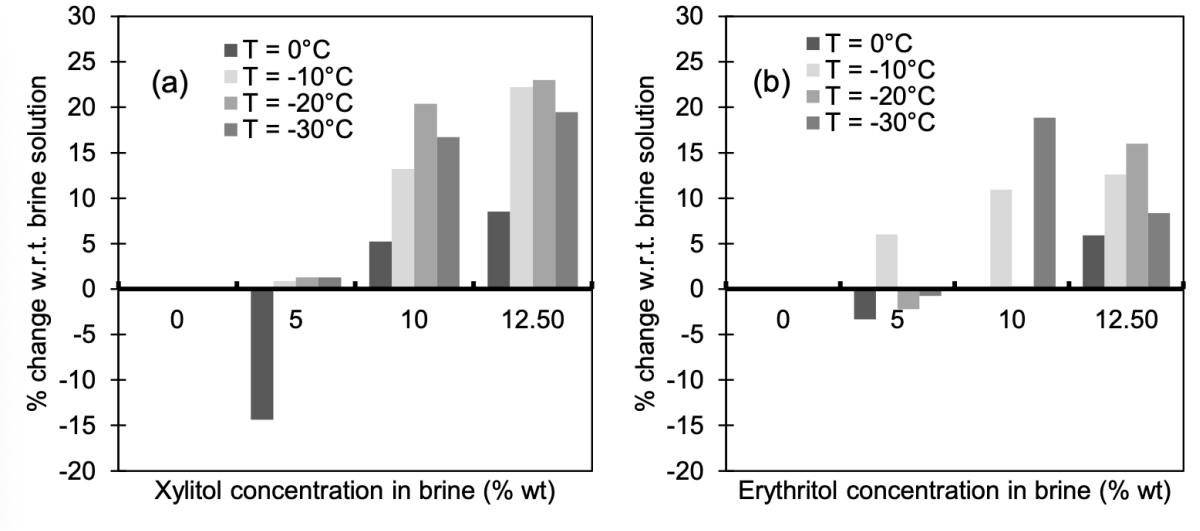

Figure 3-12: Percent decrease in weight of ice cube immersed in (a) 23.3% NaCl brine + xylitol, and (b) 23.3% NaCl brine + erythritol, when compared to the traditional deicing solution (23.3% NaCl brine), at different low temperatures.

3.3.6 Skid Resistance

The skid resistance of PCC pavements after applying reference and polyol-based deicing solutions was measured in terms of BPN (British Pendulum Number) using the procedure described in Section 2.5. The relative humidity (RH) and temperature during the skid resistance tests were measured before conducting the tests. The RH and temperature measured during the test day were 18% and 3°C, respectively. The BPN values of xylitol and erythritol-based deicing solutions are provided in **Table 3-3** and **Table 3-2**, respectively. The average BPN values corresponding to the reference and polyol-based deicing solutions are provided in **Figure 3-13** and **Figure 3-14** for xylitol and erythritol, respectively.

The BPN values observed in **Figure 3-13** and **Table 3-2** exhibited an increase until the application of 12.50% xylitol-based deicing solutions. This also shows that increasing the concentration of polyols in the deicing solutions leads to a decrease in the skid resistance of the pavement surface. The results indicate that 12.50% xylitol-based deicing solutions perform best in terms of generating sufficient frictional force to prevent vehicle tires from skidding. A 4.80% increase in skid resistance is observed for the application of a 12.50% xylitol-based deicing solution. Unlike xylitol, erythritol-based deicing solutions did not exhibit a specific pattern in BPN, with BPN decreasing corresponding to some weight fractions and increasing corresponding to others (see **Table 3-4** and **Figure 3-14**). The results indicate that a 10% erythritol-based deicing solution performs best in terms of generating sufficient frictional force (2.68% decrease compared to a traditional brine solution) to prevent vehicle tires from skidding due to the low crystallization tendency of erythritol.

Table 3-2: Average BPN values of pavement after applying xylitol-based deicer

Sample No.	**Solution**	**BPN** values	**BPN** values	**BPN** values	**BPN** values	**BPN** values	**BPN** values
		1	2	3	4	5	Avg.
1	23.3% Brine	54	55	55	54	53	54.2
2	23.3% Brine + 5% Xylitol	58	58	55	54	55	56
3	23.3% Brine + 10% Xylitol	60	54	58	55	55	56.4
4	23.3% Brine + 12.50% Xylitol	55	55	55	63	56	56.8

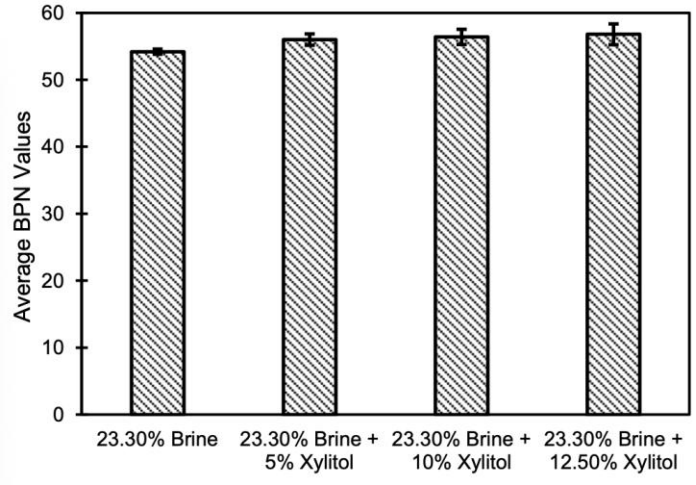

Figure 3-13: Average BPN values of pavement after applying xylitol-based deicer

Table 3-3: Average BPN values of pavement after applying erythritol-based deicer

Sample No.	**Solution**	**BPN values**					
		1	**2**	**3**	**4**	**5**	**Avg.**
1	23.3% Brine	50	50	56	50	55	52.2
2	23.3% Brine + 5% Erythritol	44	48	48	42	47	45.8

Sample No.	Solution	BPN values					
		1	2	3	4	5	Avg.
3	23.3% Brine + 10% Erythritol	49	52	47	56	50	50.8
4	23.3% Brine + 12.50% Erythritol	50	50	55	43	43	48.2

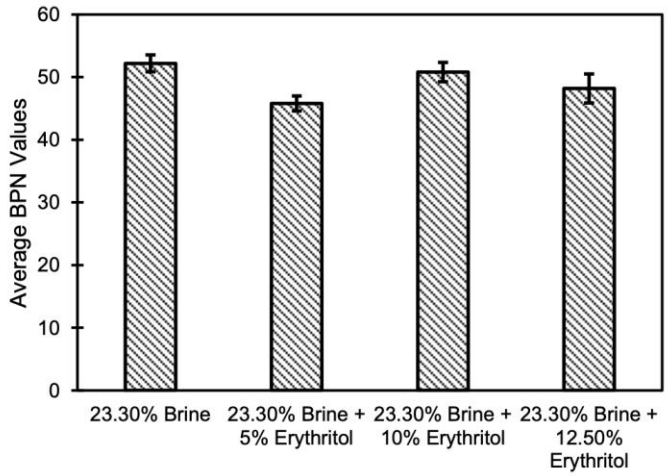

Figure 3-14: Average BPN values of pavement after applying erythritol-based deicer

3.3.7 Dissolved Oxygen (DO) Level

DO tests are conducted using the procedure discussed in Section 2.6. The 3-day DO levels of the reference and polyol-based deicing solutions are summarized in **Table 3-4**. The instrument was calibrated using sodium sulfite solution before taking readings on both instances, and the calibrated reading for zero-level oxygen at 'Day 0' and 'Day 3' was 0.37 mg/L and 0.42 mg/L, respectively. From Table 5, it can be observed that the DO level increased in each of the cases rather than decreasing, which is due to the temperature gradient. The solubility of oxygen decreases with an increase in temperature [58]. As the ambient temperature was around 42°C when the water was collected from the Tempe Town Lake and the test was conducted at 22°C, this temperature gradient was the primary reason behind this anomaly. Fluctuations can also be noticed in the DO results, which are within the normal range. The same water body can show a fluctuation of upto 3mg/L in DO levels. The DO test results indicate that polyol-based deicing solutions resulted in lower depletion of dissolved oxygen when compared to the salt brine deicer. In comparison to the salt brine deicer, the 5% xylitol-based brine solution exhibited an increase of 24% DO, whereas 5% erythritol-based brine solution demonstrated a decrease of 88% DO when mixed with lake water, which can be credited to the high viscosity and low biodegradability of erythritol-based deicing solutions. At this point, it is essential to highlight that only DO tests were performed in this study to determine the depletion of DO when polyol-based brine solutions are used as deicers. Additional detailed tests are outside the scope of this study.

Table 3-4: Three-Day Dissolved Oxygen Test of Stream Water Mixed with Various Deicers

	Day 0		Day 3			
Deicer Solution	Observed Reading	Calibrated Reading	Observed Reading	Calibrated Reading	Consumed DO	Average

Control	9.73	9.36	10.06	9.64	-0.28	-0.28
	9.23	8.86	9.53	9.11	-0.25	
	9.55	9.18	9.91	9.49	-0.31	
Brine	9.03	8.66	9.49	9.07	-0.41	-0.25
	9.75	9.38	9.79	9.37	0.01	
	9.12	8.75	9.51	9.09	-0.34	
5% Xylitol	9.7	9.33	9.6	9.18	0.15	-0.31
	9.11	8.74	9.6	9.18	-0.44	
	9.1	8.73	9.8	9.38	-0.65	
5% Erythritol	9.63	9.26	9.81	9.39	-0.13	-0.03
	9.22	8.85	9.72	9.3	-0.45	
	9.76	9.39	9.33	8.91	0.48	

4 Mitigating Corrosion Damage Steel Employing Biobased Erythritol and Xylitol as Corrosion Inhibitions

4.1 Introduction

Traditional deicing materials, such as sodium chloride (NaCl), magnesium chloride ($MgCl_2$), and calcium chloride ($CaCl_2$), are primarily employed on pavements, sideways, and walk-throughs to remove the snow and ice to ensure safe mobility in winter. These deicers primarily inhibit the bonding of snow and ice to the pavements and help loosen the pre-bonded ice, facilitating its subsequent cleaning through plowing. NaCl is widely used among all deicers because it is relatively inexpensive, effective, easily available, has fewer storage issues, and is easy to apply [59]–[61]. The state Department of Transportations (DoTs) employs salt in granular form and brine solutions form. According to the New York DoT report, approximately 0.95 to 1 million tons of salt are applied annually on state roads to clear the snow and ensure safe mobility [62]. Overall, in the U.S., the utilization of salts to clean the roads in the winter has increased by 200% since 1975 [63]. The annual consumption of salt as a deicing material in the U.S. is growing for two main reasons: a) general expansion of transportation infrastructure [29] throughout the country and b) especially, two-thirds of the U.S. roadways are located in snowy areas [64]. Considering the cost of chloride deicers in the U.S. and Canada, more than 2.3 and 1 billion dollars are spent each year, respectively, to keep the highways clear for mobility [65].

While these chlorides are promising candidates for snow and ice clearance, their usage leads to corrosion-induced deterioration in concrete pavements, bridges, highways, and automobiles. NaCl-based deicers provide a constant supply of chloride ions that lead to the corrosion of rebars within the concrete [48], [49]. The ingress of chlorides compromises the passive layer on the surface of the rebars and initiates corrosion, leading to reduced functionality requiring expensive repairs at a later stage [66]. Several studies are conducted to reduce this chloride-induced corrosion, for instance, a dual oxide layer corrosion inhibitor containing Mg, Al, and Fe in a ratio of 9:2:1, is synthesized which has the ability to absorb the chloride ions and reduce the content of free chloride ions at low temperatures from the surrounding [67]. Steel structures near highways and automobiles undergo accelerated corrosion due to chloride-based deicers on the pavements. The use of chloride-based deicers not only impacts civil engineering infrastructure but also deteriorates automobiles and the environment [68]. In addition to this, the deicing salts also impact the highway maintenance equipment in a variety of ways such as depreciating their values, increasing the equipment downtime, reducing its reliability, reducing equipment service, increasing the repair cost, and safety concerns [69]. Anti-corrosion coatings were recommended to mitigate corrosion in highway equipment. The performance and corrosion mitigation mechanisms have been thoroughly discussed in the literature to protect the value of assets in chloride-based environments [70]. Moreover, these deicing salts also affect the hydration products, leading to scaling and increased alkaline pore solution, which causes osmotic pressure [71]. Several studies attributed the scaling of the concrete to deicers (both corrosive and non-corrosive) and verified their presence within the concrete by conducting physical and chemical studies [72]–[74]. The chloride ions from the deicers react with calcium hydroxide in the cement paste to form expansive oxychloride compounds, damaging the concrete [75]. Magnesium ions can substitute calcium in the (calcium-silicate-hydrate) CSH gel to form (magnesium-silicate-hydrate) MSH that causes cracking and reduced strength [76]. Chloride-based deicers also promote alkali-silica reaction (ASR), further damaging concrete. The use of non-corrosive deicers, such as acetates and formate of potassium, sodium, calcium and magnesium have shown promising results to mitigate corrosion [71]. However, their mass

application is hindered due to its cost and its affinity to corrode certain metals. Moreover, they are also proven to produce scaling effect in concrete [72].

With this, some studies have employed corrosion inhibitors to reduce the corrosiveness of traditional deicers in field with plenty of success. Ideally, a corrosion inhibitor is a compound or a group of compounds that, when added in appropriate dosage, can protect the steel from corrosion [77]. Typically introduced in limited amounts to the corrosive environment, corrosion inhibitors are categorized based on their mechanism of action: anodic, cathodic, or mixed type [78]–[80]. Anodic inhibitors impede the anodic reaction, cathodic inhibitors slow down the cathodic reaction, while mixed-type inhibitors affect both reactions [79]. Regardless of their type, corrosion inhibitors interplay at the metal-solution interface by forming films, achieved via either physical or chemical adsorption. Physical adsorption is particularly favored in corrosion inhibition scenarios due to its spontaneous nature and lack of requirement for external energy [80]. Various corrosion inhibitors that form a protective film on the metal surface via physical adsorption have been very well explored in past [81]. In addition to this, corrosion inhibitors are classified as inorganic, organic, or hybrid, each with distinct protection mechanisms. Inorganic corrosion inhibitor usually inhibits either cathodic or anodic reaction, while organic inhibitors delay both the anodic and cathodic reactions. The choice to opt for either inorganic or organic is associated with factors such as cost, working performance, and ecofriendly nature. Several inorganic chromates and phosphates of calcium, magnesium, and potassium were proven choices as corrosion mitigation in corrosive environment, however, they have been banned due to toxicity concerns [82], [83]. To address this, researchers have been investigating green corrosion inhibitors derived from agricultural products, offering eco-friendly and sustainable alternatives.

A recent study investigated the corrosion inhibition potential of corn-based polyols, namely, sorbitol, mannitol, and maltitol in combination with traditional deicing media [54]. These polyols are renewable, cost-effective, sustainable, and environmentally friendly. Additionally, in combination with traditional deicing solutions, they also enhanced ice melting capabilities and lowered the freezing point without compromising skid resistance [84]. Another study, employed the mannitol and sorbitol to reduce the corrosion damage in of ASTM A615 steel in corrosive environment [79]. Building on this knowledge, the current study explores two other corn-based polyols: erythritol and xylitol. Belonging to the same polyol class, erythritol and xylitol are hypothesized to function similarly in inhibiting steel corrosion. It is pertinent to mention that, herein, the corrosion inhibition potential of erythritol and xylitol is evaluated at neutral pH on ASTM A572, which is primarily used in bridge construction and is often exposed to neutral salt fog from vehicle movement on bridges.

This study investigates the efficiency of erythritol and xylitol, which are four- and five-hydroxyl group polyols, respectively, as corrosion inhibitors in combination with chloride-based deicers. Both erythritol and xylitol are the derivatives of agriculture corn crop and are also employed as sugar substitutes. They are prepared from corn starch via enzymatic hydrolysis or fermentation process [85]–[88]. Their chemical structures and properties are provided in Figure 4-1, and Table 4-1, respectively. This article is organized as follows: In Section 2, the experimental program is elaborated, detailing the surface preparation of the test specimens and explaining the choice of erythritol and xylitol as corrosion inhibitors. This section also covers various characterization techniques used in the study, including accelerated corrosion tests, potentiodynamic polarization tests, the corrosion inhibition mechanism of polyols, adsorption isotherms, and microstructural investigation of corroded specimens. Section 3 comprehensively analyzes the findings derived from these characterization techniques. Finally, Section 4 presents the key conclusions drawn from the study.

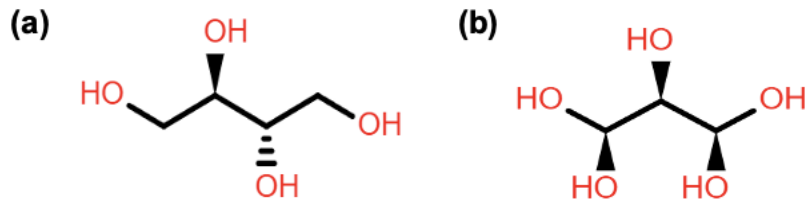

Figure 4-1: Chemical structures of (a) erythritol, and (b) xylitol.

Table 4-1: Properties of erythritol and xylitol.

Polyol	Chemical formula	Molar mass (g/mol)	Density (g/cm^3)
Erythritol	$C_4H_{10}O_4$	122.120	1.45
Xylitol	$C_5H_{12}O_5$	152.146	1.52

4.2 Corrosion Characterization Program

This section provides a comprehensive description of the preparation of steel specimens for accelerated corrosion testing and potentiodynamic polarization analysis. Furthermore, this section describes the methodologies and protocols implemented for characterizing the two selected polyols, i.e., erythritol and xylitol, within the scope of this study.

4.2.1 Preparation of Corrosion Test Specimens

In this research, ASTM A572 steel [89], commonly used in the U.S. construction industry, particularly in bridge construction [47], [54], [90], was chosen to assess the corrosion inhibition effectiveness of erythritol and xylitol. This choice is also pertinent due to the similarity of ASTM A572 steel to other varieties, such as Q460, Q345B, and S355JR, which are extensively utilized in European and Chinese construction sectors [91], [92]. The study involved preparing two sets of ASTM A572 steel specimens, with their chemical composition detailed in a prior study [54]. Disc-shaped specimens with a 19 mm diameter were prepared for the accelerated corrosion tests, while square plate specimens measuring 75mm×75mm were prepared for potentiodynamic polarization tests. To minimize the influence of surface roughness on the efficiency of the polyol-based corrosion inhibitors, both specimen sets underwent a systematic polishing process using silicon carbide sandpapers in a sequential grit order of #60, #120, #220, #400, #600, and #800. A previous study [93], demonstrated how rougher surfaces experience a higher rate of initial corrosion. Polishing would eliminate this difference allowing us to consider the polyol type and concentration as the two parameters of interest. Following the grinding, specimens were thoroughly cleansed with warm water and acetone to eliminate any residual dust or debris. In total, nine specimens were prepared for the accelerated corrosion tests, and an equal number were prepared for the potentiodynamic polarization tests. The methodologies employed in these tests are elaborated in Section 2.2 of this article.

4.3 Characterization Methods

4.3.1 Accelerated Corrosion Test Protocols

The accelerated corrosion test involves disc-shaped ASTM A572 steel specimens exposed to a continuously flowing deicing solution composed of 23% wt. NaCl, with varying concentrations of erythritol and xylitol (0%, 0.5%, 1%, 2%, and 3%). The accelerated corrosion tests are carried out in a controlled chamber, maintaining an ambient temperature of 30°C and humidity levels at 100%, per ASTM B117 standards [94]. The experimental setup includes a feeder for the deicing media, a peristaltic pump to ensure consistent flow, and a disc-shaped specimen positioned on an inclined plane. This inclination prevents the accumulation of the deicing solution on the specimen's surface during the experiment. The setup designed for accelerated corrosion study is illustrated in Figure 4-2. The steel specimens are subjected to a recurring flow (0.5mL/min) of the deicing solution. This flow rate allows enough oxygen to interact with the metal surface to initiate and further progress the corrosion process. A high flow rate may flush the adsorbed polyols from the steel surface, while a low flow rate may not depict accurate corrosion damage. Furthermore, the same flow rate was also employed in the previous study [54]. Photographs of the specimens are taken at 12-hour intervals to visually assess corrosion damage. However, to accurately document early-stage corrosion, especially in specimens subject to 23% wt. NaCl solution without polyols, images are captured every 8 hours. This approach allows for a detailed comparison between the corrosion effects on specimens with and without polyol inclusion in the deicing solution. Finally, to make the corroded area more quantifiable for better comparison, Image J.JS online software [95] was used to calculate the percent damage area on the surface of the ASTM A572 steel specimens, at the end of the testing period (48 hours).

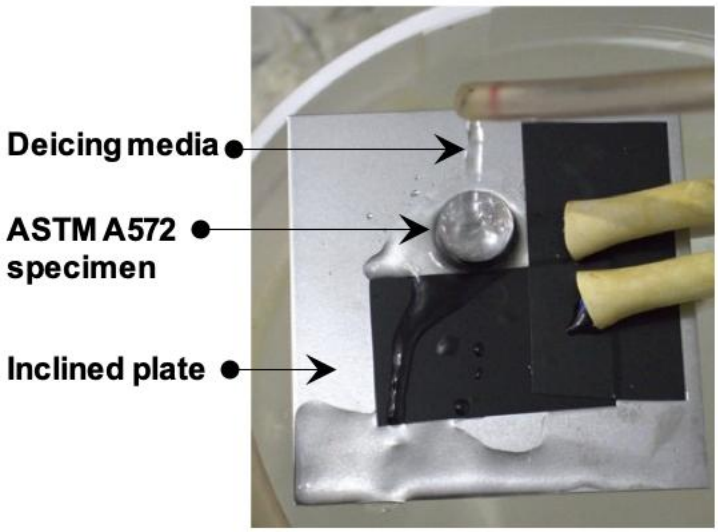

Figure 4-2: ASTM A572 disc-shaped specimen exposed to 23% brine deicing solution containing 0.5%, 1%, 2%, and 3% of polyols at 30°C of ambient temperature and 100% relative humidity.

4.3.2 Potentiodynamic Polarization Test Protocols

In previous research, various electrochemical techniques, such as electrochemical impedance spectroscopy, linear polarization, and potentiodynamic polarization, have been utilized to analyze the immediate corrosion behavior and mechanisms of metals [48], [49], [96]–[100] In the present study, the

potentiodynamic polarization technique is chosen for its ability to provide comprehensive insights into the corrosion mechanism, corrosion rate, and passivation range [97]. This technique is favored for its reproducibility, efficiency, and cost-effectiveness. Tests are conducted using Gamry's Potentiostat Interface E1000. The setup comprises three electrodes: a saturated calomel electrode (SCE) serving as the reference electrode (RE), an ASTM A572 steel square specimen (75mm× 75mm) as the working electrode (WE), and a stainless-steel wire mesh as the counter electrode (C.E.) [54]. To prepare the WE, plastic tape is applied to the surface of the ASTM A572 steel plate, exposing a circular area of 7.07 cm^2 [89]. This prepared electrode is then immersed in a 23% brine solution containing polyols for approximately 2 hours before testing, allowing for the establishment of a stable state potential.

In this experimental configuration, the SCE acts as a benchmark for potential measurements, comparing the potentials between it and the exposed area of the WE. A potential difference applied across these electrodes generates a current, measured per unit area of the WE, known as the corrosion current density [96]. This parameter is crucial as it is directly proportional to the corrosion rate at the WE (Holland 1991). To ensure accuracy and reliability, each polyol concentration test is repeated thrice, although, for clarity, only one representative curve is presented here, as all curves closely overlap with each other. The testing involves varying the potential from a cathodic to an anodic scan within a range of ±500 mV at a scanning rate of 10 mV/sec. Maintaining a high potential and scanning rate is crucial for observing the passivation and pitting behavior of the ASTM A572 steel specimens. Detailed information regarding the potentiodynamic polarization test parameters can be found in the referenced literature (Progress 2009; Holland 1991; Song and Saraswathy 2006). All tests are conducted at an ambient temperature of 25°C.

4.3.3 Surface Characterization of Corroded Specimens

Previous studies have indicated that the addition of polyols in corrosive media can significantly alter the corrosion behavior of ASTM A572 steel specimens [54], [79]. Building on this understanding, the present research aims to explore how the presence of erythritol and xylitol in deicing media affects the formation and nature of corrosion products on ASTM A572 steel surfaces. To this end, this study employs a variety of surface characterization techniques to investigate the types of corrosion products formed and to assess the morphological changes on the corroded surfaces. X-ray diffraction (XRD) analysis is utilized to identify the types of corrosion products and their intensities. The surface morphology of the corroded specimens is examined using scanning electron microscopy (SEM), while energy-dispersive X-ray spectroscopy (EDX) is employed to determine the elemental composition of the damaged surfaces. The preparation of the disc-shaped ASTM A572 steel specimen surfaces for SEM and EDX analysis follows the protocol outlined in Section 2.1. These specimens are then subjected to accelerated corrosion in a deicing solution containing polyols for a duration of 48 hours. Post-accelerated corrosion testing, the specimens are air-dried for 24 hours at room temperature and subsequently coated with gold using sputtering equipment to prepare them for SEM and EDX analysis. Additionally, XRD analysis is performed to corroborate the composition of the corrosion products formed during the accelerated corrosion tests further. For this purpose, a Bruker AXS D8 Discover multipurpose X-ray diffractometer is employed. The diffractometer's laser is precisely collimated and focused on a circular area of 100µm diameter on the specimen surface. Diffractograms are acquired over a 2-theta range of 10-100°, with the generator settings adjusted to 40kV and 30mA to ensure optimal results.

4.4 Results and Discussion

This section presents results obtained from the accelerated corrosion tests and potentiodynamic polarization tests about the corrosion inhibition performance of erythritol and xylitol. Additionally, adsorption isotherms are employed to elucidate the corrosion inhibition mechanism of the two mentioned polyols. The final sub-section explains the surface morphology of the corroded specimens and the characterization of the corrosion products formed during the accelerated corrosion studies.

4.4.1 Accelerated Corrosion Results

In this research, accelerated corrosion tests were conducted to assess the impact of various fractions of considered polyols on the corrosion of ASTM A572 steel disc specimens. These tests involved exposing the specimens to a standard deicing solution (23% wt. NaCl) and observing the surface corrosion over 48 hours, both with and without the addition of polyols (erythritol and xylitol). Corrosion progression was tracked through photographs taken every 12 hours. Initially, at t = 0 hours, all the specimens are free from any type of corrosion, and they show uniform polished surfaces. However, as exposure time increased, varying levels of corrosion were observed, depending on the weight fraction and the type of polyol used. Specimens exposed to the standard deicing solution without polyols exhibited significant corrosion when compared to those containing polyols.

Specific findings include: 1) traditional deicing solution (no polyols): noticeable corrosion began after 8 hours, covering almost 80% of the surface area by 48 hours (see Figure 4-3**,** and Figure 4-6), 2) deicing solution with erythritol (0.5%, 1%, 2%, 3%): corrosion started after 12 hours and showed minimal progression over 48 hours. At the end of the testing period, 30.01%, 24.83%, 32.11%, and 26.52% of the total surface area was corroded for 0.5%, 1%, 2%, and 3% erythritol, respectively (see Figure 4-4**,** and Figure 4-6). Specimens with 2% and 3% erythritol had the least corrosion, starting after 24 hours with no further increase (see Figure 4-4), 3) deicing solution with xylitol (0.5%, 1%, 2%, 3%): exhibited superior corrosion inhibition. The 0.5% xylitol solution showed minor corrosion after 12 hours of exposure without further progression. Higher concentrations of xylitol (1% to 3%) demonstrated minimal to negligible corrosion, with only minor pitting observed by the end of the test period, i.e., 48 hours (see Figure 4-5). The percent corroded area for 0.5%, 1%, 2%, and 3% of xylitol is determined to be 9.39%, 7.26%, 12.40, and 5.36% of the total area, respectively (see Figure 4-6). This delayed corrosion can be attributed to the chelating properties of polyols, which adsorb the polyols onto the metal surface, blocking active sites and inhibiting anodic dissolution [101]. The accelerated corrosion tests provide visual evidence supporting the corrosion inhibition potential of polyols in the deicing solution (23% wt. NaCl solution). Moreover, the corrosion inhibition mechanism and corrosion rates are quantified using the potentiodynamic polarization test in the next section. The detailed mechanism of corrosion inhibition by these polyols is further discussed in Section 3.4.

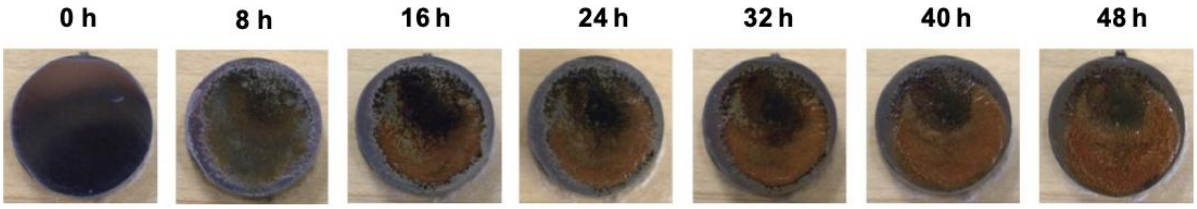

Figure 4-3: Periodic visual appearance of ASTM A572 disc-shaped specimen exposed to 23% brine solution at 30°C of ambient temperature and 100% relative humidity.

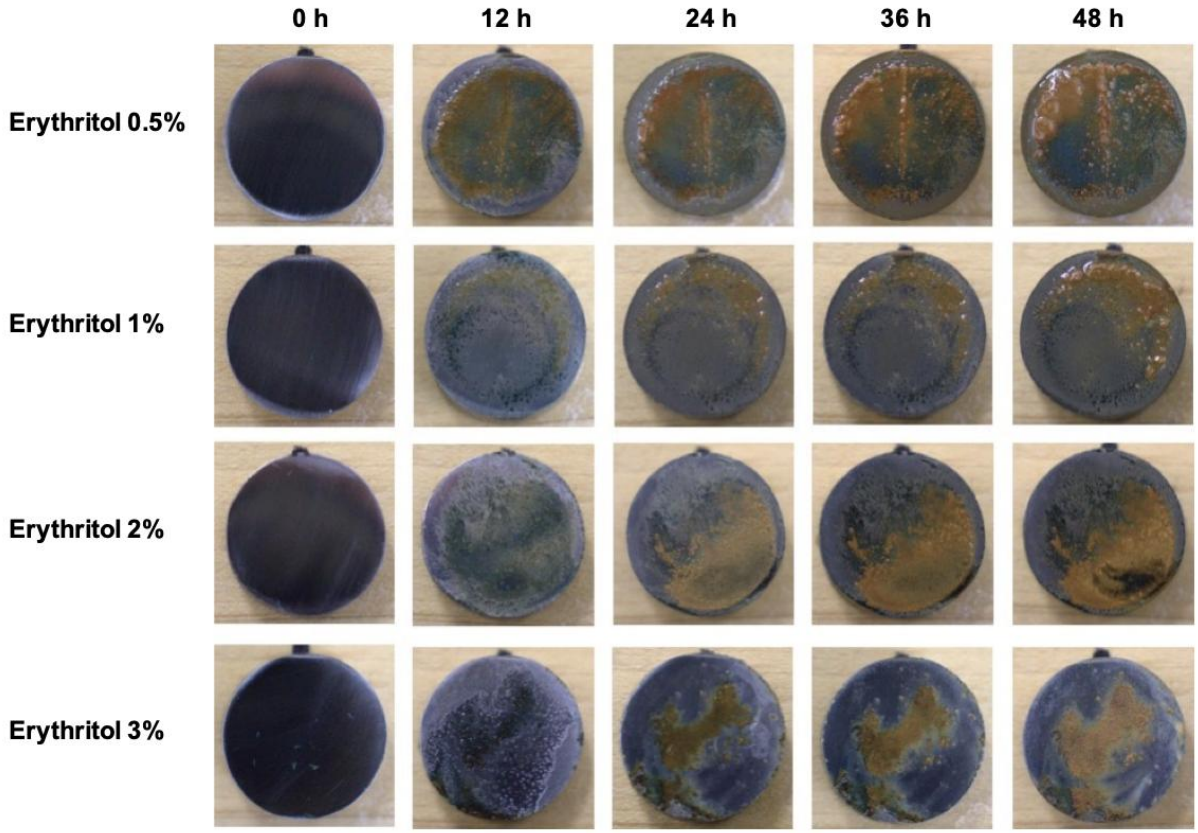

Figure 4-4: Periodical visual appearance of ASTM A572 disc-shaped specimen exposed to 23% brine solution containing 0.5%, 1%, 2%, and 3% of erythritol at 30°C of ambient temperature and 100% relative humidity.

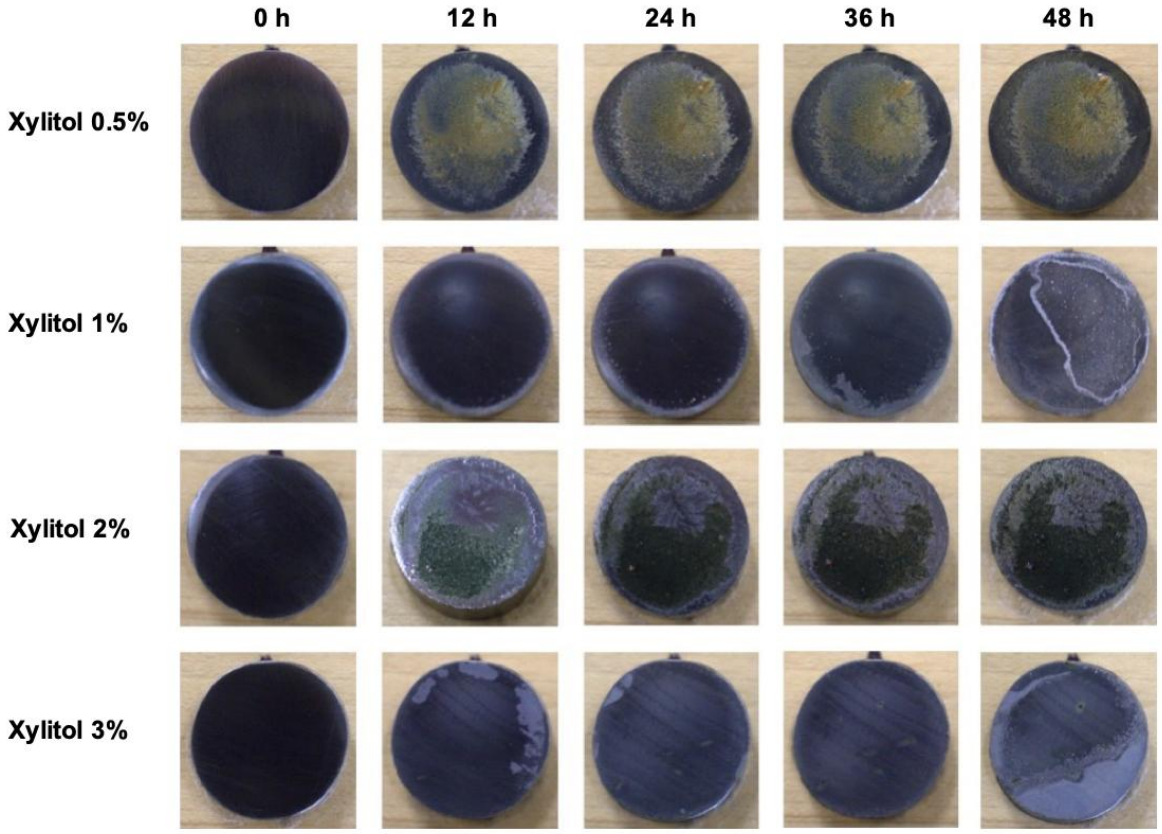

Figure 4-5: Periodical visual appearance of ASTM A572 disc-shaped specimen exposed to 23% brine solution containing 0.5%, 1%, 2%, and 3% of xylitol at 30°C of ambient temperature and 100% relative humidity.

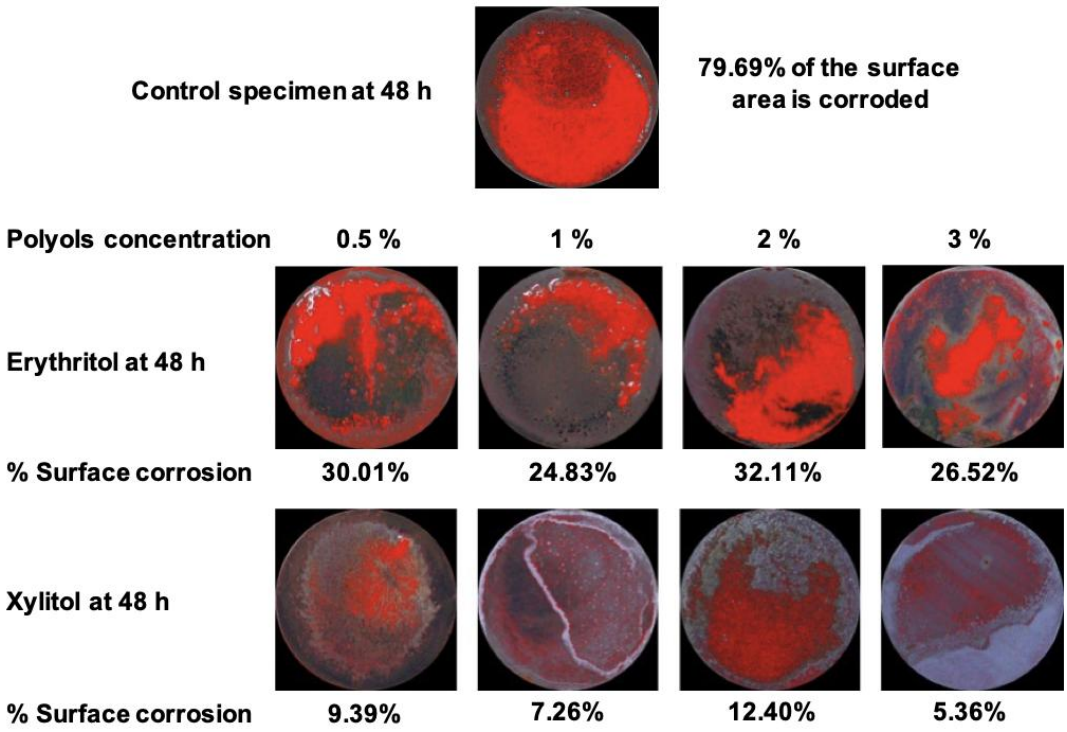

Figure 4-6: Percent corroded area of ASTM A572 disc-shaped specimen exposed to 23% brine solution with and without 0.5%, 1%, 2%, and 3% of erythritol and xylitol.

4.4.2 Potentiodynamic Polarization Results

Building upon the qualitative assessment of corrosion damage conducted through the accelerated corrosion tests, the potentiodynamic polarization test aims to quantify the corrosion rates, corrosion current densities, and corrosion mechanism of ASTM A572 steel. This test is conducted in the absence and presence of erythritol and xylitol at varying concentrations of 0.5%, 1%, 2%, and 3%. The procedure employed for these tests is detailed in Section 2.2.2.

The potentiodynamic polarization curves obtained from the polarization tests provide a detailed insight into the electrochemical processes occurring at both the anodic and cathodic sites. Typically, such curves exhibit two distinct branches: anodic branch, where the potential (V) increases with the increase in logarithmic current (A/cm^2), and cathodic branch, wherein the potential (V) decreases as the logarithmic current increases. Within the cathodic branch, two primary regions can be identified: oxygen dissolution followed by hydrogen evolution, resulting in a reduction of the passive film [66], [102]–[104]. Within the anodic branch, several regions can be distinguished: active corrosion region, characterized by an increase in current density with minimal change in potential, passive corrosion region, where a passive oxide film is formed on the steel surface, maintaining a constant corrosion current density while the potential increases. Eventually, the passive oxide layer dissolves, initiating pit formation [105].

Figure 4-7 and Figure 4-8 display the potentiodynamic polarization curves of ASTM A572 steel in the presence of varying concentrations (0.5%, 1%, 2%, and 3%) of erythritol and xylitol. From both the

figures, it can be observed that all the polarization curves exhibit typical Tafel behavior, demonstrating a linear relationship between logarithmic current and potential. The presence of erythritol and xylitol in the deicing solution causes a shift in the polarization curves towards lower current regions, indicating the corrosion inhibition potential of both the erythritol and xylitol. Additionally, all curves shift towards a more positive potential (more noble) in the presence of polyols, suggesting a retardation of electrochemical reactions [106], [107]. This retardation signifies less anodic dissolution and hence corrosion protection to the ASTM A572 steel specimens. Comparing erythritol and xylitol, the curves for xylitol shifted more towards the noble potential region, indicating better corrosion protection performance [108], [109]. These findings align with observations from accelerated corrosion tests, further supporting xylitol's superior corrosion inhibition capability. The polarization cures are utilized to determine the corrosion current densities and corresponding corrosion rates for varying concentrations of erythritol and xylitol, which will be discussed in the subsequent section.

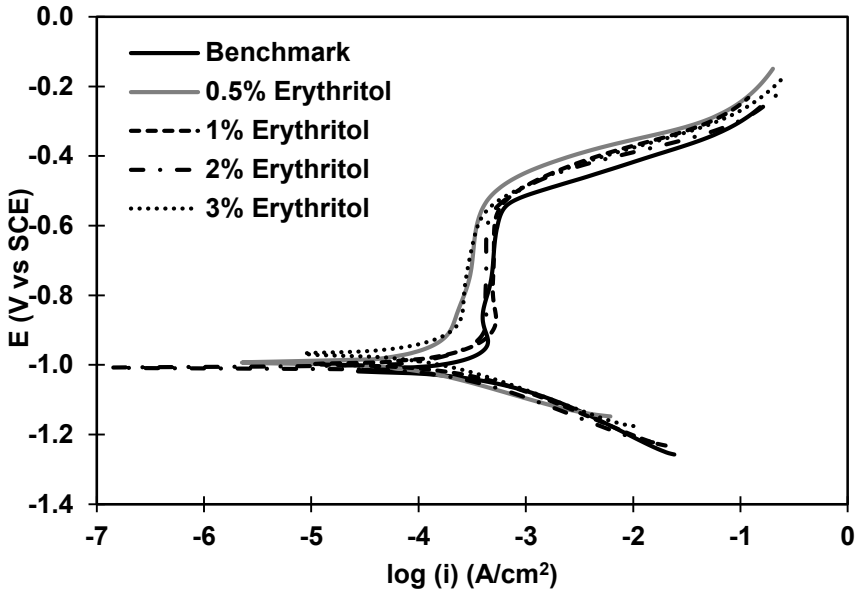

Figure 4-7: Potentiodynamic polarization curves obtained for ASTM A572 steel in the presence of 0.5%, 1%, 2%, and 3% of erythritol in salt brine deicer.

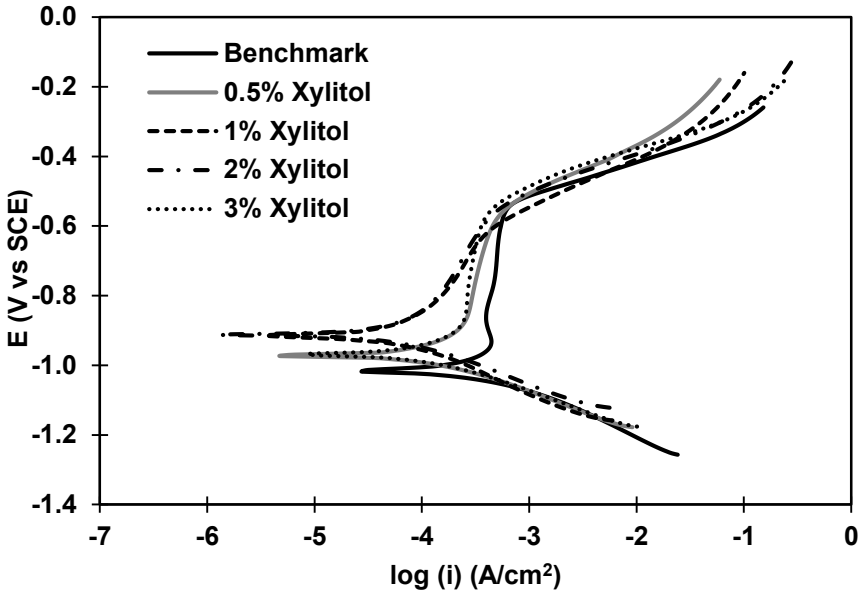

Figure 4-8: Potentiodynamic polarization curves obtained for ASTM A572 steel in the presence of 0.5%, 1%, 2%, and 3% of xylitol in salt brine deicer.

4.4.3 Tafel Extrapolation

This study employs the Tafel extrapolation technique to quantify electrochemical parameters like corrosion potentials (E_{corr}), corrosion current densities (i_{corr}), and Tafel slopes (anodic slope, β_a and cathodic slope, β_b) [110]. Studies in the past indicate that Tafel extrapolation can be conducted by considering either the anodic branch, cathodic branch, or both [66], [105], [111]–[113], provided that at least one branch exhibits Tafel behavior wherein the logarithmic current density shows a linear variation with the potential of the WE [66], also known as linear or Tafel section [49], [114], [115]. Considering both anodic and cathodic branches is advantageous for determining the Tafel slopes. However, determining the Tafel slope and respective corrosion current density using a single branch is also possible. While employing a single branch, the cathodic branch is preferred due to its typically prominent Tafel region compared to the anodic branch, which may exhibit deviation due to passivation, pitting behavior, and surface deterioration [116].

In this study, we considered cathodic branches for Tafel extrapolation because the potentiodynamic polarization curves obtained from ASTM A572 steel specimens display a more prominent Tafel region in the cathodic curves compared to their respective anodic counterparts. A detailed explanation of the Tafel exploration is provided elsewhere [117]. The different polarization parameters obtained via Tafel analyses are listed in Table 4-2**,** while the corrosion current densities are displayed in Figure 4-9. More explicitly, the corrosion current density deicing solution without any polyol was 63.169 $\mu A/cm^2$. Incorporating polyols in the deicing solution reduced the corrosion current densities, ranging from of 20.378 $\mu A/cm^2$ to 4.356 $\mu A/cm^2$. Deicing solution with erythritol (0.5%, 1%, 2%, 3%) revealed corrosion current densities of 20.378 $\mu A/cm^2$, 14.591 $\mu A/cm^2$, 16.292 $\mu A/cm^2$, and 7.721 $\mu A/cm^2$, respectively. Similarly, deicing solution with xylitol (0.5%, 1%, 2%, 3%) showed corrosion current densities of 12.135 $\mu A/cm^2$, 5.652 $\mu A/cm^2$, 8.324 $\mu A/cm^2$, and 4.356 $\mu A/cm^2$, respectively. With these values, it is clear that the presence of the polyols in the deicing media reduced the corrosion

current densities substantially. Moreover, the reduction in corrosion current densities of the deicing media containing erythritol and xylitol relative to the benchmark solution (no polyols) is quantified in terms of percentage corrosion inhibition efficiency (CIE) employing the following equation

$$CIE\,(\%) = (i^{a}_{corr} - i^{p}_{corr})/i^{a}_{corr} \times 100 \qquad \text{Eq. 1}$$

where CIE represents the percent corrosion inhibition efficiency, i^{a}_{corr} is the corrosion current density without polyol and i^{p}_{corr} is the corrosion current density with polyols (erythritol or xylitol) concentrations in the deicing media. Mean CIE values for different concentrations of polyols (erythritol or xylitol) are displayed in Figure 4-10. Figure 4-10 shows that the addition of 0.5%, 1%, 2%, and 3%, of erythritol in deicing media revealed a CIEs of 68%, 77%, 74%, and 88%, respectively. On the other hand, the addition of xylitol led to CIEs of 81%, 91%, 87%, and 93%, respectively. With these CIEs, it can be concluded that the addition of a very limited quantity (0.5%) of erythritol and xylitol into the deicing media resulted in a pronounced effect on the CIE of polyols. The corrosion rates are determined using the following equation, conforming to ASTM G102 [99]

$$Corrosion\,rate\left(\frac{mm}{year}\right) = 3.27 \times 10^{-3} \times \frac{i_{corr}}{\rho} \times EW \qquad \text{Eq. 2}$$

where, i_{corr} is the corrosion current density, which is measured from the Tafel graph in $\mu A/cm^2$, ρ is the density of steel taken in g/cm^3, while $E.W.$ is the equivalent weight of alloy, and in the current case it is determined to be 28.25. The average values of the corrosion rates are displayed in Figure 4-11. It can be noticed that the average corrosion rates $(mm/year)$ corresponding to the deicing media containing various concentrations of erythritol and xylitol are substantially reduced in comparison to the traditional deicing media (23% wt. $NaCl$). The corrosion rate for the traditional deicing solution is recorded to be 0.742 $mm/year$, whereas, for erythritol concentrations of 0.5%, 1%, 2%, and 3%, the corrosion rates are 0.239 $mm/year$, 0.171 $mm/year$, 0.191 $mm/year$, and 0.090 $mm/year$, respectively. Correspondingly, for xylitol concentrations of 0.5%, 1%, 2%, and 3%, the corrosion rates are determined to be 0.142 $mm/year$, 0.066 $mm/year$, 0.097 $mm/year$, and 0.051 $mm/year$, respectively. The percent reduction in corrosion rates compared to the benchmark solution is calculated as 67.74%, 76.90%, 74.21%, and 87.77% for erythritol, and 80.79%, 91.05%, 86.82%, and 93.10% for xylitol, for concentration of 0.5%, 1%, 2%, and 3%, respectively. Overall, the maximum reduction (93.10%) in corrosion rate is recorded in the presence of 3% xylitol. The mechanism underlying the improvement in CIEs and reduction in corrosion rates due to erythritol and xylitol incorporation are discussed comprehensively in the subsections.

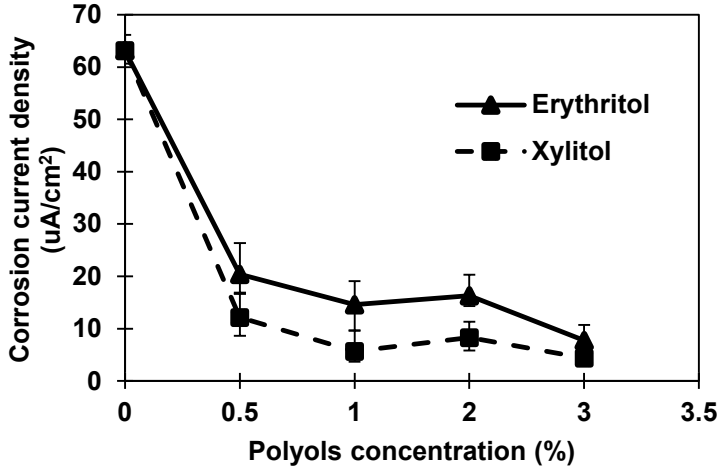

Figure 4-9: Decrease in corrosion current densities in ASTM A572 steel specimens as a function of weight concentrations of erythritol and xylitol in salt brine deicer.

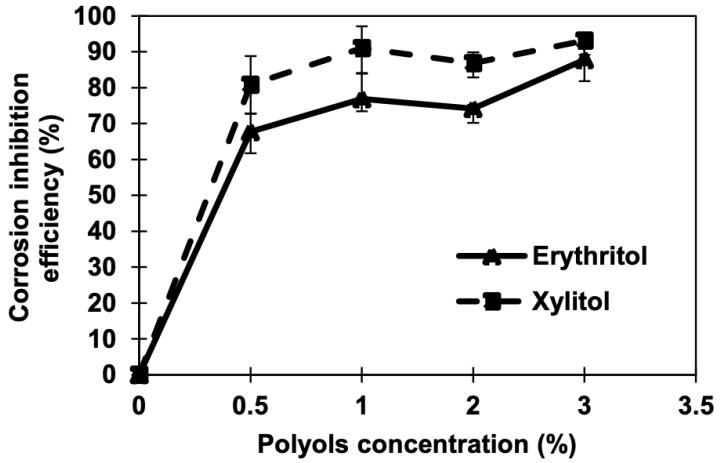

Figure 4-10: Improvement in corrosion inhibition efficiencies as a function of varying concentrations of erythritol and xylitol.

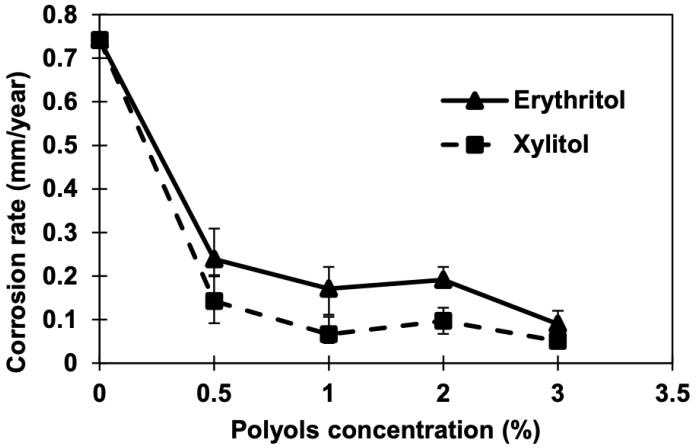

Figure 4-11: Decrease in corrosion rates in ASTM A572 steel specimens as a function of weight concentrations of erythritol and xylitol in salt brine deicer.

Table 4-2: Electrochemical parameters obtained from Tafel extrapolation.

	Corrosion inhibitors	Dosage (%)	E_corr (V)	$\lVert -i \rVert\_corr$ (μA/cm^2)	$\lVert -\beta \rVert\_c$ (V/dec)	Corrosion rate (mm/yr)
1	Benchmark	-	-1.001	63.169	0.135	0.742
2	Erythritol	0.5	-0.991	20.378	0.105	0.239
		1	-0.972	14.591	0.095	0.171
		2	-0.984	16.292	0.095	0.191
		3	-0.962	7.721	0.085	0.090

3 Xylitol	0.5	-0.969	12.135	0.109	0.142
	1	-0.942	5.652	0.102	0.066
	2	-0.923	8.324	0.096	0.097
	3	-0.856	4.356	0.082	0.051

4.4.4 Corrosion Phenomenon and Inhibition Mechanism

Corrosion Process

The corrosion phenomenon, as a consequence of a redox reaction wherein two complimentary reactions occur [118], involves the dissolution of iron at the anodic site results in deterioration and physical loss of the metal which is governed by Eq. 3 (see Table 4-3). The pH level of the solution influences the reaction at the cathodic site. In an acidic environment, the reduction of hydrogen ions (H^+) take place, whereas, in basic or at neutral pH conditions, reduction of dissolved oxygen occurs as depicted by Eq. 4, and Eq. 5 (see Table 4-3). The hydroxyl ions (OH^-) generated from the reduction of dissolved oxygen at the cathodic site migrates to the anodic site, reacting with the iron ions Fe^{2+} to form ferrous hydroxide $Fe(OH)_2$, which is regarded as the initial corrosion product [60], [119]. Furthermore, in brine solutions, the concentration of dissolved oxygen is significantly low due to the prevalence of sodium (Na^+) and chloride (Cl^-) ions, diminishing the prominence of dissolved oxygen reduction compared to the hydrogen liberation. To maintain the chemical equilibrium, hydrogen evolution (see Eq. 6) also occurs by the direct reduction of water molecules as indicated in the literature [80], [120].

The presence of sodium (Na^+) and chloride (Cl^-) ions in the benchmark deicing media (23% wt. $NaCl$) without polyols augments the electrolytic conductivity of the solution, thereby accelerating the rates of both cathodic and anodic reactions. Additionally, these ions foster the formation of $FeCl_2$, alongside $Fe(OH)_2$, and sodium hydroxide ($NaOH$). The formation of $FeCl_2$ initiate the hydrolysis of water, resulting in the formation of hydrochloric acid (HCl) (see Eq. 7), thereby amplifying the solution's acidity and corrosiveness [121]. The addition of polyols into the deicing solution inhibits the corrosion of metal, which is discussed in the following section.

Table 4-3: Chemical reactions involved in the corrosion process.

Reaction description	Equation	No.
Anodic dissolution of iron	$Fe \rightarrow Fe^{2+} + 2e^-$	Eq. 3
Cathodic reduction (Acidic environment)	$2H^+ + 2e^- \rightarrow H_2$	Eq. 4
Cathodic reduction (Neutral or basic environment)	$H_2 + 2H_2O + 4e^- \rightarrow 4OH^-$	Eq. 5
Reduction of water	$2H_2O + 2e^- \rightarrow H_2 + 2OH^-$	Eq. 6
Formation of HCl	$FeCl_2 + 2H_2O \rightarrow FeO + 2HCl$	Eq. 7

Role of Erythritol and Xylitol in Corrosion Inhibition

When the polyols (erythritol or xylitol) are added to the deicing solution, they engage in a competition with the OH^- and O_2 atoms to adhere to the iron ions by physical, chemical, or both adsorption. In previous studies, polyols of a similar class, namely, sorbitol, mannitol, and maltitol, were investigated, confirming their chelating affinity for metals [29], [84]. In an alkaline or neutral environment, polyols can furnish anionic sites where multivalent iron/metal ions can bind. Multivalent iron ions refer to ferrous (Fe^{2+}) and ferric ions (Fe^{3+}), which can bind to the polyols molecules by losing two or three electrons, respectively [29], [84]. These characteristics facilitate the formation of stable complexes on the iron surface, impeding the active sites for electrochemical reactions.

Pertaining to the potentiodynamic polarization curves, the corrosion protection performance of polyols has been thoroughly discussed in Sections 3.2 and 3.3. In addition to the reduction in corrosion rates and movement of polarization curves toward the more noble region, displacement in corrosion potential is discussed herein. The average displacement in corrosion potential of erythritol is 0.024V, whereas for xylitol is 0.078V. With this, it is established that the average shift in corrosion potential for both erythritol and xylitol falls below the threshold of 0.085V. This threshold is typically followed in literature to classify corrosion inhibitors as anodic or cathodic [122], [123]. These observations conclude that the erythritol and xylitol act as mixed-type corrosion inhibitors. Overall, the shifting of corrosion potential towards the more positive side shows the dominance of anodic inhibition, which is more prominent in the case of xylitol. Mixed types of corrosion inhibitors adhere to the steel surface via physisorption or chemisorption to protect the surface by blocking the active sites, which will be discussed in the next section [105].

4.4.5 Adsorption Isotherms of Erythritol and Xylitol

The adherence of the polyols (erythritol and xylitol) to the steel surface is further quantified using the adsorption isotherms. Adsorption isotherm is the graphical interpretation between the corrosion inhibitor molecules and their adsorb concentration on the metal surface [111]. The concentration of the corrosion inhibitor molecules is usually determined experimentally [123]. The interaction of the corrosion inhibitors and steel surface depends on several factors, such as the chemical structure of the corrosion inhibitor molecules, electrode potential, temperature of the electrolyte, and characteristics of the steel surface (composition, roughness, etc.) [99], [124]. Corn-based polyols., i.e., erythritol and xylitol, are organic in nature, and their adsorption onto the steel surface in an aqueous medium is considered a quasi-substitutional process [115], [125]. Quasi substitutional process refers to the reaction where a reactant molecule physically replaces a radical of the second reactant. Herein, the polyol (erythritol or xylitol) molecules substitute the associated water molecules that are adsorbed onto the steel surface [115], [126] as depicted by Eq. 8 (see Table 4-4). Herein, x is the number of water molecules that are substituted by the polyols. The water molecules adhered to the steel surface are replaced by the polyol molecules., i.e., erythritol or xylitol. Adsorption isotherms are developed for erythritol and xylitol adsorption using the Langmuir isotherm model [124]. The Langmuir isotherms, also known as straight-line models, are developed for various concentrations of polyols (erythritol and xylitol) employing Eq. 9 (see Table 4-4). $\mathrm{C_{Poly}}$ is the concentration of polyols employed in the study, θ is known as surface coverage representing a thin layer of adsorb polyols on the surface of the steel specimens and is determined using the CIE (%) data using Eq. 10 (see Table 4-4), while $\mathrm{K_{ads}}$ is the standard adsorption equilibrium constant. $\mathrm{K_{ads}}$ is determined from the Langmuir isotherm model and is then used to calculate the standard free energy (ΔG^0_{ads}) of adsorption which quantifies the interaction of adsorbed polyols with the steel surface, provided in Eq. 10 [123]. Eq. 11 relates the ΔG^0_{ads} to K_{ads} [126], [127]. R is the universal gas constant which is equal to 8.314Joule/K-mol, T is the absolute value of

temperature in kelvin (K) which is equal to 293.15K, and 55.5mol/L is a constant factor which represents the molar concentration of water.

Figure 4-12 displays the plots of the polyol concentration (C_{Poly}) to the ratio of polyols concentration and respective surface coverage (C_{Poly}/θ). It is noticed that the plots yield straight lines, which confirms that the adsorption of erythritol and xylitol on the ASTM A572 steel surface in traditional deicing media obeys the Langmuir adsorption isotherm [124]. The adsorption parameters obtained from the Langmuir adsorption isotherms are tabulated in Table 4-5. For both the types of polyols investigated in this study, the ΔG^0_{ads} values are observed to be negative which suggest that the adsorption process of polyols onto the surface of ASTM A572 steel is spontaneous, and does not necessitate an external source of energy. Studies in the past reported that investigating the ΔG^0_{ads} offer a valuable insight into the type of adsorption between the corrosion inhibitor and the metal surface [128], [129]. The adsorption of corrosion inhibitors is considered physical if the value of ΔG^0_{ads} are less than -20kJ/mol [127]. Physical adsorption means that the inhibitors will adhere to the metal surface via electrostatic attraction also known as physisorption. Similarly, the adsorption will be considered as chemical if the ΔG^0_{ads} values are greater than -40kJ/mol [126]. This means that the inhibitors will attach it to the steel surface through the sharing or transfer of electrons, which will establish a coordinate type of bond, also known as chemisorption. Studies performed in the recent past showed ΔG^0_{ads} values in a range of -28kJ/mol, which is associated with mixed types of adsorption [127], [130], [131]. In this study, the values of ΔG^0_{ads} are less than -20kJ/mol (see Table 4-5) which shows that both the erythritol (-15.10kJ/mol) and xylitol (-17.68 kJ/mol) are adsorbed onto the ASTM A572 steel surface via physisorption. Moreover, the ΔG^0_{ads} for xylitol is comparatively closer to the threshold value (-20kJ/mol) than the erythritol which show the stronger adsorptive and film-forming ability of xylitol. Furthermore, this observation is also in line with the results from accelerated corrosion studies.

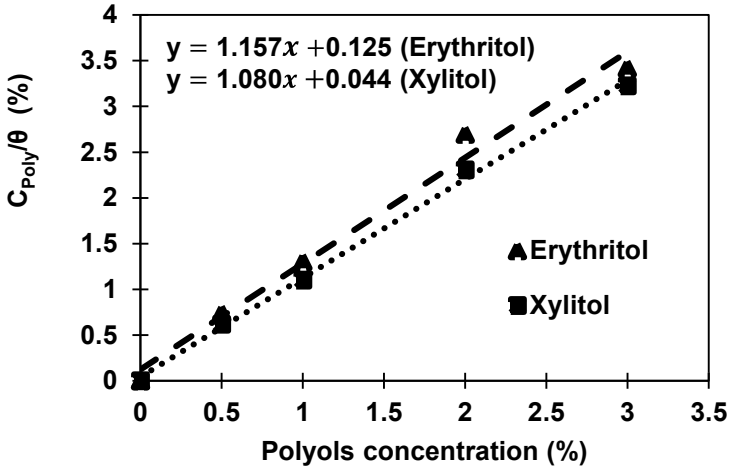

Figure 4-12: Evaluation of langmuir adsorption isotherm for steel specimens in traditional deicing media (23% wt. of $NaCl$) containing various concentrations of erythritol and xylitol.

Table 4-4: Equations used to determine various adsorption parameters for erythritol and xylitol in a chloride environment.

Reaction description	Equation	No.
Substitution reaction of polyols in water	$Polyol_{(sol)} \cdot + xH_2O_{(ads)} \rightarrow Polyol_{(ads)} \cdot + xH_2O_{(sol)}$	Eq. 8

Langmuir adsorption model	$\frac{C_{Poly}}{\theta} = \frac{1}{K_{ads}} + C_{Poly}$	Eq. 9
Surface coverage	$\theta = \frac{CIE\,(\%)}{100}$	Eq. 10
Standard free energy of adsorption	$\Delta G^0_{ads} = -RTln(55.5K_{ads})$	Eq. 11

Table 4-5: Electrochemical parameters from the Langmuir isotherm model.

	Polyol type	$1/K_{ads}$	$\Delta G^0_{ads}(k.Jol/mol)$	***Refs***
1	Erythritol	0.125	-15.10	This study
2	Xylitol	0.044	-17.68	This study
3	Sorbitol	0.092	-23.04	[54]
4	Mannitol	0.079	-23.43	[54]
5	Maltitol	0.054	-25.95	[54]

4.4.6 Adsorption Isotherms of Erythritol and Xylitol

The surface of the steel specimens subjected to a recurring flow of traditional deicing media (23% brine solution) for 48 hours incurred variable degrees of corrosion damage. As already discussed in Section 3.1, the steel specimens subjected to various concentrations (0.5%, 1%, 2%, and 3%) of erythritol and xylitol revealed less corrosion damage than the benchmark deicing solution (see Figure 4-3 to Figure 4-6). Therefore, we investigated the surface of the steel specimens using three different characterization techniques to determine the types of corrosion products and surface morphology of these specimens. All three characterizations are performed on the benchmark specimen (exposed to traditional deicing media containing no polyols) and the specimen exposed to deicing media containing 3% of each polyol. SEM micrographs and EDX analysis are conducted on the surface of the representative specimens using a JEOL JSM-6490LV scanning electron microscope. All the SEM images are taken at 2000X magnifications (see Figure 4-13). The ASTM A572 steel specimen exposed to traditional deicing media containing no polyol exhibits a relatively rough surface morphology (see Figure 4-13 – (a)). The whole surface was predominantly covered with goethite ($\alpha - \mathrm{FeOOH}$) and lepidocrocite ($\gamma - \mathrm{FeOOH}$) in the form of semi crystalline species [132]. The rough surface also contains some form of amorphous ferrous hydroxides [130]. Moreover, the presence of sodium chloride crystals on the surface of the steel specimens was also confirmed during the SEM analysis. On the contrary, the steel specimens subjected to the deicing solution containing polyols (3% of erythritol or 3% of xylitol) display a thick oxide layer, some spherical-shaped goethite crystals ($\alpha - \mathrm{FeOOH}$) and occasional salts crystal deposits (see Figure 4-13 – (b & c)). Notably, the SEM micrographs reveal less corroded surface morphology regardless of the type of polyols employed in the deicing media. The prominent difference in surface roughness and reduced corrosion product formation indicate that polyols effectively act as corrosion inhibitors which slow down the corrosion process. The observed corrosion products were then characterized through EDX analyses and the elemental composition is presented in Figure 4-14, Figure 4-15, and Figure 4-16. EDX analyses were performed at two different spots on the same specimen's

surface. It is noticed that all three representative specimens revealed four main elements in their EDX spectra: iron (Fe), oxygen (O), sodium (Na), and chlorine (Cl). The intensified peaks of Fe and O confirm the formation of corrosion products, while the mild peaks from Na and Cl indicate the residual salts from deicing media.

The composition of the corrosion products on the surface of the steel specimens is further validated by performing XRD analyses. Herein, the XRD patterns were directly obtained from the surface of representative specimens (benchmark specimens and specimens subjected to 3% of erythritol or xylitol). The analysis was performed using a multipurpose X-ray diffractometer named Bruker AXS' D8 Discover, following the procedure described in Section 2.2.3. The diffractograms are presented in Figure 4-17, Figure 4-18, and Figure 4-19. All the XRD patterns exhibit three characteristic peaks which are commonly observed in low-carbon steels, along with peaks corresponding to NaCl from the deicing solution [104]. These patterns signify the presence of NaCl, $FeOOH$, Fe_2O_3, and metallic iron in the corrosion products [59]. Both $FeOOH$, Fe_2O_3, are the oxides of iron resulting from the loss of two and three electrons, respectively. Structurally, $FeOOH$ serves as an outer layer, while Fe_2O_3 forms an inside layer. $FeOOH$ is vivid or dark orange in color, formed at the initial stage of corrosion, acting as a protective passivation layer against further corrosion. In contrast, Fe_2O_3 displays a reddish-brown color and forms a more stable oxide layer on the metal surface, serving as a site for the accumulation of corrosion products [133], [134]. However, both of these layers are porous and can allow oxygen, and water, alongside the chloride ions from the deicing solution, to further deteriorate the metals [134]. The presence of these products also validates the findings of SEM and EDX analyses, which suggest the formation of different corrosion products on the surface of steel specimens. Notably, a higher count is observed for $FeOOH$ in case of the specimen exposed to traditional deicing media containing no polyols. In addition to this, the disappearance of the peak corresponding to Fe_2O_3 in the case of the deicing solution containing polyols confirms that polyols effectively slow down the corrosion rate and consequently limit the formation of corrosion products.

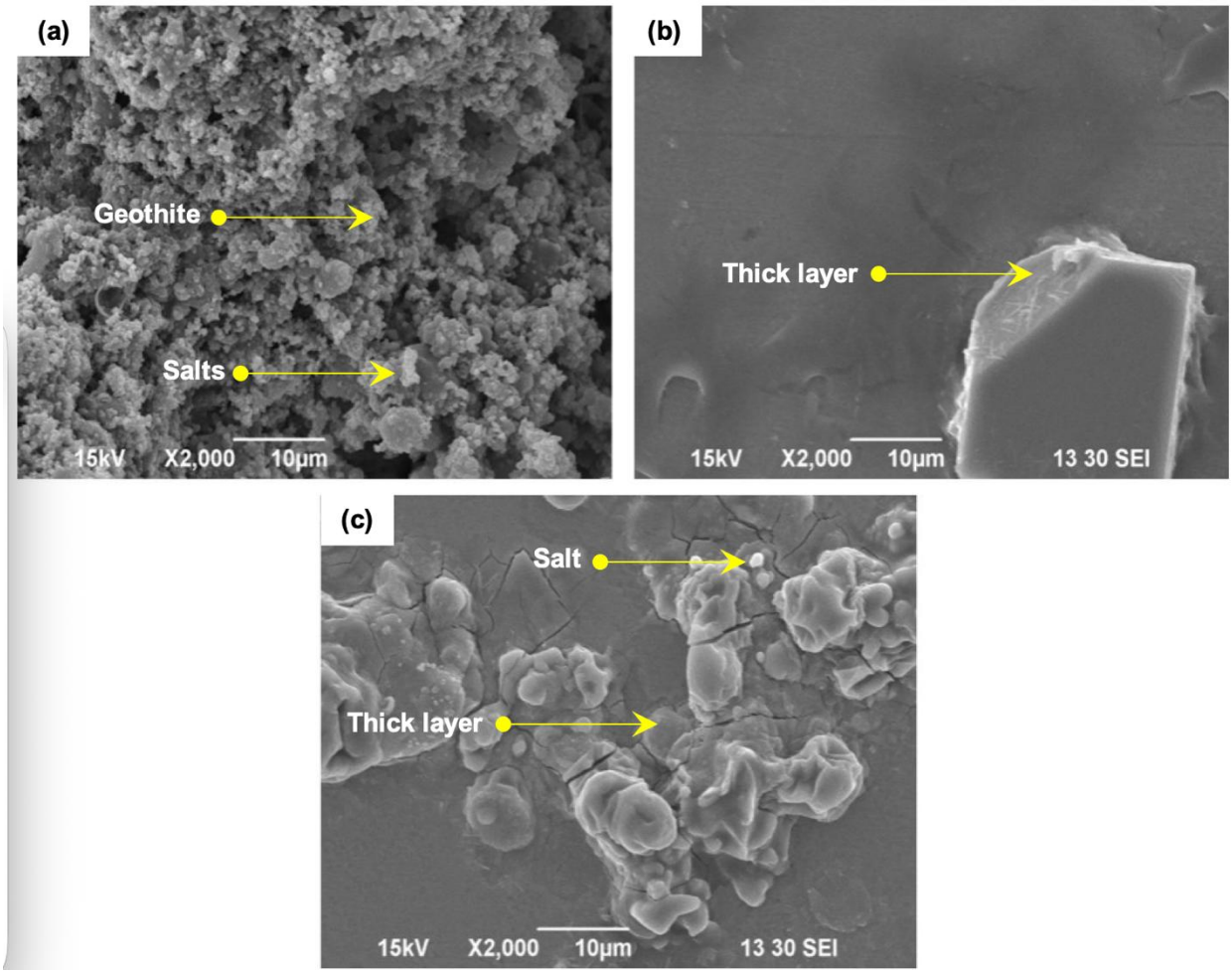

Figure 4-13: Evaluation of langmuir adsorption isotherm for steel specimens in traditional deicing media (23% wt. of $NaCl$) containing various concentrations of erythritol and xylitol.

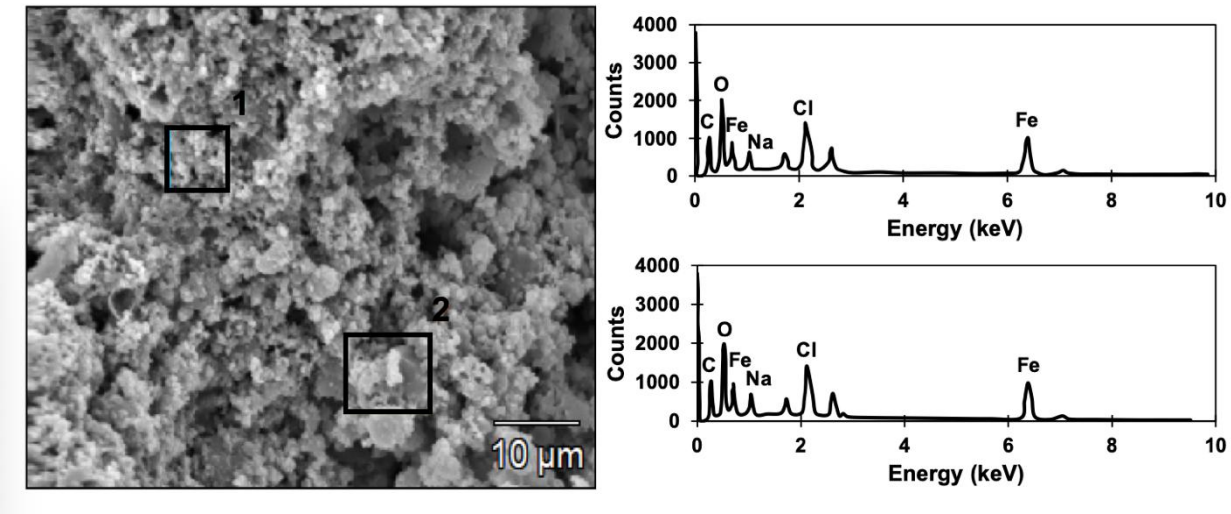

Figure 4-14: EDX spectra illustrating the elemental composition of corroded ASTM A572 steel specimen's surface subjected to the recurring flow of traditional deicing media containing no polyols.

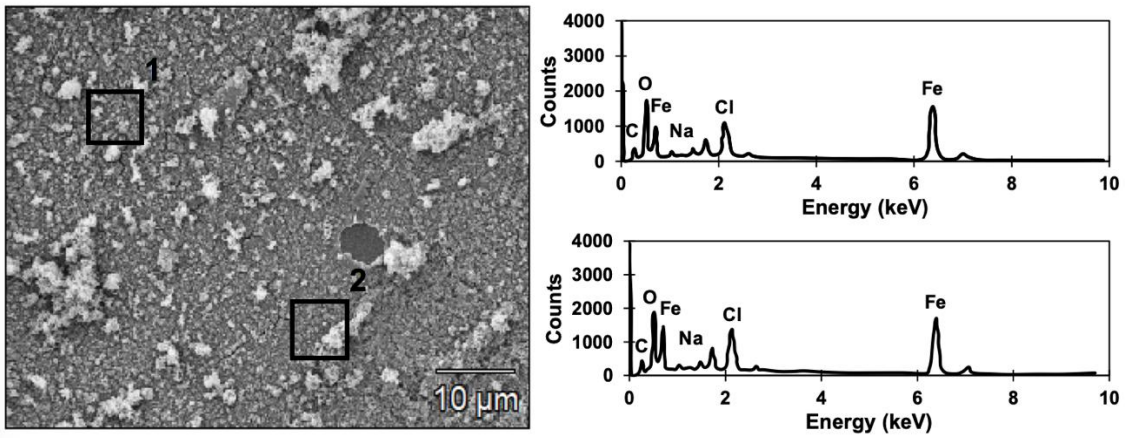

Figure 4-15: EDX spectra illustrating the elemental composition of the corroded steel specimens subjected to the recurring flow of traditional deicing media containing erythritol.

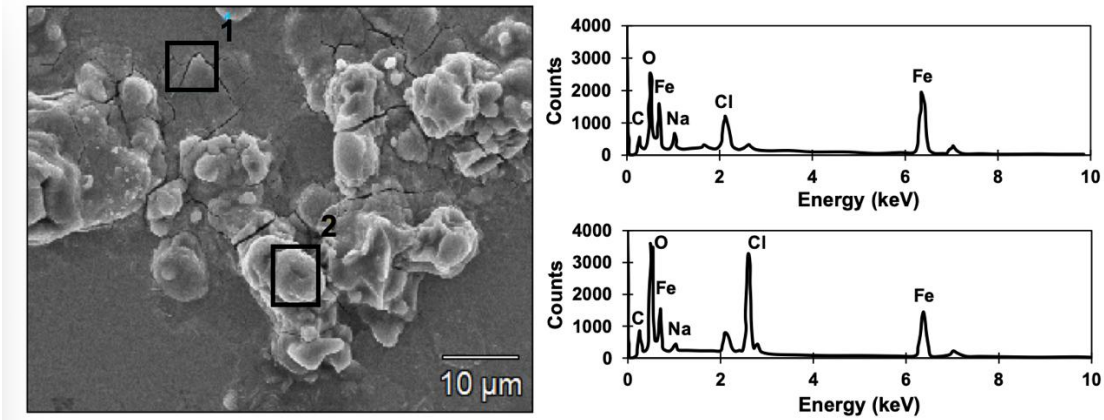

Figure 4-16: EDX spectra illustrating the elemental composition of the corroded steel specimens subjected to the recurring flow of traditional deicing media containing xylitol.

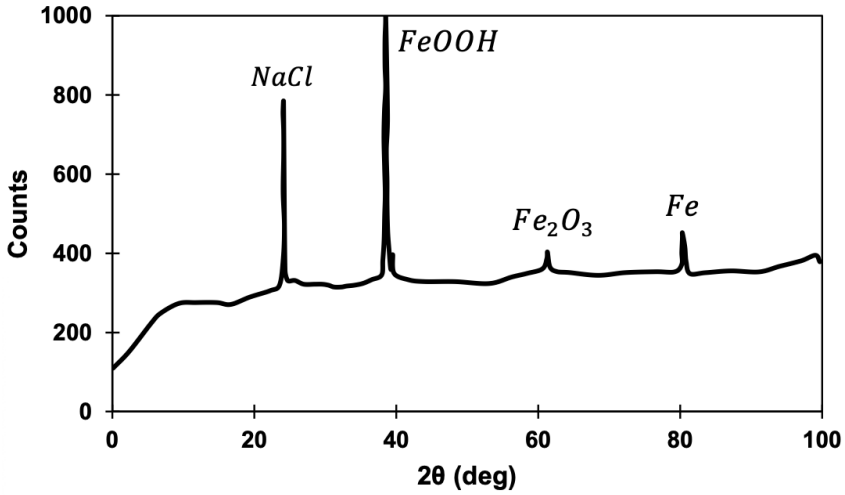

Figure 4-17: XRD diffractogram showing the patterns of various phases present on the surface of corroded steel specimen subjected to the recurring flow of traditional deicing media containing no polyols.

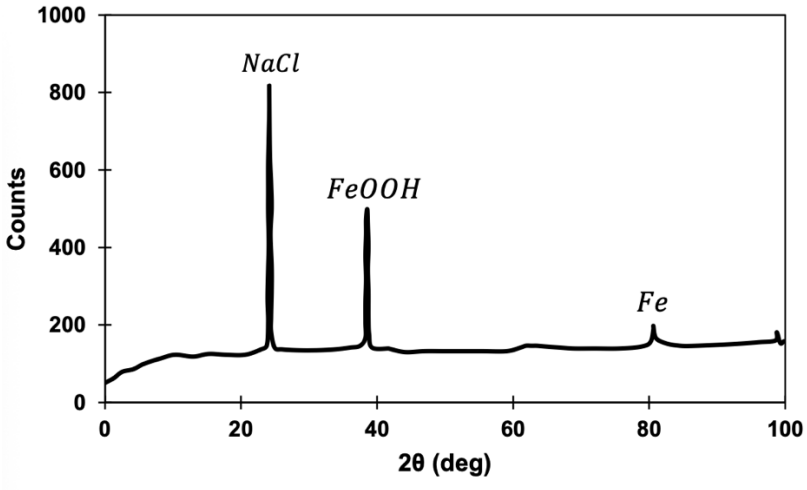

Figure 4-18: XRD diffractogram showing the patterns of various phases present on the surface of corroded steel specimen subjected to the recurring flow of traditional deicing media containing 3% of erythritol.

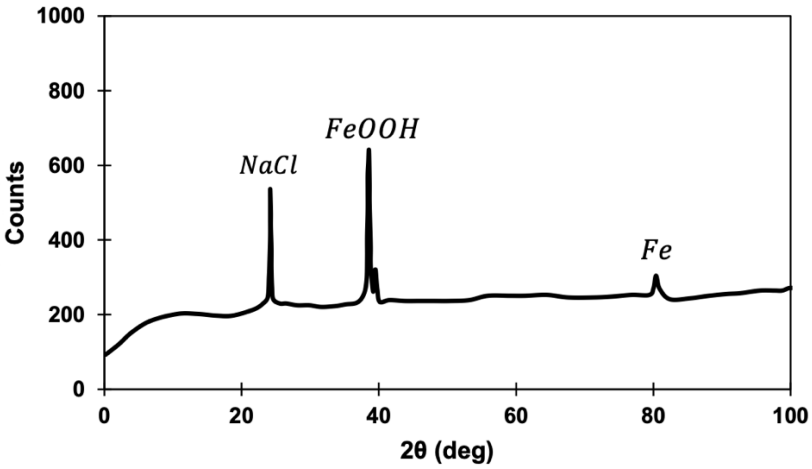

Figure 4-19: XRD diffractogram showing the patterns of various phases present on the surface of corroded steel specimen subjected to the recurring flow of traditional deicing media containing no polyol 3% of xylitol.

5 Correlation Between Dry and Swollen Superabsorbent Polymer Particle Sizes in Cement Pore Solution and Salt Brine

5.1 Introduction

Superabsorbent polymers (SAPs) have hydrophilic, three-dimensionally crosslinked polymer networks that can absorb and retain substantial amounts of water or aqueous fluids relative to their own mass [135]. SAPs are engineered to absorb between 200 and 4000 grams of fluid per gram of polymer without dissolving, due to their distinct network structure and crosslink density [136]. These materials were first conceptualized in the 1930s and were first commercialized in the 1960s for ophthalmic applications and subsequently in various other applications [4]. SAPs were initially utilized for hygiene products and have since been widely used in biomedical applications in drug delivery, wound dressings, and tissue engineering, where their ability to swell and hold moisture helps release medicines gradually and promote healing [1], [22], [26]. The primary distinguishing features of SAPs include their high swelling capacity, mechanical deformability in the dry state, and fragility when swollen, all resulting from water-polymer interactions and osmotic pressure gradients [20], [23], [137]. The swelling mechanism of SAPs is governed by the balance between osmotic pressure driving water uptake and the repulsion between ionized carboxylate groups within the polymer network. Upon contact with water, the higher chemical potential outside the polymer matrix, which acts as the driving force for mass transfer, causes water to diffuse into the polymer matrix. The chemical potential is essentially defined as the measure of the free energy per unit amount of a substance that drives its tendency to move, react, or equilibrate between phases or regions, such as between a polymer gel and its surrounding solution**.** Deswelling occurs with changes in temperature, chemical equilibrium, humidity, or mechanical pressure. Factors such as crosslinking density, ionic strength, and the properties of the absorbed fluid affect this process [138], [139].

Recently, SAPs have been increasingly integrated into cementitious systems in civil engineering and construction materials. They help mitigate autogenous shrinkage, control early age cracking, and enhance internal curing efficiency. Their absorption and desorption behaviors influence hydration kinetics, microstructure development, and mechanical performance, making them essential additives for high-performance concrete applications [46], [138], [140]. Acting as internal water reservoirs, SAPs gradually release water as the surrounding matrix dries, which aids in maintaining hydration continuity and improving the durability of high-performance concrete. In addition, SAPs have also proven to be useful for preserving the concentration of brine solution used for deicing of roads, resulting in enhanced ice melting capacity with minimal impact on skid resistance [141]–[143].

However, despite the widely recognized advantageous inclusion of SAPs in various systems, they tend to exhibit unique size-dependent absorption and desorption characteristics that govern their functionality in cementitious, brine, and aqueous environments [144], [145]. Recent studies have demonstrated that smaller SAPs enable faster hydration in cementitious environments due to more rapid water release, whereas larger particles can influence a wider hydration zone while increasing total porosity. Furthermore, smaller SAP particles exhibit faster absorption rates due to reduced diffusion paths, meaning that water can penetrate the polymer more quickly because of the shorter diffusion distance within the particle structure [26], [146]. The effect of the different morphology of SAPs, spherical versus irregular granules, has been investigated in previous studies and found to have some impact on the swelling behavior of SAPs. Despite all these observations, the size-dependent effect on

the swelling behavior of SAPs still requires further investigation. This gap is particularly relevant in cementitious environments, due to the increasing use of SAPs as internal curing agents [147].

Based on the literature, SAP particles have different sizes, ranging from around 50 µm to 850 µm. There is a notable lack of understanding regarding how size influences the swelling behavior of SAPs. Current assessment methods primarily examine the bulk behavior of these materials [148]. A clear understanding of the impact of size on the swelling mechanism is particularly relevant for evaluating the pore structure of concrete or measuring the retention capacity of particles when used alongside deicers as additives [149].

Different bulk gravimetric methods have been used to quantify the swelling mechanism of SAPs. Many commonly used pre-screening techniques, such as the RILEM-recommended tea-bag and filtration methods, offer approximate estimates and are primarily intended for comparative assessments rather than precise representation of in situ behaviour. Zhao et al. and Olawuyi & Boshoff stated that the interstitial water retention, which refers to the water molecules trapped in the tiny spaces between SAP particles, within the tea bag, often leads to overestimated absorption values [148], [150], [151]. Manual blotting also introduces operator bias, while pouch confinement restricts the swelling of highly absorptive SAPs. Similarly, the filtration method, although more direct, typically disrupts swollen SAP particles under vacuum pressure, potentially underestimating absorption due to particle loss through filter pores.

Advanced imaging methods offer more accurate, spatially resolved insights into SAP behavior. Optical microscopy and laser diffraction techniques have been employed to track swelling behavior and particle size evolution, providing direct visual confirmation of particle swelling, albeit limited to two-dimensional imaging and less effective for embedded SAPs. X-ray micro-computed tomography (µCT), utilized by Olawuyi & Boshoff [149], offers non-destructive 3D analysis of internal void formation caused by SAP swelling, revealing void size, distribution, and morphology. The TC 260-RSC recommends standardized SAP characterization techniques, including laser diffraction, SEM/ESEM, µCT, and optical microscopy, depending on the desired resolution and transparency of matrices [152].

The objective of this study is to quantify the correlation between the dry and swollen SAP particle volumes in cementitious, brine, and aqueous solutions. An advanced digital microscope with 3D imaging capability was used, as gravimetric analysis has limitations in analyzing individual particles. The swollen SAP particle sizes were assessed at 5, 10, 30, and 60 minutes. The resulting 3D images were investigated to characterize water absorption and its rate.

5.2 Materials and Methods

5.2.1 Super Absorbent Polymer and Test Solution Preparation

Liquiblock WHS2 is a commercially available SAP that was procured from Chase Corporation, named as SB in this study. It is a sodium salt of crosslinked polyacrylic acid containing hydrophilic carboxylate groups, which exhibit strong affinity towards water due to their negative charges and polar nature [148]. SB was selected for this study because of its widespread use in internal and external curing applications within cementitious systems, where its high water retention and controlled release capacity enhance hydration and reduce shrinkage [145], [153]. Additionally, SB has shown promise in deicing applications by improving the longevity and efficiency of brine-based systems, owing to its ionic compatibility and swelling behavior in saline environments [145]. The properties of SB, including chemical composition, particle size distribution (PSD) in µm, pH value, apparent bulk density in

grams/liter (g/l), moisture content in %, and deionized water absorption capacity in grams/gram (g/g) are provided by the manufacturer and summarized in Table 5-1.

The swelling capacity of SB highly depends on its responsiveness to external stimuli such as pH and ionic concentration [26], [154], [155]. To evaluate these effects, SB was tested in three distinct media: cement pore solution, 3.5% NaCl solution, and distilled water. The cement pore solution was prepared following the procedure outlined in RILEM recommendations by mixing cement and water at a water-to-cement ratio of 5:1 by weight, magnetically stirring the mixture for 24 hours, and subsequently filtering to obtain a clear solution. The pH of the resultant pore solution was 12.7, which was measured by an OAKLAN PH550 pH meter. The 3.5% NaCl solution was selected to simulate SAP deicer blends applied on icy roads.

Table 5-1: Material properties of SAP.

SAP ID	Commercial Name	Chemical composition	Particle Size Distribution (µm)	pH	Apparent Bulk Density (g/l)	Moisture Content (%)	Chemical structure
SB	Liquiblock™ WHS2	Sodium salt of crosslinked polyacrylic acid	150-850	5.6-6.6	600-700	0-5	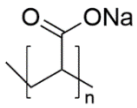

5.2.2 SAP Particle Volume Measurement

A total of 180 SB particles, covering a range of dry volumes from 0.03 mm^3 to 0.35 mm^3, were evaluated across the three previously described media, with 60 particles allocated to each medium. SB particles were initially separated by dry sieving using ASTM standard sieves with mesh sizes of No. 50 (300 µm), No. 40 (425 µm), No. 35(500 µm), No. 30 (600 µm), and No. 25 (710 µm). Subsequently, particles within each sieved size range were inspected via optical microscopy to confirm consistency in dry volume distribution.

The swelling behavior of SB particles was analyzed using a Keyence VHX-7000 digital microscope equipped with a 4K CMOS image sensor and high-resolution lenses capable of magnifications ranging from 20× to 6000×. Each SAP particle was submerged individually into the selected solutions, and their 3D profiles were captured at specified intervals of 0-, 5-, 10-, 30-, and 60- minutes. To ensure accurate volumetric assessment of irregularly shaped particles, images were taken at three different tilt angles. The final particle volume was determined as the average of these three measurements. The microscope's built-in Depth from Defocus (D.F.D.) algorithm was employed to calculate the vertical positioning of each pixel through lens movement. This algorithm generates a brightness versus z-height curve, identifying the pixel height at maximum brightness and thereby enabling detailed and accurate 3D characterization of both dry and swollen SAP particles. To better visualize this process, Figure 5-1 illustrates how the volumetric measurements were derived. In Figure 5-1. (a), a 3D cross-sectional view of an SB particle is shown, where a slicing plane intersects the particle to reveal its internal contour. Figure 5-1. (b) presents the top view of the same particle, along with a corresponding height profile (green

line) across the selected cross-section. The maximum vertical height (e.g., H_{max} = 477 µm) is marked as an example of the depth data captured. Using this approach, the height at each point on the particle's surface is measured across successive cross-sections, and the total volume is calculated by integrating these heights over the corresponding surface areas. This method enables precise volume estimation of highly irregular SAP particles.

The absorption rate of each particle (R_V) was calculated using the following equation

$$R_V = \frac{(V_s - V_d) \times \rho_W}{t} \quad (3)$$

where V_d is the dry volume, V_s is the swollen volume, ρ_W is the density of water (approximately 1000 g/L), and t is the swelling time in minutes.

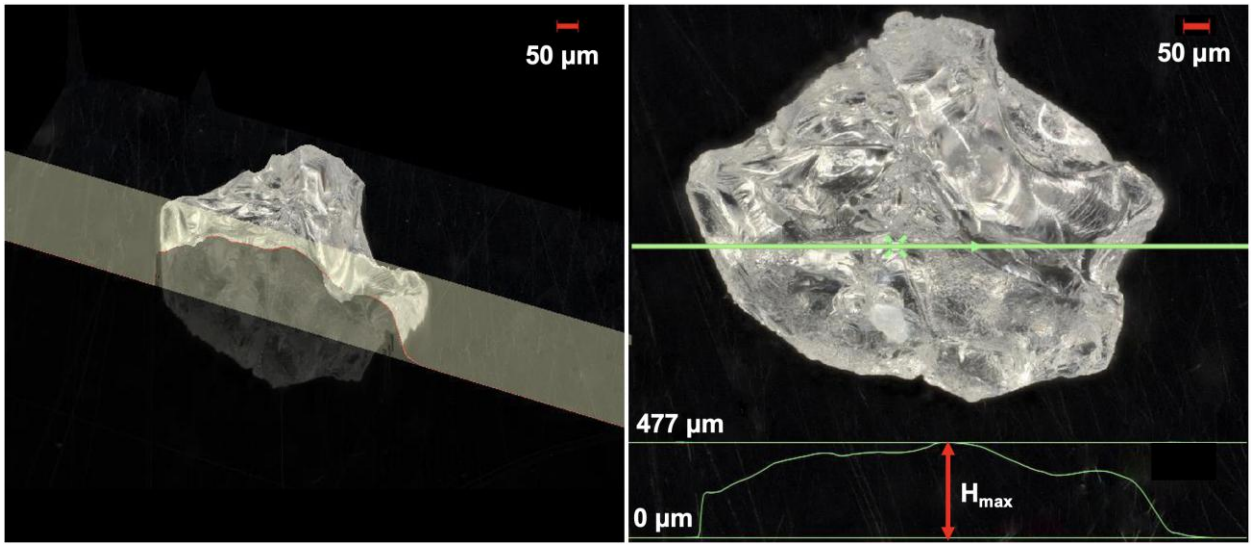

Figure 5-1: 3D digital microscopy images of an SB particle used for volumetric analysis: (a) cross-sectional view showing the internal structure along a slicing plane (light band), and (b) top view of the same particle with a height profile line (see the lower half of image) used to measure vertical heights across the selected cross-section. Experimental Program

5.2.3 Correlation analysis

The purpose of this study is to evaluate the correlation between the dry and swollen volumes of the SAP particles. To this end, Pearson correlation coefficient, Spearman rank correlation coefficient, and distance correlation coefficient were used. The correlation coefficients were computed between the dry SAP volume and swollen SAP volumes evaluated at four different time intervals: 5 mins, 10 mins, 30 mins, and 60 mins, after soaking the SAP particles in distilled water, 3.5% wt. NaCl solution and cement pore solution. The Pearson correlation coefficient quantifies the linear correlation between the dry and swollen volumes. The value of the Pearson correlation coefficient varies between -1 and +1, where positive and negative coefficients indicate direct and inverse linear relationships between the dry and

swollen volumes, and a value of 0 indicates no linear correlation. The Pearson correlation coefficient (r_p) is given as:

$$r_p = \frac{\sum(x_i - \bar{x})(y_i - \bar{y})}{\sqrt{\sum(x_i - \bar{x})^2 \sum(y_i - \bar{y})^2}} \quad (4)$$

where, x_i and y_i are the i^{th} values of the dry and swollen volumes of the SAP particle, $\bar{x}$ and $\bar{y}$ are the mean values of the dry and swollen volumes of the SAP particle.

The Spearman's correlation coefficient was also evaluated for the dry and swollen volumes of the SAP particles to assess the monotonic relationship between the variables. Unlike Pearson's correlation coefficient, the Spearman correlation coefficient is evaluated using the ranks of the data rather than the raw values. The correlation coefficient varies between -1 and +1, where a value close to ±1 indicates a strong monotonic relationship, and a value close to 0 indicates a very weak relationship. The sets of values of the two variables are assigned ranks, and the correlation coefficient is quantified based on the rank differences between the observations of the two variables. The Spearman's correlation coefficient (r_s) is given as:

$$r_s = 1 - \frac{6\sum d_i^2}{n(n^2 - 1)} \quad (5)$$

where, d_i is the difference between the two ranks and n is the total number of observations.

Furthermore, the distance correlation between the two variables was also quantified. The distance correlation measures the dependence between two variables irrespective of the nature of the relationship, making it possible to capture any nonlinear correlation between the variables. Let us assume two random vectors X ∈ R^n and Y ∈ R^n, representing n paired observations, denoted by sample vectors x= (x_1,x_2,…..,x_n)^T and y= (y_1,y_2,…..,y_n)^T. The pairwise distance matrices A=[a_ij]∈ R^(n×n) and B=[b_ij]∈ R^(n×n) are computed using a_ij=‖x_i-x_j ‖_p and b_ij=‖y_i-y_j ‖_q, where ‖·‖_p and ‖·‖_q denote the l_p and l_q norms, respectively, and i and j represent the i^th and j^th observations. Subsequently, the distance matrices A and B are double-centered to obtain $\bar{A}$= [$\bar{A}$_ij]∈ R^(n×n) and $\bar{B}$=[$\bar{B}$_ij]∈ R^(n×n) where,

$$\bar{A}_{ij} = a_{ij} - \frac{1}{n}\sum_{l=1}^{n} a_{il} - \frac{1}{n}\sum_{k=1}^{n} a_{kj} + \frac{1}{n^2}\sum_{k,l=1}^{n} a_{kl}$$

$$\bar{B}_{ij} = b_{ij} - \frac{1}{n}\sum_{l=1}^{n} b_{il} - \frac{1}{n}\sum_{k=1}^{n} b_{kj} + \frac{1}{n^2}\sum_{k,l=1}^{n} b_{kl} \quad (6)$$

The squared sample distance covariance is then given as:

$$\mathrm{dCov}^2(\boldsymbol{x}, \boldsymbol{y}) = \frac{1}{n^2}\sum_{i,j=1}^{n} \bar{A}_{ij}\bar{B}_{ij} \quad (7)$$

Finally, the sample distance correlation ($\mathcal{R}$) is given as:

$$\mathcal{R} = \mathrm{dCor}^2(\boldsymbol{x},\boldsymbol{y}) = \begin{cases} \dfrac{\mathrm{dCov}^2(\boldsymbol{x},\boldsymbol{y})}{\sqrt{\mathrm{dCov}^2(\boldsymbol{x},\boldsymbol{x})\mathrm{dCov}^2(\boldsymbol{y},\boldsymbol{y})}} & \text{if } \mathrm{dCov}^2(\boldsymbol{x},\boldsymbol{x})\mathrm{dCov}^2(\boldsymbol{y},\boldsymbol{y}) > 0 \\ 0 & \text{if } \mathrm{dCov}^2(\boldsymbol{x},\boldsymbol{x})\mathrm{dCov}^2(\boldsymbol{y},\boldsymbol{y}) = 0 \end{cases} \quad (8)$$

5.2.4 Inductively Coupled Plasma Optical Emission Spectroscopy (ICP-OES) test

To evaluate the effect of SB on cement pore solution chemistry, two liquid samples were prepared and analyzed using ICP-OES: (1) a control cement pore solution and (2) cement pore solution exposed to SB. In both cases, 100 mL of cement pore solution was prepared, and 0.2 grams of SB was immersed in the solution using a sealed teabag for 1 hour at room temperature to simulate ion exchange conditions. After exposure, the teabag was removed, and the solution was filtered as needed prior to analysis. ICP-OES measurements were conducted using an Agilent 5900 instrument in Synchronous Vertical Dual View (SVDV) mode with polychromator boost. Calibration was performed using the M26P standard, a commercial multi-element solution (VHG-SM75B) doped with phosphorus, covering 26 trace metals.

5.2.5 Elemental Composition Analysis

Laser-Induced Breakdown Spectroscopy (LIBS) was employed to evaluate the elemental composition of SB particles after exposure to cement pore solution. The SB particles were first soaked in cement pore solution for 60 minutes, then filtered, rinsed, and dried prior to analysis. For comparison, a separate set of SB particles that had not been exposed to any media was also tested under identical conditions. LIBS was performed in drilling mode to carry out depth profiling, allowing for the detection of elemental distribution from the surface inward. A high-energy pulsed laser was directed at a fixed point on each particle, progressively removing micro-layers of material and generating plasma emissions at each depth. The emitted spectrum was analyzed to identify the presence of elements. Five layers were profiled per test, each corresponding to a depth of 10 μm, enabling evaluation of changes in elemental composition throughout the particle cross-section.

5.3 Results and Discussion

SB is a homopolymer composed of acrylic acid monomers that have been crosslinked and subsequently neutralized using sodium hydroxide. This process forms an anionic structure with hydrophilic carboxylate functional groups distributed along its polymer chains. Upon exposure to an aqueous solution, SB undergoes swelling due to a difference in chemical potential between the polymer and the external solution. This difference in the chemical potential is due to the concentration gradient of ions between the particle's internal structure and the surrounding aqueous medium that causes osmotic pressure [144], [145]. To facilitate a clearer understanding of the swelling behavior of SB particles, this section is divided into three subsections based on the type of swelling medium: distilled water, cement pore solution, and NaCl solution. The swelling behavior of SB in each medium is discussed in detail in the following subsections.

5.3.1 Swelling Behavior of SB in Distilled Water

The swelling response of SB in distilled water is characterized by rapid water uptake and substantial volume change due to strong osmotic pressure. When SB is exposed to water, it undergoes

an initial wetting stage, during which the surface of SB comes into contact with water molecules. Subsequently, water molecules penetrate the micropores of the SB, hydrating sodium cations and carboxylate groups within the polymer chains. As illustrated in Figure 5-2, the horizontal and vertical wavy lines can be visualized as polymer chains with carboxylate groups (COO^-) and disassociated sodium ions within the SAP particle (grey region) surrounded by water. The presence of higher sodium ions and COO^- in the SAP particle will lead to a higher ionic concentration, resulting in water entering the SAP particle [144]. In addition, the electrostatic repulsion between the negatively charged COO^- groups on the polymeric chains, depicted by red arrows in Figure 5-2**,** provide gaps between polymer chains, allowing the newly entered water molecules to be retained within the SAP particle. These combined osmotic pressure and electrostatic repulsion forces contribute to the pronounced swelling behavior of SB in distilled water.

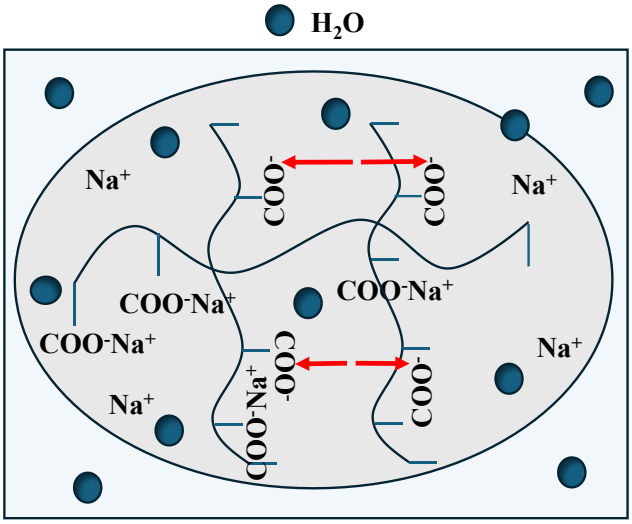

Figure 5-2: Schematic illustration of the swelling mechanism of SB in distilled water.

The swelling evolution of SB in distilled water is presented in Figure 5-3, showing the morphological changes of a representative particle at different times from 0 to 60 minutes. A rapid increase in particle size is observed within the first 10 minutes, followed by continued but slower swelling up to 30 minutes. Beyond this point, the particle exhibits minimal further swelling, suggesting that maximum swelling is attained by 30 minutes, referred to as equilibrium, consistent with observations previously reported in the literature [144], [145]. The equilibrium is obtained when either the osmotic pressure diminishes or the constraint imposed by the elastic restoring force of the SAP is achieved [135], [156].

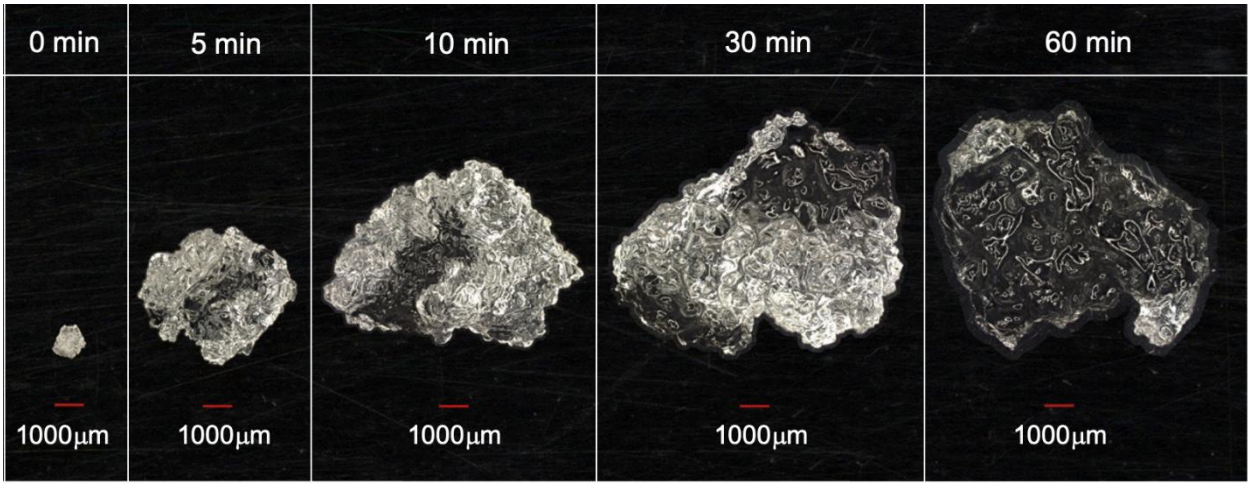

Figure 5-3: Swelling of a typical SB particle in distilled water at various times until 60 minutes.

To investigate the effect of particle size on swelling behavior, Figure 5-4. (a) presents the variation of swollen volume of SB particles with respect to the dry volumes in distilled water. Larger SB particles exhibit higher absorption, primarily due to the increased number of polymer chains that are capable of hydrogen bonding [144]. Smaller particles absorb less water overall, as they contain fewer internal polymer chains when compared to larger particles, but their higher surface area allows absorption through weaker surface interactions, such as Van der Waals forces [20], [144], [146], [157]. However, this is not as effective as binding water through hydrogen bonding in the larger particles.

To quantitatively assess the relationship between dry and swollen volumes, three correlation coefficients, Pearson (r_p), Spearman (r_s), and distance correlation ($\mathcal{R}$), were calculated for volumes at four time points (5, 10, 30, and 60 minutes) in distilled water, as shown in Table-5-2. All three correlation coefficients indicate strong correlations between dry and swollen volumes during the first 30 minutes, with $r_p \geq 0.83$, $r_s \geq 0.78$, $\mathcal{R} \geq 0.80$. In addition, the distance correlation, which is capable of characterizing nonlinear correlations, is very close to the Pearson correlation coefficient, indicating the absence of any nonlinear correlation. This can be corroborated from the Figure 5-4. However, at 60 minutes, the correlation values decreased ($r_p = 0.61$, $r_s = 0.56$, $\mathcal{R} = 0.58$), indicating a relatively weaker correlation between dry and swollen volumes as the particles approach equilibrium.

Figure 5-4.(b) illustrates the variation of absorption rate (R_v) of SB particles with respect to the dry particle volume at various time points in distilled water. Since the absorption rate is calculated based on the change in swollen volume over time (Equation 1), the same correlation analysis applied to Figure 5-4.(a) is also relevant for interpreting Figure 5-4.(b). The highest absorption rates are observed at 5 and 10 minutes, and this trend gets stronger with the increase in the particle size (dry volume), as they benefit from a greater number of accessible hydrophilic sites early in the swelling process. As time progresses, the correlation declines markedly for all particles, reflecting a transition toward equilibrium as the ion concentration gradient between the SAP and surrounding medium diminishes or the elastic limit of the SAP particle is reached.

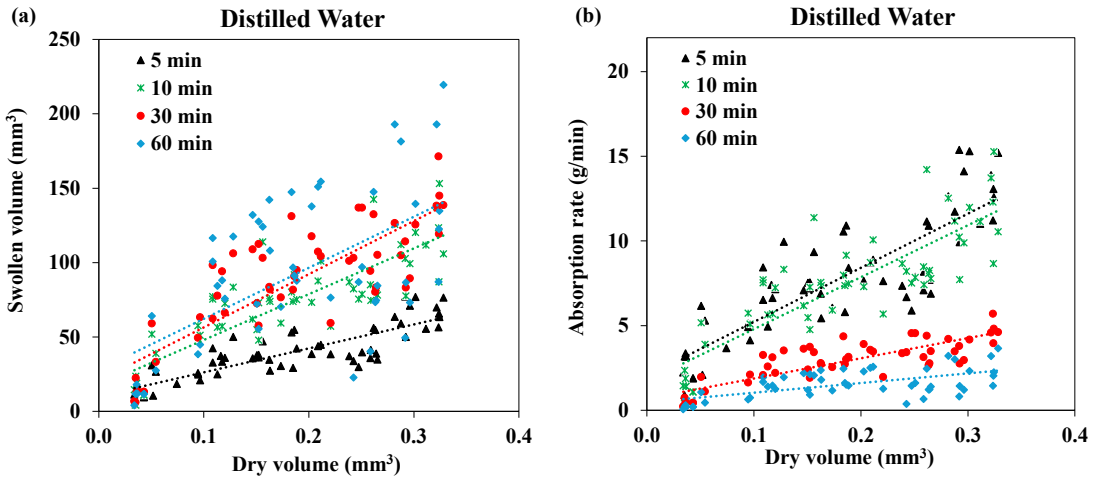

Figure 5-4: Distilled water medium: (a) swollen volume versus dry volume, and (b) absorption rate versus dry volume over time.

Table 5-2: Correlation coefficients between dry and swollen volumes in distilled water over time for SB.

Solution	Elapsed soaking time (min)	Pearson correlation (r_p)	Spearman correlation (r_s)	Distance correlation $(\mathcal{R})$
Distilled Water	5	0.849	0.855	0.820
	10	0.848	0.847	0.830
	30	0.833	0.783	0.803
	60	0.610	0.563	0.588

5.3.2 Swelling Behavior of SB in 3.5 wt.% NaCl Solution

In the saline environment, the swelling behavior of SB is markedly altered due to ionic interactions that disrupt the typical osmotic pressure-driven uptake observed in deionized water. When SB is introduced into a 3.5 wt.% NaCl solution, the carboxylate groups (COO^-) within the polymer matrix interact with free Na^+ ions from the solution. As illustrated in Figure 5-5, the yellow Na^+ ions represent sodium ions from the external NaCl solution, some of which remain in the surrounding medium while others diffuse into the polymer network. The other Na^+ ions without the circle originate from the SAP itself and are present inside the particle before exposure. This interaction results in the formation of COO^-Na^+ complexes, which reduce the number of free, dissociated COO^- groups, as illustrated in Figure 5-5. The reduction of these free negatively charged groups is referred to as the ionic shielding effect, a phenomenon that occurs when cations (in this case, Na^+) in the solution interact with negatively charged carboxylate groups, reducing the electrostatic repulsion between COO^- groups [158].

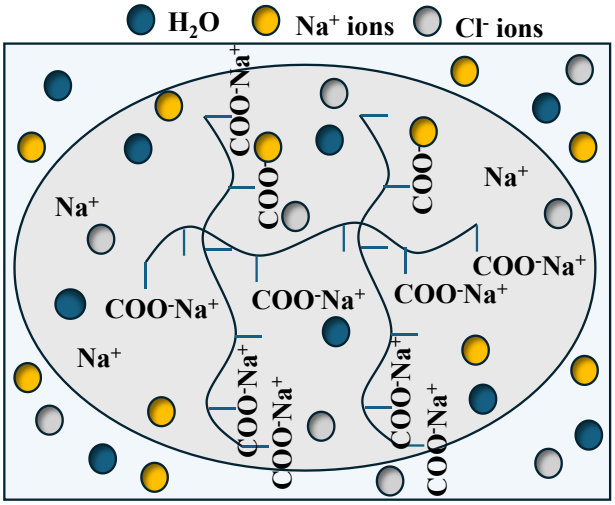

Figure 5-5: Schematic illustration of the swelling mechanism of SB in 3.5% NaCl solution.

The time-dependent swelling response of a typical SB particle in 3.5% NaCl solution is shown in Figure 5-6 for various time intervals. Compared to the behavior in distilled water, the swelling is visibly reduced at all time points. The limited swelling is directly related to the restricted repulsion of polymer chains due to the formation of ionic complexes, as discussed earlier. The particle reaches its maximum size around 30 minutes, after which negligible swelling occurs, consistent with previously reported literature [144], [145].

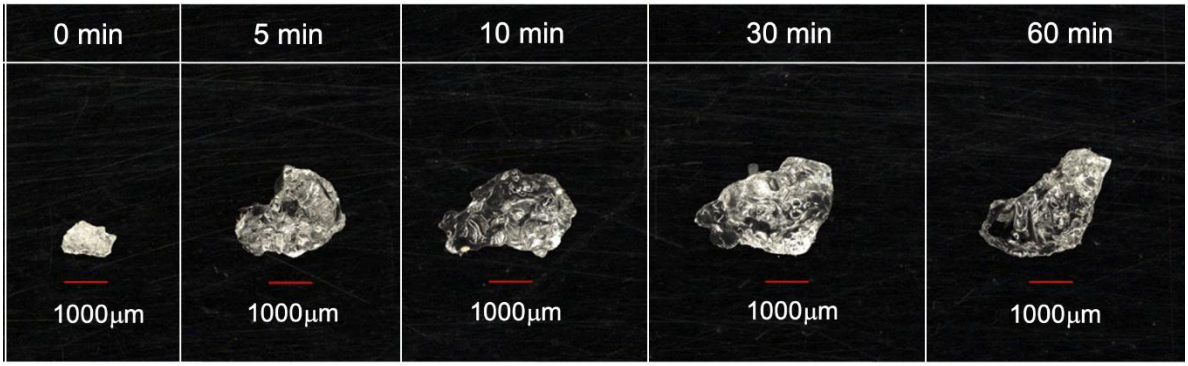

Figure 5-6: Swelling of a typical SB particle in 3.5% NaCl solution at various times until 60 minutes.

Figure 5-7 (a) presents the variation of swollen volume of SB particles with respect to the dry volumes in 3.5% NaCl solution is presented in Figure 5-7. (a). The correlation between dry and swollen volumes was evaluated using Pearson (r_p), Spearman (r_s), and distance correlation ($\mathcal{R}$) coefficients, as summarized in Table 5-3. At 5 minutes, all three correlation coefficients indicate a weaker correlation compared to later time intervals. The strength of correlation improves over time, reaching high values by 30 and 60 minutes, which suggests that the correlation between the particle size and swelling volume becomes more pronounced as time progresses. This trend is attributed to the dominant ionic shielding effect during the early stage, which suppresses electrostatic repulsion between polymer chains, thereby delaying water uptake. Over time, the influence of particle size becomes more evident, as larger SB particles exhibit higher absorption due to the increased number of polymer chains that are capable of hydrogen bonding [33,44], as previously discussed.

Figure 5-7. (b), shows the variation of absorption rate ($\boldsymbol{R_v}$) of SB particles with respect to the dry particle volume at various time points in brine solution. Although the maximum absorption rate still occurs at 5 minutes, its magnitude is markedly lower under saline conditions when compared to distilled water. For particles with dry volumes greater than 0.3 mm³, the average absorption rate during the first 5 minutes is approximately 0.59 g/min per particle in NaCl solution. In contrast, the corresponding rate in distilled water is around 12.5 g/min per particle, highlighting the significant suppression of swelling due to the ionic shielding effect in the saline medium.

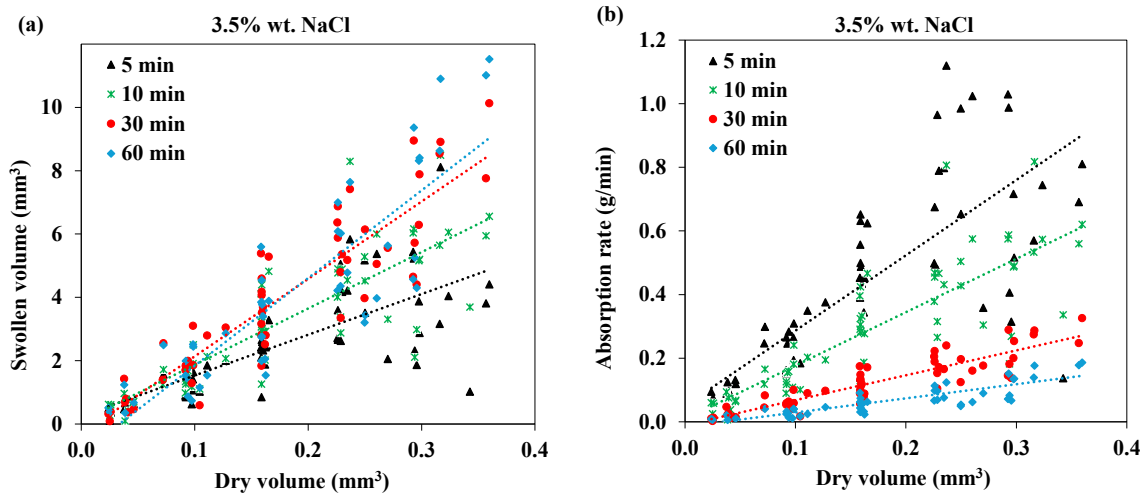

Figure 5-7: 3.5%NaCl medium : (a) swollen volume versus dry volume, and (b) absorption rate versus dry volume over time.

Table 5-3 . Correlation coefficients between dry and swollen volumes in 3.5% NaCl solution over time.

Sol	**Elapsed soaking time** (min)	**Pearson correlation** (r_p)	**Spearman correlation** (r_s)	**Distance correlation** $(\mathcal{R})$
3.5% NaCl	5	0.753	0.822	0.795
	10	0.845	0.882	0.855
	30	0.907	0.903	0.892
	60	0.869	0.878	0.848

5.3.3 Swelling Behavior of SB in Cement Pore Solution

The swelling behavior of SB in cement pore solution is markedly different due to the presence of multiple ionic species, including Ca^{2+}, Na^{+}, and K^{+}, as illustrated in Figure 5-8. These cations are released during cement hydration and interact with the negatively charged carboxylate (COO^{-}) groups within the polymer network. Such interactions induce a strong ionic shielding effect and lead to the formation of ionic complexes, which suppress the electrostatic repulsion between the carboxylate groups. In particular, multivalent cations like Ca^{2+} can connect multiple polymer chains by binding with several COO^{-} groups simultaneously (a process known as cross-linking), which tightens the polymer structure and hinders its ability to swell. The red arrows in Figure 5-8 represent these interactions between Ca^{2+} ions and the

carboxylate groups. This reduction in internal spacing leads to a denser network structure that restricts water uptake and significantly limits the swelling capacity of SB [155].

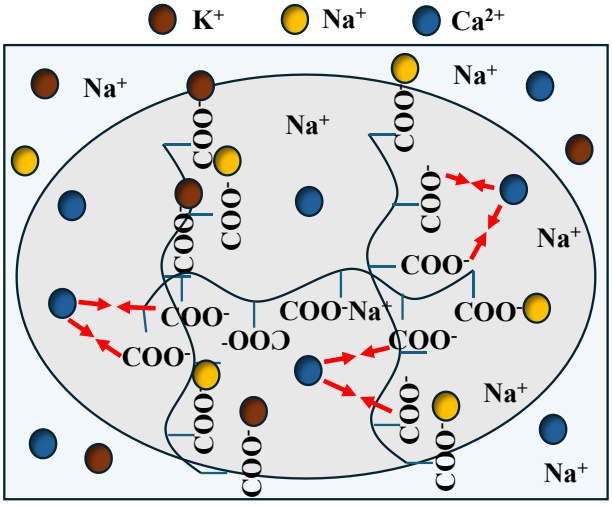

Figure 5-8: Schematic illustration of the swelling mechanism of SB in cement pore solution.

The swelling evolution of a typical SB particle in the cement pore solution is shown in Figure 5-9. Maximum swelling occurs within the first 10 minutes; however, unlike in distilled water or NaCl solution, a noticeable reduction in particle volume is observed after 30 minutes. The early-stage swelling is attributed to an initial osmotic pressure gradient between the polymer and the external pore solution. However, as cations rapidly diffuse into the polymer matrix, they form insoluble ionic complexes with carboxylate groups. The precipitation of calcium-carboxylate salts on the particle surface results in the formation of a distinct, white, crust-like layer, which is visibly evident at 30 and 60 minutes. This phenomenon is further supported by the ICP-OES results presented in Figure 5-10, which reveals an approximate 33% reduction in Ca^{2+} concentration in the pore solution following SB exposure compared to the control. This decline indicates significant calcium uptake by the SB particles, consistent with the formation of ionic cross-links and the development of the observed egg-shell-like crust on the SB surface. In parallel, Na^{+} concentration increases by approximately 154%, reflecting substantial sodium ion release from the SB matrix into the surrounding solution.

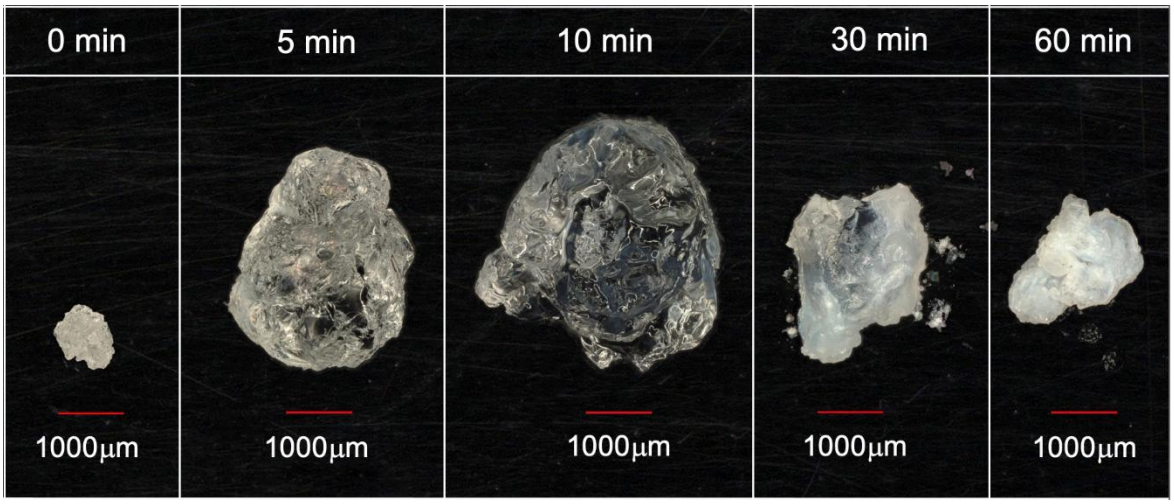

Figure 5-9: Swelling of a typical SB particle in cement pore solution at various times until 60 minutes.

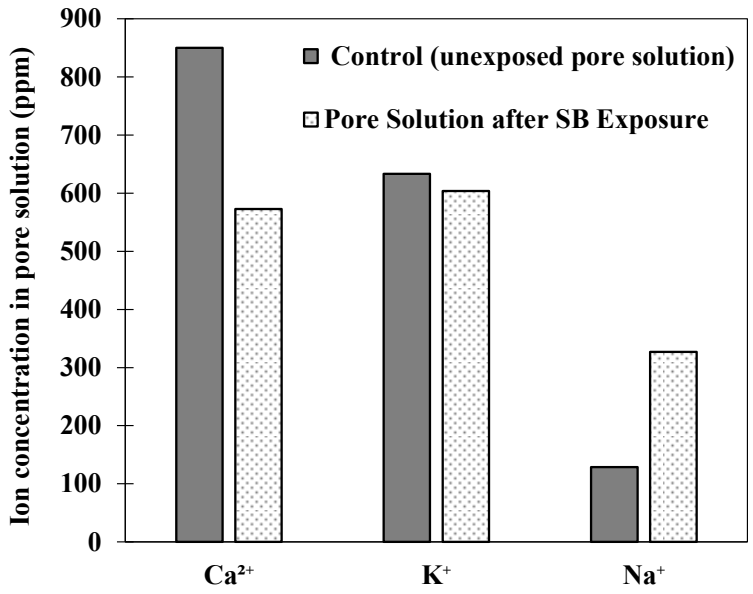

Figure 5-10: Ion concentrations in cement pore solution before and after exposure to SB, measured by ICP-OES.

To further validate the presence of calcium-rich deposits on the SB surface after exposure to cement pore solution, elemental depth profiling was conducted using LIBS. Figure 5-11 compares the elemental composition of (a) an unexposed, dried SB particle and (b) a particle exposed to cement pore solution for 60 minutes. In the unexposed sample, no calcium signal is detected across the analyzed depth layers. In contrast, the exposed particle shows a consistent presence of calcium across all five layers. This clear difference confirms that calcium from the pore solution has diffused into the polymer and formed ionic complexes. These results strongly support the ICP-OES findings and provide direct evidence of calcium accumulation within the outer regions of the polymer, consistent with the formation of the observed white crust as shown in Figure 5-9. Additionally, sodium content, which is prominent in the unexposed SB particle, is significantly reduced in the exposed particle, with no clear sodium signal detected in the depth profile. This further corroborates the occurrence of ion exchange, where Na^+ ions are displaced by multivalent cations such as Ca^{2+}.

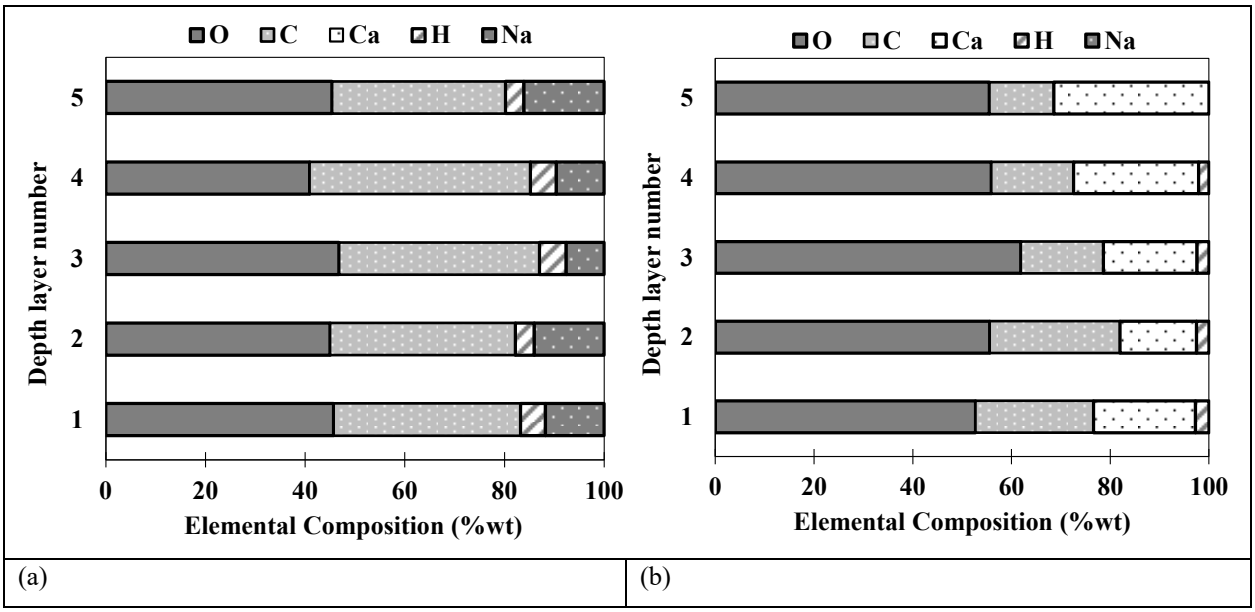

Figure 5-11: Elemental composition of SB particles analyzed by LIBS: (a) unexposed SB showing no calcium signal, and (b) SB exposed to cement pore solution for 60 minutes showing calcium presence across all depth layers and reduced sodium content.

The particle size-dependent swelling behavior is presented in Figure 5-12.(a). The correlation between dry and swollen volumes was assessed using Pearson (r_p), Spearman (r_s), and distance correlation ($\mathcal{R}$) coefficients, as presented in Table 5-4. At 5 minutes, all three coefficients indicate a strong correlation ($r_p = 0.916$ $r_s = 0.906$, $\mathcal{R} = 0905$), which progressively declines over time. As particle size increases, swelling is initially enhanced due to the increased accessible polymer chains capable of forming stronger hydrogen bonds. However, the influence of multivalent cations such as Ca^{2+} becomes increasingly dominant as time progresses. These cations form ionic complexes by additional cross-links with carboxylate groups, reducing the osmotic pressure gradient and diminishing electrostatic repulsion between polymer chains. The concurrent precipitation of calcium, as previously discussed, contributes to deswelling by releasing absorbed water [155].

Figure 5-12. (b) shows the variation of the absorption rate (R_v) of SB particles with respect tothe dry particle volume at various time points in the cement pore solution. Similar to the brine solution, the maximum absorption rate occurs at 5 minutes but remains substantially lower than in distilled water. For particles with dry volumes greater than 0.3 mm^3, the average absorption rate during the first 5 minutes is approximately 1.9 g/min per particle. This reduced absorption is primarily attributed to the formation of ionic complexes, which lower the osmotic pressure gradient and hinder further water uptake.

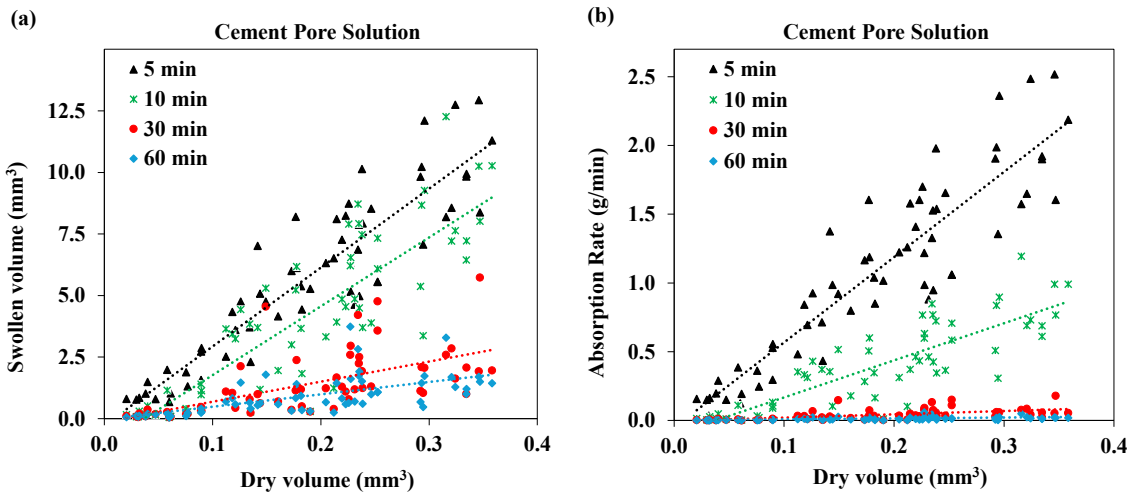

Figure 5-12: Cement pore medium: (a) swollen volume versus dry volume, and (b) absorption rate versus dry volume over time.

Table 5-4 . Correlation coefficients between dry and swollen volumes in cement pore solution over time.

Solution	Elapsed soaking time (min)	Pearson correlation (r_p)	Spearman correlation (r_s)	Distance correlation $(\mathcal{R})$
Cement pore	5	0.916	0.906	0.905
	10	0.848	0.861	0.831
	30	0.617	0.775	0.697
	60	0.622	0.763	0.700

5.3.4 Comparative Analysis of Swelling Behavior Across Media

Figure 5-13 compares the swollen volume of SB particles in distilled water, 3.5 wt.% NaCl, and cement pore solution at 5, 10, 30, and 60 minutes. Across all time points, SB particles exhibit the greatest swelling in distilled water, with pronounced reduced swelling in cement pore solution and 3.5 wt.% NaCl solution. The superior swelling in distilled water is attributed to a high osmotic pressure gradient and strong electrostatic repulsion between carboxylate groups, which enable rapid water uptake.

At 5 minutes (see Figure 5-13. (a)), swelling in NaCl solution is significantly reduced due to the ionic shielding effect of Na^+ ions, which form ionic complexes with carboxylate groups. The cement pore solution, on the other hand, exhibits a higher swollen volume than NaCl at 5 minutes, likely due to the presence of a diverse set of ions. However, over time, the presence of cations like Ca^{2+} in cement pore solution exhibits a strong affinity for carboxylate groups, forming ionic cross-links and insoluble calcium-carboxylate complexes. This interaction decreases osmotic pressure and electrostatic repulsion, thereby suppressing further swelling.

Additionally, calcium precipitation both on the surface and within the matrix leads to deswelling and partial particle degradation. Consequently, as shown in Figure 5-13. (c) and Figure 5-13. (d), SB particles in cement pore solution show the lowest swollen volumes at 30 and 60 minutes.

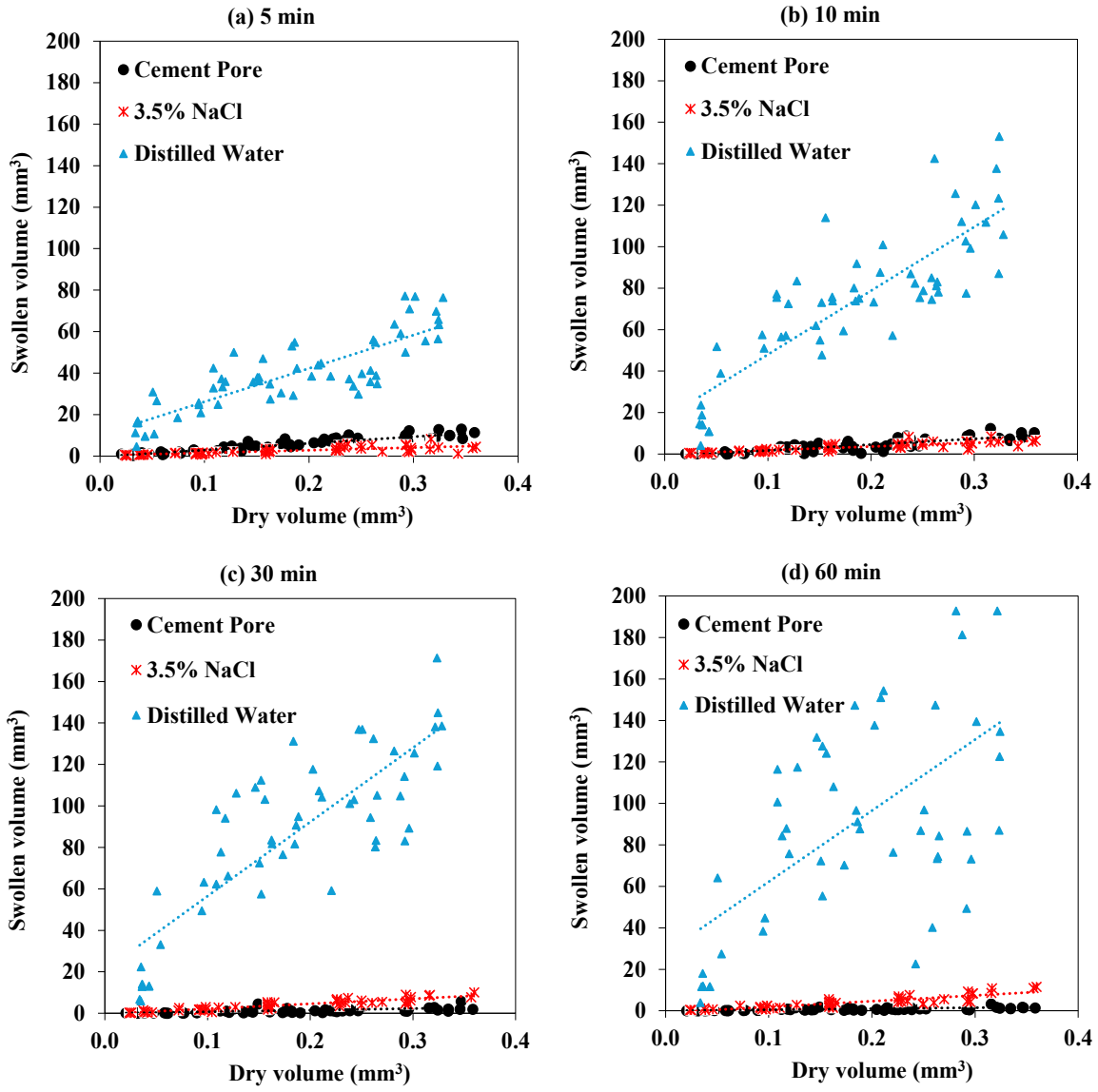

Figure 5-13: Comparison of the swollen particle volume across different media at: (a) 5 minutes; (b) 10 minutes; (c) 30 minutes; and (d) 60 minutes.

To visualize the swelling characteristics of SB particles, Figure 5-14 presents the volume evolution of five particles with similar initial volumes (greater than 0.3 mm³) in distilled water, 3.5 wt.% NaCl solution, and cement pore solution. After reaching maximum swelling within the first few minutes, the swollen volumes in both distilled water and NaCl solution stabilize over time. In contrast, particles in the cement pore solution exhibit a pronounced decline in volume after the initial swelling, indicating significant deswelling behavior. At 60 minutes, the average swollen volume of SB particles is approximately 137.70 mm³ in distilled water, 8.41 mm³ in 3.5% NaCl solution, and 1.52 mm³ in the

cement pore solution. The sharp decline in the cement pore curves is primarily attributed to the interaction between calcium ions and the carboxylate groups of the polymer, which induces ionic cross-linking and the precipitation of calcium–carboxylate salts. This reaction lowers the osmotic pressure gradient and reduces water retention, leading to progressive deswelling.

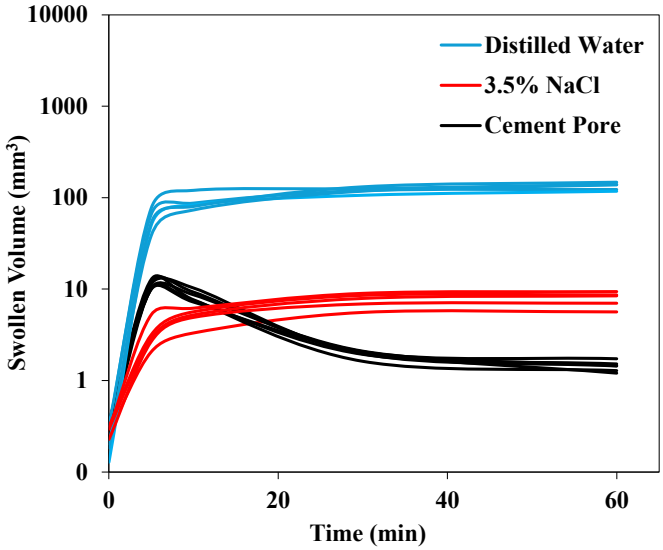

Figure 5-14: Time-dependent swelling behavior of five SB particles in distilled water, 3.5 wt.% NaCl solution, and cement pore solution

6 Conclusions and Recommendations

This chapter summarizes the important conclusions of this project followed by a list of recommendations for future research.

6.1 Super Absorbent Polymers (SAPs) as Concentration Preservers in Brine Deicers for Enhanced Ice Melting Capacity

The following conclusions can be drawn from the present study:

The water absorption capacity of SAPs in brine solution approximately decreased by 97%, 97%, 98%, 94%, and 88% for SAP-SA, SB, SC, SD, and SE, respectively, compared to the deionized water absorption capacity.

SAP-SE had the highest water absorption capacity (24 grams/gram) in salt brine solution. This is due to the increased osmatic pressure induced by the presence of potassium ions in the SAP-SE mixed with sodium and chloride ions in the salt brine solution. In contrast, the presence of similar sodium ions in other SAPs leads to lower osmotic pressure, reducing their water absorption capacity when compared to SE.

Adding or replacing NaCl with 5% large-sized SAPs (SA and SB) in the brine solution significantly increased their ice melting capacity at all subfreezing temperatures. The addition of merely 5% large-sized SA into the 23.3% wt. NaCl brine solution increased the ice melting capacity by up to 65% at T=-20°C and 80% at T=-30°C. Likewise, replacing NaCl with 5% large-sized SAP (SA and SB) in the brine solution enhanced their ice melting capacity by up to 40% at T=-30°C compared to the traditional brine deicer.

The ice melting capacity of SE at all the deicing temperatures and weight fractions is lower than that of the reference salt brine. This subpar performance can be attributed to its high saltwater absorption leaving behind free water that has lower concentration of salt.

Adding or replacing 5% of SAPs in the brine solution demonstrated superior performance compared to the 10% addition group at all subfreezing temperatures in the ice melting test.

Adding or replacing 5% large-sized SAPs (SA and SB) resulted in the lowest BPN reduction (1% for SA and 2% for SB) compared to dry surface in both asphalt and PCC pavements.

A notable reduction in skid resistance is observed when 10% of SAPs are added to the brine solution, indicating that higher weight concentrations of additives increase slipperiness on the pavement surface.

The SAP-brine deicers introduced in this study can be applied directly to the pavement surface like the traditional salt brine deicers. Specifically, replacing NaCl with 5% large-sized SAP (SA and SB) in traditional brine deicer can enhance the ice melting efficiency at extreme subfreezing temperatures while reducing the consumption of chloride-based salt. This innovative approach holds the potential to bring about a transformative change in the deicing industry, particularly within regions characterized by severely cold climatic conditions.

Based on the results of the current study, several avenues for future research can be explored to further enhance the efficacy and sustainability of deicing methods using SAP-brine solutions. This section highlights some of the recommendations as follows:

New environmentally friendly SAP formulations can be tailored specifically for deicing applications to enhance ice melting performance. Exploring alternatives such as organic compounds or biodegradable polymers could offer sustainable solutions that reduce environmental impact while maintaining or improving ice melting efficiency.

Investigating the fundamental mechanisms responsible for variations in absorption properties among different SAP types in a salt brine environment is essential. Future research should focus on factors such as particle size, crosslinking density, and polymer composition to optimize SAP formulations for enhanced performance in deicing applications.

Real-world performance of SAP-brine deicers can be assessed through long-term field trials to understand their effectiveness and durability across different road types and various climatic conditions.

Detailed cost analysis can be conducted to evaluate the production, application, and maintenance costs of SAP-brine solutions compared to traditional deicers. Potential cost savings can be considered from reduced salt usage and improved road safety, as well as the scalability of production and distribution for wider adoption.

A comprehensive environmental life cycle analysis (LCA) can be performed to understand the broader ecological implications of using SAP-brine deicers. The environmental footprint of the product can be assessed from production to disposal, including potential impacts on soil, water sources, and local ecosystems.

6.2 Lowering Freezing Point and Improving Ice Melting Capacity of Deicers with Xylitol and Erythritol

The following conclusions could be drawn from this study:

1. The addition of polyols to a 23.3 % NaCl deicing solution successfully reduced the freezing point below −21.1°C, with a 12.50% erythritol-brine solution and a 12.50% xylitol-brine solution showing optimal performance. These solutions lowered the freezing point to approximately -37.53°C and -35.37°C, respectively, outperforming other tested concentrations.
2. Xylitol and erythritol-based NaCl deicers exhibited superior ice melting capacity even at sub-freezing temperatures when compared to salt brine deicer alone. When 12.50% xylitol is added to the salt brine deicer, a 16% increase in the ice melting is observed at -20°C, when compared to the reference 23.3% NaCl deicer, whereas addition of 12.50% erythritol led to a 23% increase in the ice melting capacity.
3. The 12.50% xylitol-based NaCl deicing solution exhibited optimal performance in generating sufficient frictional force to prevent vehicle tires from skidding when compared to the reference 23.3% NaCl deicing solution.
4. Addition of polyols did not result in considerable changes in DO levels of the lake water for the temperatures studied herein. The polyol-modified deicers exhibited up to a 24% increase in dissolved oxygen in lake water when compared to the salt brine deicer.

Experimental results suggest that a combination of 12.50% xylitol with a 23.3% NaCl deicing solution is well-suited for deicing in regions where temperatures fall below -20°C, considering skid resistance and environmental aspects. The polyol-enhanced deicing solutions developed in this study can be applied directly to pavement surfaces or used for pre-wetting in deicing operations. Future research will focus on assessing the performance of these polyol-brine solutions through direct road application.

6.3 Mitigating Corrosion Damage in Steel Employing Biobased Erythritol and Xylitol as Corrosion Inhibitions

In this research, the corrosion inhibition performance of erythritol and xylitol is investigated in traditional deicing media (23% wt. of $NaCl\ solution$). Based on the discussion, the following conclusions are drawn.

Accelerated corrosion tests showed relatively less and delayed corrosion on the surface of the ASTM A572 steel specimens subjected to the recurring flow of deicing media containing erythritol and xylitol, which is attributed to the adherence of erythritol and xylitol to the steel surface.

The polarization curves displayed typical tafel behavior, wherein the logarithmic current density linearly varies with change in potential. For the deicing media containing erythritol and xylitol, the polarization curves shifted towards the low current and more noble potential regions, indicating that both erythritol and xylitol retard electrochemical reactions and inhibit corrosion.

The deicing media containing erythritol showed CIEs in a range of 68% to 88%. Similarly, the presence of xylitol revealed CIEs in a range of 81% to 93%. These observations conclude that adding small amounts of polyols substantially improved the corrosion inhibition in ASTM A 572 steel subjected to deicing media.

The presence of 3% erythritol in deicing media, reduced the corrosion rate (0.090 $mm/year$) by 87%, while the presence of xylitol decreased the corrosion rate (0.051 $mm/year$) by 93%, in comparison to traditional deicing media (0.742 $mm/year$) containing no polyols.

The adsorption isotherms for erythritol and xylitol obey the straight-line model, while the ΔG_{ads}^{0} for erythritol (-15.10kJ/mol) and xylitol (-17.68 kJ/mol) are mixed type of corrosion inhibitors, suggesting that both these polyols spontaneously physisorbed onto the steel specimens in the brine solution.

Finally, the SEM-EDX and XRD analyses confirm the increased formation of corrosion products on the surface of the steel specimens subjected to the deicing solution containing no polyols. Conversely, the specimens subjected to a deicing solution containing erythritol and xylitol exhibit a reversed trend, indicating their effective corrosion protection performance in chloride environments.

6.4 Correlation between dry and swollen superabsorbent polymer particle sizes in cement pore solution and salt brine

The following conclusions can be drawn from the present study:

The swelling capacity of SB was highly sensitive to the ionic composition of the surrounding medium. In distilled water, SB exhibited the highest swelling due to the presence of a high osmotic pressure gradient and electrostatic repulsion between carboxylate groups.

In 3.5 wt.% NaCl solution, swelling was substantially reduced due to the ionic shielding effect of sodium ions. These ions formed ionic complexes with carboxylate groups, which reduced the number of free ionized sites, suppressed electrostatic repulsion, and decreased the osmotic pressure gradient.

Cement pore solution also led to low swelling behavior. This reduction was attributed to the presence of multivalent cations (e.g., Ca^{2+}), which not only shielded charges but also introduced ionic cross-linking by simultaneously interacting with multiple carboxylate groups, thereby restricting swelling. In later stages, deswelling occurred due to calcium-carboxylate precipitation and white crust formation, which further limited water retention.

Particle size played a dominant role in the swelling behavior observed across all media. Correlation analyses (Pearson, Spearman, and distance correlation) consistently demonstrated strong size dependence in the early stages of swelling, particularly in distilled water and cement pore solution. However, in cement pore solution, this size-dependent effect decreased over time due to degradation and deswelling processes, but remained high enough to consider it as an important factor.

Across all media, the highest absorption rates occurred within the first 5 minutes, emphasizing the initial impact of osmotic pressure gradients. Distilled water showed the highest absorption rate (~12.5 g/min), followed by cement pore solution (~1.9 g/min), and 3.5 wt.% NaCl (~0.59 g/min). The suppressed rates in saline and cement pore environments were consistent with the ionic complexation and reduced osmotic pressure discussed earlier.

References

[1] V. Mechtcherine *et al.*, “Application of super absorbent polymers (SAP) in concrete construction—update of RILEM state-of-the-art report,” *Mater. Struct. Constr.*, vol. 54, no. 2, 2021, doi: 10.1617/s11527-021-01668-z.

[2] S. Zhao, O. M. Jensen, M. T. Hasholt, and X. Guan, “Absorption capacity of superabsorbent polymer in cement pastes: a robustness test,” *Mater. Struct. Constr.*, vol. 54, no. 1, pp. 1–15, 2021, doi: 10.1617/s11527-021-01636-7.

[3] D. Snoeck, C. Schröfl, and V. Mechtcherine, “Recommendation of RILEM TC 260-RSC: testing sorption by superabsorbent polymers (SAP) prior to implementation in cement-based materials,” *Mater. Struct. Constr.*, vol. 51, no. 5, 2018, doi: 10.1617/s11527-018-1242-8.

[4] H. Yang, M. Liu, H. Bian, L. Wu, J. Liu, and W. Wang, “The influence of SAP particle size and extra water on the dynamic mechanical behavior of SAP-modified cement-based composites,” *Constr. Build. Mater.*, vol. 347, no. 17, p. 128622, 2022, doi: 10.1016/j.conbuildmat.2022.128622.

[5] D. Snoeck and N. De Belie, “Repeated Autogenous Healing in Strain-Hardening Cementitious Composites by Using Superabsorbent Polymers,” *J. Mater. Civ. Eng.*, vol. 28, no. 1, pp. 1–11, 2016, doi: 10.1061/(asce)mt.1943-5533.0001360.

[6] X. Ma, Q. Yuan, J. Liu, and C. Shi, “Effect of water absorption of SAP on the rheological properties of cement-based materials with ultra-low w/b ratio,” *Constr. Build. Mater.*, vol. 195, pp. 66–74, 2019, doi: 10.1016/j.conbuildmat.2018.11.050.

[7] Y. Tan, X. Lu, R. He, H. Chen, and Z. Wang, “Influence of superabsorbent polymers (SAPs) type and particle size on the performance of surrounding cement-based materials,” *Constr. Build. Mater.*, vol. 270, p. 121442, 2021, doi: 10.1016/j.conbuildmat.2020.121442.

[8] a276, “Standard Specification for Stainless Steel Bars and Shapes,” *ASTM Int.*, vol. 10, pp. 1–7, 2012, doi: 10.1520/A0276.

[9] B. Fotovvati, N. Namdari, and A. Dehghanghadikolaei, “On coating techniques for surface protection: A review,” *J. Manuf. Mater. Process.*, vol. 3, no. 1, 2019, doi: 10.3390/jmmp3010028.

[10] M. Criado, D. M. Bastidas, S. Fajardo, A. Fernández-Jiménez, and J. M. Bastidas, “Corrosion behaviour of a new low-nickel stainless steel embedded in activated fly ash mortars,” *Cem. Concr. Compos.*, vol. 33, no. 6, pp. 644–652, 2011, doi: 10.1016/j.cemconcomp.2011.03.014.

[11] N. A. Farhan, M. N. Sheikh, and M. N. S. Hadi, “Experimental Investigation on the Effect of Corrosion on the Bond Between Reinforcing Steel Bars and Fibre Reinforced Geopolymer Concrete,” *Structures*, vol. 14, no. March, pp. 251–261, 2018, doi: 10.1016/j.istruc.2018.03.013.

[12] Z. Zhou and P. Qiao, “Bond behavior of epoxy-coated rebar in ultra-high performance concrete,” *Constr. Build. Mater.*, vol. 182, pp. 406–417, 2018, doi: 10.1016/j.conbuildmat.2018.06.113.

[13] A. Afshar, S. Jahandari, H. Rasekh, M. Shariati, A. Afshar, and A. Shokrgozar, “Corrosion resistance evaluation of rebars with various primers and coatings in concrete modified with different additives,” *Constr. Build. Mater.*, vol. 262, p. 120034, 2020, doi: 10.1016/j.conbuildmat.2020.120034.

[14] M. Li, T. Su, Y. Chen, H. He, and X. Yang, “Salt spray aging effects on dynamic responses and failure characteristics of hybrid bonded-riveted CFRP/Al joints under high speed loading,” *J. Manuf. Process.*, vol. 72, no. September, pp. 582–593, 2021, doi: 10.1016/j.jmapro.2021.10.048.

[15] Y. Li *et al.*, “A review on durability of basalt fiber reinforced concrete,” *Compos. Sci. Technol.*, vol. 225, no. May, p. 109519, 2022, doi: 10.1016/j.compscitech.2022.109519.

[16] T. Ayub, N. Shafiq, and M. F. Nuruddin, “Mechanical properties of high-performance concrete reinforced with basalt fibers,” *Procedia Eng.*, vol. 77, pp. 131–139, 2014, doi: 10.1016/j.proeng.2014.07.029.

[17] American Society of Civil Engineers, “2017 Infrastructure Report Card: A comprehensive assessment of America’s Infrastructure,” *Asce*, p. 111, 2017, [Online]. Available: https://www.infrastructurereportcard.org/

[18] B. Tutkun and H. Yazıcı, “Effect of absorption determining methods of superabsorbent polymers in cementitious environments on the fresh properties,” *Mater. Today Proc.*, vol. 81, pp. 43–49, 2023, doi: 10.1016/j.matpr.2022.11.403.

[19] Á. Vega-Zamanillo, L. Juli-Gándara, M. Á. Calzada-Pérez, and E. Teijón-López-Zuazo, “Impact of temperature changes and freeze-thaw cycles on the behaviour of asphalt concrete submerged in water with sodium chloride,” *Appl. Sci.*, vol. 10, no. 4, pp. 1–12, 2020, doi: 10.3390/app10041241.

[20] Y. Zhuo *et al.*, “Gels as emerging anti-icing materials: A mini review,” *Mater. Horizons*, vol. 8, no. 12, pp. 3266–3280, 2021, doi: 10.1039/d1mh00910a.

[21] T. Abbas, D. N. Lavadiya, and R. Kiran, “Exploring the use of polyols, corn, and beet juice for decreasing the freezing point of brine solution for deicing of pavements,” *Sustain.*, vol. 13, no. 11, 2021, doi: 10.3390/su13115765.

[22] Y. Bachra, A. Grouli, F. Damiri, X. X. Zhu, M. Talbi, and M. Berrada, “Synthesis, Characterization, and Swelling Properties of a New Highly Absorbent Hydrogel Based on Carboxymethyl Guar Gum Reinforced with Bentonite and Silica Particles for Disposable Hygiene Products,” *ACS Omega*, vol. 7, no. 43, pp. 39002–39018, 2022, doi: 10.1021/acsomega.2c04744.

[23] K. Zhang, W. Feng, and C. Jin, “Protocol efficiently measuring the swelling rate of hydrogels,” *MethodsX*, vol. 7, no. September 2019, p. 100779, 2020, doi: 10.1016/j.mex.2019.100779.

[24] B. M. Gerbino-Bevins, C. Y. Tuan, and M. Mattison, “Evaluation of ice-melting capacities of deicing chemicals,” *J. Test. Eval.*, vol. 40, no. 6, 2012, doi: 10.1520/JTE104460.

[25] S. Afgan, R. Kiran, and X. Qi, “Mitigating corrosion damage in steel employing biobased erythritol and xylitol as corrosion inhibitions,” vol. 37, no. August, pp. 1–14, 2024, doi: 10.1061/JMCEE7.MTENG-18945.

[26] L. P. Esteves, “Superabsorbent polymers: On their interaction with water and pore fluid,” *Cem. Concr. Compos.*, vol. 33, no. 7, pp. 717–724, 2011, doi: 10.1016/j.cemconcomp.2011.04.006.

[27] K. Nilssen, A. Klein-Paste, and J. Wåhlin, “Accuracy of ice melting capacity tests: Review of melting data for sodium chloride,” *Transp. Res. Rec.*, vol. 2551, pp. 1–9, 2016, doi: 10.3141/2551-01.

[28] C. C. Chappelow, A. D. McElroy, and R. R. Blackburn, “Handbook of Test Methods for Evaluating Chemical Deicers, Report No. SHRP-H-332,” *Natl. Res. Counc.*, pp. 31–42, 1992.

[29] R. K. Yellavajjala, D. N. Lavadiya, and H. U. Sajid, *Corn-Based Deicers (Final Report for IHRB Project TR-754*, no. July. 2020. [Online]. Available: https://orcid.org/0000-0002-2370-8592

[30] T. F. Fwa, “Skid resistance determination for pavement management and wet-weather road safety,” *Int. J. Transp. Sci. Technol.*, vol. 6, no. 3, pp. 217–227, 2017, doi: 10.1016/j.ijtst.2017.08.001.

[31] I. M. Asi, “Evaluating skid resistance of different asphalt concrete mixes,” *Build. Environ.*, vol. 42, no. 1, pp. 325–329, 2007, doi: https://doi.org/10.1016/j.buildenv.2005.08.020.

[32] B. Mataei, H. Zakeri, M. Zahedi, and F. M. Nejad, “Pavement Friction and Skid Resistance Measurement Methods: A Literature Review,” *Open J. Civ. Eng.*, vol. 06, no. 04, pp. 537–565, 2016, doi: 10.4236/ojce.2016.64046.

[33] A. Ueckermann, D. Wang, M. Oeser, and B. Steinauer, “Calculation of skid resistance from texture measurements,” *J. Traffic Transp. Eng. (English Ed.*, vol. 2, no. 1, pp. 3–16, 2015, doi: 10.1016/j.jtte.2015.01.001.

[34] T. Andriejauskas, V. Vorobjovas, and V. Mielonas, “Evaluation of skid resistance characteristics and measurement methods,” *9th Int. Conf. Environ. Eng. ICEE 2014*, no. May, 2014, doi: 10.3846/enviro.2014.141.

[35] A. Ueckermann, D. Wang, M. Oeser, and B. Steinauer, “A contribution to non-contact skid resistance measurement,” *Int. J. Pavement Eng.*, vol. 16, no. 7, pp. 646–659, 2015, doi: 10.1080/10298436.2014.943216.

[36] X. Shi, Y. Liu, M. Mooney, B. Hubbard, L. Fay, and A. Leonard, “Effect of Chloride-based Deicers on Reinforced Concrete Structures,” no. July, p. 86, 2010, [Online]. Available: https://rosap.ntl.bts.gov/view/dot/23879

[37] I. M. Asi, “Evaluating skid resistance of different asphalt concrete mixes,” *Build. Environ.*, vol. 42, no. 1, pp. 325–329, 2007, doi: 10.1016/j.buildenv.2005.08.020.

[38] A. Ben Slimane, M. Khoudeir, J. Brochard, and M. T. Do, “Characterization of road microtexture by means of image analysis,” *Wear*, vol. 264, no. 5–6, pp. 464–468, 2008, doi: 10.1016/j.wear.2006.08.045.

[39] I. News, I. Projects, M. Design, M. Testing, P. Management, and Q. Management, “SKID RESISTANCE : WHY IT ’ S IMPORTANT AND HOW TO MEASURE,” pp. 4–7, 2021.

[40] O. A. Abaza, T. D. Chowdhury, and M. Arafat, “Comparative Analysis of Skid Resistance for Different Roadway Surface Treatments,” *Am. J. Eng. Appl. Sci.*, vol. 10, no. 4, pp. 890–899, 2017, doi: 10.3844/ajeassp.2017.890.899.

[41] Y. Senga, A. Dony, J. Colin, S. Hamlat, and Y. Berthaud, “Study of the skid resistance of blends of coarse aggregates with different polish resistances,” *Constr. Build. Mater.*, vol. 48, pp. 901–907, 2013, doi: 10.1016/j.conbuildmat.2013.07.040.

[42] C. Engineering *et al.*, “Copyright ASCE 2010 GeoShanghai 2010 International Conference Copyright ASCE 2010 GeoShanghai 2010 International Conference,” pp. 1–31, 2008.

[43] J. Wei *et al.*, “Study on the Skid Resistance Deterioration Behavior of the SMA Pavement,” *Sustain.*, vol. 14, no. 5, 2022, doi: 10.3390/su14052864.

[44] J. Wåhlin and A. Klein-Paste, “The effect of mass diffusion on the rate of chemical ice melting using aqueous solutions,” *Cold Reg. Sci. Technol.*, vol. 139, no. April, pp. 11–21, 2017, doi: 10.1016/j.coldregions.2017.04.001.

[45] S. Küresel *et al.*, “No 主観的健康感を中心とした在宅高齢者における 健康関連指標に関する共分散構造分析Title,” *Ege Eğitim Dergisi/ Ege J. Educ.*, 2014.

[46] V. Mechtcherine *et al.*, “Effect of superabsorbent polymers (SAP) on the freeze–thaw resistance of concrete: results of a RILEM interlaboratory study,” *Mater. Struct. Constr.*, vol. 50, no. 1, 2017, doi: 10.1617/s11527-016-0868-7.

[47] R. K. Yellavajjala and S. Hizb Ullah, Afgan, *Final Report IHRB Project TR-788 July 2023 Sponsored by the IOWA Highway TR-788 : Mitigation of Corrosion Through Chemosorption*, no. July. 2023.

[48] R. K. Yellavajjala and S. Hizb Ullah, Afgan, *FINAL REPORT IHRB PROJECT TR-788 JULY 2023 SPONSORED BY THE IOWA HIGHWAY TR-788 : MITIGATION OF CORROSION THROUGH Chemosorption*, no. July. 2023.

[49] S. Afgan, R. Kiran, X. Qi, and D. S. Bajwa, “Enhancement of corrosion resistance and bond strength in rebars employing abrasives-infused soy-protein isolate coatings,” *Constr. Build. Mater.*, vol. 407, no. June, p. 133455, 2023, doi: 10.1016/j.conbuildmat.2023.133455.

[50] T. URAJI, H. KOHNO, H. YOSHIMURA, M. SHIMOYAMADA, and K. WATANABE, “Freezing Point Depression of Polyol-Aqueous Solutions in the High Concentration Range.,” *Food Sci. Technol. Int. Tokyo*, vol. 2, no. 1, pp. 38–42, 1996, doi: 10.3136/fsti9596t9798.2.38.

[51] M. Akin and X. Shi, “Development of Standardized Test Procedures for Evaluating Deicing Chemicals,” vol. 5, no. March, p. 97p, 2010, [Online]. Available: http://wisdotresearch.wi.gov/wp-content/uploads/08-32deicinglabtest-f.pdf%5Cnhttp://www.clearroads.org/research-projects/downloads/08-32deicinglabtest-final-report.pdf%5Cnhttp://www.westerntransportationinstitute.org/documents/reports/4W1906_Final_Report.

[52] H. Ullah Sajid, D. L. Naik, and R. Kiran, “Improving the ice-melting capacity of traditional deicers,” *Constr. Build. Mater.*, vol. 271, p. 121527, 2021, doi: 10.1016/j.conbuildmat.2020.121527.

[53] A. Zumbé, A. Lee, and D. Storey, “Polyols in confectionery: the route to sugar-free, reduced sugar and reduced calorie confectionery,” *Br. J. Nutr.*, vol. 85, no. S1, pp. S31–S45, 2001, doi: 10.1079/bjn2000260.

[54] H. U. Sajid, R. Kiran, X. Qi, D. S. Bajwa, and D. Battocchi, “Employing corn derived products to reduce the corrosivity of pavement deicing materials,” *Constr. Build. Mater.*, vol. 263, p. 120662, 2020, doi: 10.1016/j.conbuildmat.2020.120662.

[55] X. Shi *et al.*, “Evaluation of Alternative Anti-Icing and Deicing Compounds Using Sodium Chloride and Magnesium Chloride as Baseline Deicers - Phase I,” *Color. Dep. Transp. DTD Appl. Res. Innov. Branch.*, no. February, pp. 4,105-142, 2009, [Online]. Available: https://rosap.ntl.bts.gov/view/dot/36465

[56] M. Fischel, “EVALUATION OF SELECTED DEICERS BASED ON A REVIEW OF THE LITERATURE Marion Fischel COLORADO DEPARTMENT OF TRANSPORTATION,” 2001.

[57] Y. Liu, T. F. Fwa, and Y. S. Choo, “Effect of surface macrotexture on skid resistance measurements by the British pendulum test,” *J. Test. Eval.*, vol. 32, no. 4, pp. 304–309, 2004, doi: 10.1520/jte11428.

[58] M. Kim, S. H. Kang, S. G. Hong, and J. Moon, “Influence of Effective Water-to-Cement Ratios on Internal Damage and Salt Scaling of Concrete with Superabsorbent Polymer,” *Materials (Basel).*, vol. 12, no. 23, 2019, doi: 10.3390/MA12233863.

[59] Y. Abboud *et al.*, “Corrosion inhibition of carbon steel in hydrochloric acid solution using pomegranate leave extracts,” *Corros. Eng. Sci. Technol.*, vol. 51, no. 8, pp. 557–565, 2016, doi: 10.1179/1743278215Y.0000000058.

[60] O. K. Abiola, N. C. Oforka, and E. E. Ebenso, “A potential corrosion inhibitor for acid corrosion of mild steel,” *Bull. Electrochem.*, vol. 20, no. 9, pp. 409–413, 2004, doi: 10.4236/msa.2017.86032.

[61] Z. Ahmad, “Basic Concepts in Corrosion,” *Princ. Corros. Eng. Corros. Control*, pp. 9–56, 2006, doi: 10.1016/b978-075065924-6/50003-9.

[62] D. L. Kelting and C. L. Laxson, “Review of Effects and Costs of Road De-icing with Recommendations for Winter Road Management in the Adirondack Park,” *ADKaction.org*, no. February, p. 76, 2010, [Online]. Available: http://www.protectadks.org/wp-content/uploads/2010/12/Road_Deicing-1.pdf

[63] L. Fay, X. Shi, and J. Huang, “Strategies to Mitigate the Impacts of Chloride Roadway Deicers on the Natural Environment,” *NCHRP Synth. Highw. Pract.*, 2013, [Online]. Available: https://api.semanticscholar.org/CorpusID:126610856

[64] *Guidelines for the Selection of Snow and Ice Control Materials to Mitigate Environmental Impacts*. 2007. doi: 10.17226/23178.

[65] D. L. Kelting, “Review of Effects and Costs of Road De-icing with Recommendations for Winter Road Management in the Adirondack Park Prepared by Underwritten and distributed by AdkAction.org, a citizen-led political action committee dedicated to preserving and improving t,” no. February, 2010, [Online]. Available: www.AdkAction.org

[66] E. McCafferty, *Introduction to corrosion science*. 2010. doi: 10.1007/978-1-4419-0455-3.

[67] D. Wang, Q. Zhu, Y. Su, J. Li, A. Wang, and Z. Xing, “Preparation of MgAlFe-LDHs as a deicer corrosion inhibitor to reduce corrosion of chloride ions in deicing salts,” *Ecotoxicol. Environ. Saf.*, vol. 174, no. January, pp. 164–174, 2019, doi: 10.1016/j.ecoenv.2019.01.123.

[68] S. Heinz, E. Novotny, A. Sander, and O. Mohseni, “Study of Environmental Effects of De-Icing Salt on Water Quality in the Twin Cities Metropolitan Area , Minnesota,” *Transp. Res.*, p. 88, 2008.

[69] Y. Li, Y. Fang, N. Seeley, S. Jungwirth, E. Jackson, and X. Shi, “Corrosion by chloride deicers on highway maintenance equipment,” *Transp. Res. Rec.*, no. 2361, pp. 106–113, 2013, doi: 10.3141/2361-13.

[70] Y. Qian, Y. Li, S. Jungwirth, N. Seely, Y. Fang, and X. Shi, “Review: The Application of Anti-Corrosion Coating for Preserving the Value of Equipment Asset in Chloride-Laden Environments: A Review,” *Int. J. Electrochem. Sci.*, vol. 10, no. 12, pp. 10756–10780, 2015, doi: 10.1016/s1452-3981(23)11298-3.

[71] X. Shi, *Sustainable Winter Road Operations*. 2018. doi: 10.1002/9781119185161.

[72] C. Giebson, K. Seyfarth, and J. Stark, “Influence of acetate and formate-based deicers on ASR in airfield concrete pavements,” *Cem. Concr. Res.*, vol. 40, no. 4, pp. 537–545, 2010, doi: 10.1016/j.cemconres.2009.09.009.

[73] J. M. S. Silva, S. M. Cramer, M. A. Anderson, M. I. Tejedor, and J. F. Muñoz, “Concrete microstructural responses to the interaction of natural microfines and potassium acetate based deicer,” *Cem. Concr. Res.*, vol. 55, pp. 69–78, 2014, doi: 10.1016/j.cemconres.2013.10.003.

[74] Z. Liu and W. Hansen, “Freezing characteristics of air-entrained concrete in the presence of deicing salt,” *Cem. Concr. Res.*, vol. 74, pp. 10–18, 2015, doi: 10.1016/j.cemconres.2015.03.015.

[75] Y. Farnam, H. Todak, R. Spragg, and J. Weiss, “Electrical response of mortar with different degrees of saturation and deicing salt solutions during freezing and thawing,” *Cem. Concr. Compos.*, vol. 59, pp. 49–59, 2015, doi: 10.1016/j.cemconcomp.2015.03.003.

[76] Xianming Shi, Laura Fay, Zhengxian Yang, Tuan Anh Nguyen, and Yajun Liu, “No Title,” *Corros. Rev.*, vol. 27, no. 1–2, pp. 23–52, 2009, doi: doi:10.1515/CORRREV.2009.27.1-2.23.

[77] F. Cor, R. Boyle, and M. Origin, “Ahmad, Z. (2006). INTRODUCTION TO CORROSION. Principles of Corrosion Engineering and Corrosion Control, 1–8. doi:10.1016/b978-075065924-6/50002-7,” no. 1819, 1923.

[78] M. Aliofkhazraei, Ed., “Corrosion Inhibitors, Principles and Recent Applications.” IntechOpen, Rijeka, 2018. doi: 10.5772/intechopen.70101.

[79] E. O. Fanijo and A. S. Brand, “Anti-corrosion behaviors of corn-based polyols on low carbon steel rebar,” *Clean. Mater.*, vol. 4, no. February, p. 100066, 2022, doi: 10.1016/j.clema.2022.100066.

[80] P. R. Roberge, *Handbook of corrosion engineering*, vol. 37, no. 09. 2000. doi: 10.5860/choice.37-5122.

[81] M. Ormellese, L. Lazzari, S. Goidanich, G. Fumagalli, and A. Brenna, “A study of organic substances as inhibitors for chloride-induced corrosion in concrete,” *Corros. Sci.*, vol. 51, no. 12, pp. 2959–2968, 2009, doi: 10.1016/j.corsci.2009.08.018.

[82] T. A. Söylev and M. G. Richardson, “Corrosion inhibitors for steel in concrete: State-of-the-art report,” *Constr. Build. Mater.*, vol. 22, no. 4, pp. 609–622, 2008, doi: 10.1016/j.conbuildmat.2006.10.013.

[83] M. Basik and M. Mobin, “Environmentally sustainable corrosion inhibitors in the oil and gas industry,” in *Environmentally Sustainable Corrosion Inhibitors*, INC, 2022, pp. 405–421. doi: 10.1016/b978-0-323-85405-4.00017-3.

[84] H. Ullah Sajid, D. L. Naik, and R. Kiran, “Improving the ice-melting capacity of traditional deicers,” *Constr. Build. Mater.*, vol. 271, no. October, 2021, doi: 10.1016/j.conbuildmat.2020.121527.

[85] Parchem, “Material Safety Datasheet - Erythritol,” *Material Safety Data Sheet*, no. 149. Parachem, NY 10801, pp. 1–5, 2015. [Online]. Available: https://us.vwr.com/assetsvc/asset/en_US/id/16490607/contents

[86] N. Z. Msomi, O. L. Erukainure, V. F. Salau, K. A. Olofinsan, and M. S. Islam, “Comparative effects of xylitol and erythritol on modulating blood glucose; inducing insulin secretion; reducing dyslipidemia and redox imbalance in a type 2 diabetes rat model,” *Food Sci. Hum. Wellness*, vol. 12, no. 6, pp. 2052–2060, 2023, doi: 10.1016/j.fshw.2023.03.023.

[87] K. K. Mäkinen, *Authorised EU health claims for xylitol and sugar-free chewing gum (SFCG)*, vol. 1. Woodhead Publishing Limited, 2014. doi: 10.1533/9780857098481.2.46.

[88] M. Grembecka, “Sugar alcohols—their role in the modern world of sweeteners: a review,” *Eur. Food Res. Technol.*, vol. 241, no. 1, pp. 1–14, 2015, doi: 10.1007/s00217-015-2437-7.

[89] ASTM A572/A572M, “Standard specification for high-strength low-alloy columbium-vanadium structural.” ASTM, pp. 6–9, 2021. doi: 10.1520/A0572_A0572M-21E01.

[90] S. Afgan and R. Kiran, “Erythritol for internal corrosion inhibition in crude oil pipelines,” *Pipelines 2024*, no. Feldman 2016, pp. 134–142, 2024, doi: 10.1061/9780784485590.016.

[91] ETA, “Hot rolled products and structural components made of steel grades Q235B, Q235D, Q345B and Q345D,” *Standards*, no. April 2015, 2015, [Online]. Available: https://www.eota.eu/download?file=/2014/14-20-0017/ead for ojeu/ead 200017-00-0302_ojeu2016.pdf

[92] B. Jiang, Y. Qu, M. Wang, G. Lou, and G. Li, “Mechanical properties and constitutive model of Q460 steel during the fire-cooling stage,” *Thin-Walled Struct.*, vol. 189, no. May, p. 110904, 2023, doi: 10.1016/j.tws.2023.110904.

[93] H. U. Sajid and R. Kiran, “Influence of corrosion and surface roughness on wettability of ASTM A36 steels,” *J. Constr. Steel Res.*, vol. 144, pp. 310–326, 2018, doi: 10.1016/j.jcsr.2018.01.023.

[94] ASTM International, “Standard Practice for Operating Salt Spray (FOG) Apparatus.,” *Water*, vol. 03, no. February, pp. 1–15, 2003, doi: 10.1520/B0117.

[95] I. J.JS, “Image online software,” 2022. https://ij.imjoy.io/

[96] T. Progress, “Standard Test Method for Conducting Potentiodynamic Polarization Resistance Measurements,” *Policy*, vol. 26, no. 5, pp. 3–5, 2009, doi: 10.1520/G0059-97R20.2.

[97] R. I. Holland, “Use of potentiodynamic polarization technique for corrosion testing of dental alloys,” *Eur. J. Oral Sci.*, vol. 99, no. 1, pp. 75–85, 1991, doi: 10.1111/j.1600-0722.1991.tb01026.x.

[98] H. W. Song and V. Saraswathy, “Analysis of corrosion resistance behavior of inhibitors in concrete using electrochemical techniques,” *Met. Mater. Int.*, vol. 12, no. 4, pp. 323–329, 2006, doi: 10.1007/BF03027549.

[99] ASTM International, “Standard practice for calculation of corrosion rates and related information,” *Astm G 102*, vol. 89, no. Reapproved. pp. 1–7, 1999. doi: 10.1520/G0102-89R10.

[100] A. A. Olajire, “Corrosion inhibition of offshore oil and gas production facilities using organic compound inhibitors - A review,” *J. Mol. Liq.*, vol. 248, pp. 775–808, 2017, doi: 10.1016/j.molliq.2017.10.097.

[101] J. E. Hodge, E. C. Nelson, and B. F. Moy, “Metal chelation by glucose-ammonia derivatives,” *Chelates Agric.*, vol. 11, no. 2, pp. 126–129, 1963, [Online]. Available: papers3://publication/uuid/190B457C-E244-4FA1-A5E3-C4AE96311A56

[102] M. Su, L. Wei, J.-H. Zhu, T. Ueda, G. Guo, and F. Xing, “Combined impressed current cathodic protection and FRCM strengthening for corrosion-prone concrete structures,” *J. Compos. Constr.*, vol. 23, no. 4, pp. 1–11, 2019, doi: 10.1061/(asce)cc.1943-5614.0000949.

[103] H.-S. Lee, V. Saraswathy, S.-J. Kwon, and S. Karthick, “Corrosion Inhibitors for Reinforced Concrete: A Review,” *Corros. Inhib. Princ. Recent Appl.*, 2018, doi: 10.5772/intechopen.72572.

[104] K. V. Akpanyung and R. T. Loto, “Pitting corrosion evaluation: A review,” *J. Phys. Conf. Ser.*, vol. 1378, no. 2, 2019, doi: 10.1088/1742-6596/1378/2/022088.

[105] B. Brycki, I. Kowalczyk, A. Szulc, O. Kaczerewska, and M. Pakiet, “Organic Corrosion Inhibitors,” IntechOpen, 2018. doi: 10.5772/intechopen.72943.

[106] M. Honarvar Nazari, M. S. Shihab, E. A. Havens, and X. Shi, “Mechanism of corrosion protection in chloride solution by an apple-based green inhibitor: experimental and theoretical studies,” *J. Infrastruct. Preserv. Resil.*, vol. 1, no. 1, pp. 1–19, 2020, doi: 10.1186/s43065-020-00007-w.

[107] N. Sato, “Basics of corrosion chemistry,” in *Green Corrosion Chemistry and Engineering: Opportunities and Challenges*, 2011, pp. 1–32. doi: 10.1002/9783527641789.ch1.

[108] M. H. Nazari, M. S. Shihab, L. Cao, E. A. Havens, and X. Shi, “A peony-leaves-derived liquid corrosion inhibitor: Protecting carbon steel from NaCl,” *Green Chem. Lett. Rev.*, vol. 10, no. 4, pp. 359–379, 2017, doi: 10.1080/17518253.2017.1388446.

[109] H. Wei, B. Heidarshenas, L. Zhou, G. Hussain, Q. Li, and K. (Ken) Ostrikov, “Green inhibitors for steel corrosion in acidic environment: state of art,” *Mater. Today Sustain.*, vol. 10, p. 100044, 2020, doi: 10.1016/j.mtsust.2020.100044.

[110] E. McCafferty, “Validation of corrosion rates measured by the tafel extrapolation method,” *Corros. Sci.*, vol. 47, no. 12, pp. 3202–3215, 2005, doi: 10.1016/j.corsci.2005.05.046.

[111] H. Butt, K. Graf, and M. Kappl, “Physics and chemistry of interfaces,” in *Physics and Chemistry of Interfaces*, 2003. doi: 10.1002/3527602313.

[112] R. W. Revie and H. H. Uhlig, *Corrosion and Corrosion Control: An Introduction to Corrosion Science and Engineering: Fourth Edition*. 2008. doi: 10.1002/9780470277270.

[113] ŠTAMPAJ, “Pourbaix diagram (stability diagram),” 1963, [Online]. Available: http://www.uobabylon.edu.iq/eprints/publication_12_18276_228.pdf

[114] A. Atrens, G. L. Song, Z. Shi, A. Soltan, S. Johnston, and M. S. Dargusch, *Understanding the corrosion of mg and mg alloys*. Elsevier, 2018. doi: 10.1016/B978-0-12-409547-2.13426-2.

[115] S. A. Abd El-Maksoud, “Studies on the effect of pyranocoumarin derivatives on the corrosion of iron in 0.5 M HCl,” *Corros. Sci.*, vol. 44, no. 4, pp. 803–813, 2002, doi: 10.1016/S0010-938X(01)00090-7.

[116] S. Yuvaraj, K. Nirmalkumar, V. R. Kumar, R. Gayathri, K. Mukilan, and S. Shubikksha, “Materials Today : Proceedings Influence of corrosion inhibitors in reinforced concrete – A state of art of review,” *Mater. Today Proc.*, vol. 68, pp. 2406–2412, 2022, doi: 10.1016/j.matpr.2022.09.118.

[117] C. Monticelli, *Corrosion inhibitors*. Elsevier, 2018. doi: 10.1016/B978-0-12-409547-2.13443-2.

[118] C. Lai, B. Xie, L. Zou, X. Zheng, X. Ma, and S. Zhu, “Adsorption and corrosion inhibition of mild steel in hydrochloric acid solution by S-allyl-O,O’-dialkyldithiophosphates,” *Results Phys.*, vol. 7, pp. 3434–3443, 2017, doi: 10.1016/j.rinp.2017.09.012.

[119] Y. Lei, L. Zhiyong, Y. Weibin, and W. Zixiao, “Adsorption and Characterization of an Organic Corrosion Inhibitor for Inhibiting Carbon Steel Corrosion in Chloride Solution,” *Curr. Anal. Chem.*, vol. 12, no. 2, pp. 141–146, 2015, doi: 10.2174/1573411011666150804195604.

[120] ACI Committee 222, “Protection of Metals in Concrete Against Corrosion,” *Aci 222R-01*, pp. 1–41, 2001.

[121] J. Alcántara, D. de la Fuente, B. Chico, J. Simancas, I. Díaz, and M. Morcillo, “Marine atmospheric corrosion of carbon steel: A review,” *Materials (Basel).*, vol. 10, no. 4, 2017, doi: 10.3390/ma10040406.

[122] S. K. Shukla and M. A. Quraishi, “Cefotaxime sodium: A new and efficient corrosion inhibitor for mild steel in hydrochloric acid solution,” *Corros. Sci.*, vol. 51, no. 5, pp. 1007–1011, 2009, doi: 10.1016/j.corsci.2009.02.024.

[123] M. Christov and A. Popova, “Adsorption characteristics of corrosion inhibitors from corrosion rate measurements,” *Corros. Sci.*, vol. 46, no. 7, pp. 1613–1620, 2004, doi: 10.1016/j.corsci.2003.10.013.

[124] I. Langmuir, “The Constitution and Fundamental Properties of Solids and Liquids. Part I. Solids.,” vol. 2046, no. 1915, 1916.

[125] V. R. Saliyan and A. V. Adhikari, “Quinolin-5-ylmethylene-3-{[8-(trifluoromethyl)quinolin-4-yl]thio}propanohydrazide as an effective inhibitor of mild steel corrosion in HCl solution,” *Corros. Sci.*, vol. 50, no. 1, pp. 55–61, 2008, doi: 10.1016/j.corsci.2006.06.035.

[126] A. Yurt, G. Bereket, A. Kivrak, A. Balaban, and B. Erk, “Effect of Schiff bases containing pyridyl group as corrosion inhibitors for low carbon steel in 0.1 M HCl,” *J. Appl. Electrochem.*, vol. 35, no. 10, pp. 1025–1032, 2005, doi: 10.1007/s10800-005-7336-3.

[127] M. H. Sliem *et al.*, “AEO7 Surfactant as an Eco-Friendly Corrosion Inhibitor for Carbon Steel in HCl solution,” *Sci. Rep.*, vol. 9, no. 1, pp. 1–16, 2019, doi: 10.1038/s41598-018-37254-7.

[128] H. Lgaz, R. Salghi, K. Subrahmanya Bhat, A. Chaouiki, Shubhalaxmi, and S. Jodeh, “Correlated experimental and theoretical study on inhibition behavior of novel quinoline derivatives for the corrosion of mild steel in hydrochloric acid solution,” *J. Mol. Liq.*, vol. 244, pp. 154–168, 2017, doi: 10.1016/j.molliq.2017.08.121.

[129] O. Kaczerewska, R. Leiva-Garcia, R. Akid, B. Brycki, I. Kowalczyk, and T. Pospieszny, “Effectiveness of O-bridged cationic gemini surfactants as corrosion inhibitors for stainless steel in 3 M HCl: Experimental and theoretical studies,” *J. Mol. Liq.*, vol. 249, pp. 1113–1124, 2018, doi: 10.1016/j.molliq.2017.11.142.

[130] A. Raman, S. Nasrazadani, and L. Sharma, “Morphology of rust phases formed on weathering steels in various laboratory corrosion tests,” *Metallography*, vol. 22, no. 1, pp. 79–96, 1989, doi: 10.1016/0026-0800(89)90024-4.

[131] T. Mao, C. Li, F. Mao, Z. Xue, G. Xu, and A. Amirfazli, “A durable anti-corrosion superhydrophobic coating based on carbon nanotubes and SiO2 aerogel for superior protection for Q235 steel,” *Diam. Relat. Mater.*, vol. 129, no. 1801, p. 109370, 2022, doi: 10.1016/j.diamond.2022.109370.

[132] R. A. Antunes, R. U. Ichikawa, L. G. Martinez, and I. Costa, “Characterization of corrosion products on carbon steel exposed to natural weathering and to accelerated corrosion tests,” *Int. J. Corros.*, vol. 2014, 2014, doi: 10.1155/2014/419570.

[133] C. Leygraf, I. O. Wallinder, J. Tidblad, and T. Graedel, “Appendix F: the Atmospheric Corrosion Chemistry of Iron and Low Alloy Steels,” *Atmos. Corros.*, pp. 302–315, 2016, doi: 10.1002/9781118762134.app6.

[134] K. Xiao *et al.*, “Effect of Concentrations of Fe2+ and Fe3+ on the Corrosion Behavior of Carbon Steel in Cl− and SO42− Aqueous Environments,” *Met. Mater. Int.*, vol. 27, no. 8, pp. 2623–2633, 2021, doi: 10.1007/s12540-019-00590-y.

[135] M. A. G. Tommaselli, N. A. Mariano, and S. E. Kuri, “Effectiveness of corrosion inhibitors in saturated calcium hydroxide solutions acidified by acid rain components,” *Constr. Build. Mater.*, vol. 23, no. 1, pp. 328–333, 2009, doi: 10.1016/j.conbuildmat.2007.12.002.

[136] L. De Meyst *et al.*, “Parameter study of superabsorbent polymers (SAPs) for use in durable concrete structures,” *Materials (Basel).*, vol. 12, no. 9, pp. 1–15, 2019, doi: 10.3390/ma12091541.

[137] M. Hesami and R. Kiran, “Starch-based hydrogel powder for enhanced dust suppression,” *Clean. Eng. Technol.*, vol. 28, no. June, p. 101055, 2025, doi: 10.1016/j.clet.2025.101055.

[138] F. Chen, S. Bai, X. Guan, J. Qiao, and H. Gou, “Influence of type and particle size of superabsorbent polymer on early water distribution and internal curing zone properties of cement paste,” *Cem. Concr. Compos.*, vol. 150, no. April, p. 105526, 2024, doi: 10.1016/j.cemconcomp.2024.105526.

[139] K. Wang, K. Dong, J. Guo, and H. Du, “Absorption and Release mechanism of superabsorbent polymers and its impact on shrinkage and durability of internally cured concrete – A review,” *Case Stud. Constr. Mater.*, vol. 21, no. October, p. e03909, 2024, doi: 10.1016/j.cscm.2024.e03909.

[140] S. Choi and G. Hong, “SELF-SEALING OF CRACKS IN CEMENTITIOUS MATERIALS INCORPORATING SUPERABSORBENT POLYMERS UNDER WET / DRY CYCLIC CONDITIONS SELF-SEALING OF CRACKS IN CEMENTITIOUS MATERIALS INCORPORATING SUPERABSORBENT POLYMERS UNDER WET / DRY CYCLIC CONDITIONS,” no. March, 2019.

[141] A. Mignon, D. Snoeck, P. Dubruel, S. Van Vlierberghe, and N. De Belie, “Crack mitigation in concrete: Superabsorbent polymers as key to success?,” *Materials (Basel).*, vol. 10, no. 3, 2017, doi: 10.3390/ma10030237.

[142] C. Schröfl, K. A. Erk, W. Siriwatwechakul, M. Wyrzykowski, and D. Snoeck, “Recent progress in superabsorbent polymers for concrete,” *Cem. Concr. Res.*, vol. 151, no. October 2021, 2022, doi: 10.1016/j.cemconres.2021.106648.

[143] Z. Lyu *et al.*, “Absorption characteristics and shrinkage mitigation of superabsorbent polymers in pavement concrete,” *Int. J. Pavement Eng.*, vol. 23, no. 2, pp. 270–284, 2022, doi: 10.1080/10298436.2020.1742334.

[144] A. Jalal and R. Kiran, “Quantifying the water donation potential of commercial and corn starch hydrogels in a cementitious matrix,” *J. Mater. Res. Technol.*, vol. 24, pp. 4336–4352, 2023, doi: 10.1016/j.jmrt.2023.04.031.

[145] G. Merke, M. Hesami, and R. Kiran, “Super Absorbent Polymers (SAPs) as concentration preservers in brine deicers for enhanced ice melting capacity,” *J. Infrastruct. Preserv. Resil.*, vol. 6, no. 1, pp. 1–15, 2025, doi: 10.1186/s43065-024-00105-z.

[146] K. K. Yun, K. K. Kim, W. Choi, and J. H. Yeon, “Hygral behavior of superabsorbent polymers with various particle sizes and cross-linking densities,” *Polymers (Basel).*, vol. 9, no. 11, pp. 7–11, 2017, doi: 10.3390/polym9110600.

[147] C. R. Davis, S. L. Kelly, and K. A. Erk, “Comparing laser diffraction and optical microscopy for characterizing superabsorbent polymer particle morphology, size, and swelling capacity,” *J. Appl. Polym. Sci.*, vol. 135, no. 14, pp. 1–10, 2018, doi: 10.1002/app.46055.

[148] S. Zhao, O. M. Jensen, and M. T. Hasholt, “Measuring absorption of superabsorbent polymers in cementitious environments,” *Mater. Struct. Constr.*, vol. 53, no. 1, pp. 1–16, 2020, doi: 10.1617/s11527-020-1442-x.

[149] B. J. Olawuyi and W. P. Boshoff, “Influence of SAP content and curing age on air void distribution of high performance concrete using 3D volume analysis,” *Constr. Build. Mater.*, vol. 135, pp. 580–589, 2017, doi: 10.1016/j.conbuildmat.2016.12.128.

[150] D. Snoeck, P. Van den Heede, and N. De Belie, “Towards an adequate deicing salt scaling resistance of high-volume fly ash (HVFA) concrete and concrete with superabsorbent polymers (SAPs),”

Frost Action Concr., vol. RILEM PRO 114, no. August, pp. 141–150, 2016, [Online]. Available: http://hdl.handle.net/1854/LU-8531162

[151] D. Wang, X. Chen, C. Yin, M. Oeser, and B. Steinauer, "Influence of different polishing conditions on the skid resistance development of asphalt surface," *Wear*, vol. 308, no. 1–2, pp. 71–78, 2013, doi: 10.1016/j.wear.2013.09.013.

[152] V. Mechtcherine and H. W. Reinhardt, "Application of superabsorbent polymers (SAP) in concrete construction: State of the art report prepared by technical committee 225-SAP," *Appl. Super Absorbent Polym. Concr. Constr. State-of-the-Art Rep. Prep. by Tech. Comm. 225-SAP*, pp. 1–164, 2012, doi: 10.1007/978-94-007-2733-5.

[153] D. M. Ramakrishna and T. Viraraghavan, "Environmental impact of chemical deicers - A review," *Water. Air. Soil Pollut.*, vol. 166, no. 1–4, pp. 49–63, 2005, doi: 10.1007/s11270-005-8265-9.

[154] N. Adsul, J. W. Lee, and S. T. Kang, "Investigating the Impact of Superabsorbent Polymer Sizes on Absorption and Cement Paste Rheology," *Materials (Basel).*, vol. 17, no. 13, 2024, doi: 10.3390/ma17133115.

[155] H. X. D. Lee, H. S. Wong, and N. R. Buenfeld, "Effect of alkalinity and calcium concentration of pore solution on the swelling and ionic exchange of superabsorbent polymers in cement paste," *Cem. Concr. Compos.*, vol. 88, pp. 150–164, 2018, doi: 10.1016/j.cemconcomp.2018.02.005.

[156] B. Unal and R. C. Hedden, "pH-dependent swelling of hydrogels containing highly branched polyamine macromonomers," *Polymer (Guildf).*, vol. 50, no. 3, pp. 905–912, 2009, doi: 10.1016/j.polymer.2008.11.049.

[157] B. H. Woo, I. K. Jeon, D. H. Yoo, H. G. Kim, and J. S. Ryou, "Ice-melting performance assessment of cement composites using silicon carbide as fine aggregate," *Appl. Therm. Eng.*, vol. 194, no. May, p. 117113, 2021, doi: 10.1016/j.applthermaleng.2021.117113.

[158] R. Mahon, Y. Balogun, G. Oluyemi, and J. Njuguna, "Swelling performance of sodium polyacrylate and poly(acrylamide-co-acrylic acid) potassium salt," *SN Appl. Sci.*, vol. 2, no. 1, 2020, doi: 10.1007/s42452-019-1874-5.